Macro-Turbulent Energy Cascades In Upper Tropospheric-Lower Stratospheric Mesoscales

Dissertation

zur

Erlangung des akademischen Grades

doctor rerum naturalium (Dr. rer. nat.)

der Mathematisch-Naturwissenschaftlichen Fakultät

der Universität Rostock

vorgelegt von:

Serhat Can

geboren am 01.03.1990

in Istanbul

eingerichtet: 29.09.2022

verteidigt: 03.03.2023

Gutachter:

Prof. Erich Becker

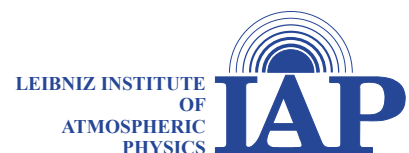(Leibniz-Institut für Atmosphärenphysik)

Prof. Thomas Birner

(Ludwig-Maximilians-Universität München)

Abstract

The focus of this thesis is on the investigation of the mesoscale (horizontal wavelengths that are smaller than about a thousand km) energy cascades in upper tropospheric and lower stratospheric (UTLS) altitudes. For this purpose, we performed simulations for 16 days of January conditions using a mechanistic general circulation model (GCM) with a high horizontal and vertical resolution extending up to the lower mesosphere ($\sim$ 55km height). Main results are twofold. Firstly, we fulfilled for the first time in a GCM the scale invariance criterion (SIC, a further physical constraint in addition to elementary hydrodynamical conservation laws) for both the horizontal subgrid-scale (SGS) diffusion of sensible heat and horizontal momentum. Secondly, the analyses of spectral kinetic energy (KE) and available potential energy (APE) budgets show that simulated KE and APE spectra in UTLS mesoscales can be explained by stratified macro-turbulence (SMT) theory. We also extended the SMT theory to include gravity wave (GW) energetics, which lead us to the conclusion that on average SMT is realized by the superposition of saturated mid-frequency GWs, such that half the energy deposited by these GWs as KE is converted to APE. Our results also show that the energy deposition of these resolved GWs is not captured properly unless SIC is fulfilled for both SGS horizontal diffusion of horizontal momentum and sensible heat.

Zusammenfassung

Der Schwerpunkt dieser Arbeit liegt auf der Untersuchung der mesoskaligen (horizontale Wellenlängen, die kleiner als etwa tausend km sind) Energiekaskaden in Höhen der oberen Troposphäre und der unteren Stratosphäre (UTLS). Zu diesem Zweck haben wir Simulationen für 16 Tage Januarbedingungen unter Verwendung eines mechanistischen globalen Zirkulationsmodells mit hoher horizontaler und vertikaler Auflösung, das sich bis in die untere Mesosphäre ($\sim$ 55km Höhe) erstreckt. Erstens haben wir zum ersten Mal in einem GCM das Skaleninvarianzkriterium (SIC, eine weitere physikalische Nebenbedingung zusätzlich zu elementaren hydrodynamischen Erhaltungsgesetzen) sowohl für die horizontale Untergitterskala (SGS) Diffusion der fühlbaren Wärme als auch für den horizontalen Impuls erfüllt. Zweitens zeigen die Analysen der Budgets für spektrale kinetische Energie (KE) und verfügbare potentielle Energie (APE), dass simulierte KE- und APE-Spektren in UTLS-Mesoskalen durch die Theorie der stratifizierten Makroturbulenz (SMT) erklärt werden können. Wir haben auch die SMT-Theorie um die Schwerewellen (GW)-Energetik erweitert, was uns zu dem Schluss führte, dass SMT im Durchschnitt der Überlagerung von gesättigten Mittelfrequenz-GWs entspricht, wobei die Hälfte der von diesen GWs als KE deponierten Energie in APE umgewandelt wird. Unsere Ergebnisse zeigen auch, dass die Energieabgabe dieser aufgelösten GWs nicht richtig erfasst wird, außer SIC ist sowohl für die horizontale SGS-Diffusion des horizontalen Impulses als auch für die fühlbare Wärme erfüllt.

Contents

Nomenclature

Acronyms

APE	Available potential energy
DSM	Dynamic smagorinsky model
FGGE	First GARP global experiment
GCM	General circulation model
gDSM	Label of the KMCM runs utilizing the generalized Dynamic smagorinsky model scheme for the horizontal diffusion
GW	Gravity wave
IE	Internal energy
IGW	Inertial gravity wave
KE	Kinetic energy
KMCM	Kühlungsborn mechanistic general circulation model
KT	Kolmogorov turbulence
LES	Large eddy simulation
PE	Potential energy
PEqs	Primitive equations
SGS	Subgrid scale
SIC	Scale-invariance criterion
SMAG	Label of the KMCM runs utilizing the classical smagorinsky scheme for the horizontal diffusion
SMT	Stratifi ed macro-turbulence
ST	Stratified turbulence
TKE	Turbulent kinetic energy
TPE	Total potential energy
UPE	Unavailable potential energy
UTLS	Upper troposphere-lowermost stratosphere

Greek Symbols

α	Aspect ratio
χ	Velocity potential
ϵ	Total frictional heating rate per unit mass
ϵ_h	Horizontal frictional heating rate per unit mass
ϵ_z	Vertical frictional heating rate per unit mass
η	Terrain following vertical hybrid coordinate
κ	Material conductivity
λ	Longitude
$\boldsymbol{\Sigma}$	2 dimensional Reynolds stress tensor
$\boldsymbol{\Sigma}_h$	Horizontal part of $\boldsymbol{\Sigma}$
$\boldsymbol{\Sigma}_z$	Vertical part of $\boldsymbol{\Sigma}$
μ_h	Horizontal diffusion of sensible heat
μ_z	Vertical diffusion of sensible heat
ν	Kinematic viscosity
ω	Pressure velocity
Φ	Geopotential
ϕ	Latitude
ψ	Stream function
ρ	Density
σ_{Th}	Thermal dissipation rate per unit mass due to horizontal turbulent diffusion of sensible heat
θ	Potential temperature
$\vec{\mathcal{T}}$	Subgrid scale horizontal sensible heat flux at the 2nd test filter scale
$\vec{\tau}$	Subgrid scale horizontal sensible heat flux at the 1st test filter scale
ξ	Relative vorticity

Latin Letters

$\hat{APE}$	Globally averaged APE per unit area at the Earth's surface
$\hat{APE}_E$	Eddy APE per unit area at the Earth's surface

$A\hat{P}E_Z$	Zonal mean APE per unit area at the Earth's surface
$\hat{KE}_E$	Eddy KE per unit area at the Earth's surface
$\hat{KE}_Z$	Zonal mean KE per unit area at the Earth's surface
$\mathbf{L}$	Leonard stress tensor
$\mathbf{M}$	Subgrid model kernel tensor
$\mathbf{P}$	Viscous stress tensor
$\mathbf{S}_{h0}$	Horizontal trace-free shear stress tensor
$\mathbf{S}_{z0}$	Vertical trace-free shear stress tensor
$\mathcal{G}$	Control volume of the atmosphere
$\mathcal{H}$	Enthalpy of the atmosphere in globally averaged climatological mean
$\mathcal{KE}$	Kinetic energy of the atmosphere in globally averaged climatological mean
$\mathcal{PE}$	Potential energy of the atmosphere in globally averaged climatological mean
$\vec{e}_x$	Zonal unit vector
$\vec{e}_y$	Meridional unit vector
$\vec{e}_z$	Vertical unit vector
$\vec{L}$	Vector analogue of the Leonard stress tensor
$\vec{M}$	Subgrid model kernel vector
$\vec{R}_h$	Diffusion of horizontal momentum
$\vec{v}$	3 dimensional velocity vector
$\vec{v}_h$	Horizontal velocity vector
$\vec{W}$	Sensible heat flux due to molecular conduction
$\vec{W}_t$	Eddy sensible heat flux due to turbulent temperature fluctuations
$\vec{W}_{ht}$	Horizontal part of $\vec{W}_t$
$\vec{W}_{zt}$	Vertical part of $\vec{W}_t$
$\vec{y}$	State vector of the KMCM
a_e	Earth's radius
APE^{DH}	Spectral contribution to APE_t from total diabatic heating
APE^{GW}	APE of GWs

APE^{HA}	Spectral contribution to APE_t from horizontal advection of APE
APE^{NBP}	Spectral contribution to APE_t from negative buoyancy production
APE^{VA}	Spectral contribution to APE_t from vertical advection of APE
APE^{VE}	Spectral contribution to APE_t from vertical exchange of APE
APE_t	Spectral tendency of APE per unit mass at a given mode layer l and total horizontal wavenumber n
APE_{ln}	Spectral APE per unit mass at a given mode layer l and total horizontal wavenumber n
C_A	Term for conversion of zonal-mean APE into eddy APE
C_E	Term for conversion of eddy APE into zonal eddy KE
C_K	Term for conversion of eddy KE into zonal mean KE
c_p	Specific heat capacity
c_s	Dynamic Smagorinsky parameter
C_Z	Term for conversion of zonal-mean APE into zonal mean KE
D_E	Term for dissipation of eddy KE
D_Z	Term for dissipation of zonal mean KE
e	Internal energy per unit mass
e_{APE}	Horizontal spectral APE density
E_{KE}	Horizontal integral scale KE density
e_{KE}	Horizontal spectral KE density
f	Coriolis frequency
Fr_h	Horizontal Froude number
G_E	Term for generation of eddy APE
G_Z	Term for generation of zonal mean APE
h	Enthalpy per unit mass
K_h	Horizontal diffusion coefficient of horizontal momentum
K_z	Vertical diffusion coefficient of horizontal momentum
KE^{AC}	Spectral contribution to APE_t from adiabatic conversion
KE^{GW}	KE of GWs
KE^{HA}	Spectral contribution to APE_t from horizontal advection of KE

KE^{MD}	Spectral contribution to APE_t from total horizontal momentum diffusion
KE^{VA}	Spectral contribution to APE_t from vertical advection of KE
KE_t	Spectral tendency of KE per unit mass at a given mode layer l and total horizontal wavenumber n
KE_{ln}	Spectral KE per unit mass at a given mode layer l and total horizontal wavenumber n
KE_{SGS}	Subgrid scale KE
KT_h	Horizontal diffusion coefficient of sensible heat
L_b	Buoyancy length scale of ST
l_h	Characteristic horizontal length scale of ST in section 5.1
l_h	Horizontal mixing length in sections 3.1 and 5.1
l_v	Characteristic vertical length scale of ST
l_v	Vertical mixing length in section 3.1
N	Brunt–Väisälä frequency
p	Pressure
p_s	Surface pressure
p_{00}	Constant reference pressure
Pr_h	Horizontal turbulent prandtl number
Q	Total diabatic heating
q	Specific humidity
Q_c	Prescribed cumulus heating in tropics
Q_m	Self-induced condensational heating in midlatitudes
Q_{rad}	Temperature relaxation as a surrogate for radiative heating
Q_{sens}	Rate of heating per unit volume of air via heat conduction
R	Molecular gas constant
R_i	Richardson number
Re_b	Buoyancy Reynolds number
Re_h	Horizontal Reynolds number
Ro_U	Integral velocity based Rossby number
Ro_ξ	Integral relative vorticity based Rossby number

s	Entropy per unit mass
T	Temperature
U_h	Characteristic integral horizontal velocity of ST in section 5.1
z_s	Surface height

Mathematical symbols used for scale separation

$(\;\check{}\;)$	Deviations from the hydrostatic reference state under anelastic approximation
$(\;\hat{}\;)$	Globally averaged mean per unit area at the Earth's surface
$(\;\overline{\overline{\;\;}}\;)$	Density weighted spatial average over resolution scale
$(\;\overline{\;\;}\;)$	Horizontal mean in chapters 2 and 4
$(\;\overline{\;\;}\;)$	Spatial and temporal average over GW scale in section 5.2
$(\;\overline{\;\;}\;)$	Spatial average over the resolution scale in sections 3.1 and 3.2
$(\;)''$	Deviations from the density weighted spatial average over resolution scale
$(\;)^*$	Perturbations from GW scale averaging
$(\;)'$	Deviations from the spatial average over the resolution scale
$(\;)_r$	A hydrostatic reference state under anelastic approximation
$(\;\widehat{\;\;}\;)$	Spatial average over the 1$^{\text{st}}$ test filter scale in sections 3.1 and 3.2
$(\;\widetilde{\;\;}\;)$	Deviations from the horizontal mean in chapters 2 and 4
$(\;\widetilde{\;\;}\;)$	Spatial average over the 2$^{\text{st}}$ test filter scale in sections 3.1 and 3.2
$<\;\;>$	Mass weighted vertically integrated global average
$[\;]$	Zonal mean
$\langle\;\rangle$	Temporal mean
$\|\;\|$	Frobenius norm

Chapter 1

Introduction

In the terminology which you graciously describe to me we might say that the atmosphere is a musical instrument on which one can play many tunes. High notes are sound waves, low notes are long inertial waves, and nature is a musician more of the Beethoven than of the Chopin type. He much prefers the low notes and only occasionally play arpeggios in the treble and then only with a light hand. The oceans and the continents are the elephants in Saint-Saens' animal suite, marching in a slow cumbrous rhythm, one step every day or so. Of course, there are overtones; sound waves, billow clouds (gravity waves), inertial oscillations, etc., but these are unimportant and are heard only at N.Y.U and M.I.T.

Jule Charney

This paragraph written by Charney in a letter from 1947 to a colleague of his at the time (Platzman (1987)), describes in a very elegant manner the overwhelming range of the temporal and spatial scales of atmospheric motion. Since this letter, our understanding of the large scales of atmospheric flow, or more specifically, synoptic scales (horizontal wavelengths on the order of several thousands of kms) and planetary scales (horizontal wavelengths larger than 10000km) has been significantly deepened, and our capacity to predict the future states of motion for these scales using numerical models has accordingly improved. However, as Charney pointed out in the above paragraph, smaller-scale motions have been subject to a certain level of disregard. This was in part due to the incapacity of computational power to appropriately perform numerical simulations including these scales and also due to the challenge of determining these small scales from observational data.

In their seminal work Nastrom and Gage (1985) analyzed aircraft measurements

of winds and temperature in the upper troposphere and derived the power spectra of these variable with respect to the horizontal wavenumber, that is, they determined the horizontal kinetic energy (KE) spectrum and the available potential energy (APE) spectrum. The existence of an exponential -3 spectral slope for KE and APE at synoptic scales (i.e. for $10 < n < 50$, where n is the total horizontal wavenumber) was found in their analysis, which further confirmed the applicability of the theory of geostrophic turbulence (Salmon (1998)) for the synoptic and planetary scales. Briefly explaining, akin to the classical 2D turbulence theory of Kraichnan (1967), in geostrophic turbulence theory the energy injection at scales of about 5 thousand km due to baroclinic instability initiates a forward cascade of enstrophy, which results in the characteristic n^{-3} power law for the KE and APE spectra at synoptic scales. Furthermore, the planetary scales, where energy is injected and which are larger than the baroclinic scale, are fed via an inverse energy cascade, which results in a shallower $-5/3$ like exponential spectral slope for KE and APE for $n < 10$.

Nastrom and Gage (1985) furthermore found a smooth and continuous KE and APE spectra with a clear $-5/3$ exponential spectral slope for the mesoscales, i.e. horizontal scales ranging from several hundreds of kilometers down to several tens of meters. This result raised significant interest with regard to the dynamics at these scales. The interpretation of the mesoscale energy spectra in the upper troposphere has gained growing attention since then. The so-called mesoscale kink that resides around several hundreds of kms of horizontal wavelengths marks the transition from the -3 exponential spectral slope to the more shallow $-5/3$ exponential spectral slope. A $n^{-5/3}$ power law was immediately interpreted as resulting from a nonlinear turbulence like dynamics that is associated with a macro-turbulent inertial range. Although the theories to explain the mesoscale dynamics since these measurements have been quite varying regarding the type of turbulence governing the inertial range, a consensus has been reached in recent years: mesoscale dynamics are primarily governed by a net forward energy cascade of both KE and APE. Both observational evidence (e.g., Lindborg (1999), Cho and Lindborg (2001), Deusebio et al. (2014)) and also numerical simulations (e.g., Koshyk and Hamilton (2001), Burgess et al. (2012), Brune and Becker (2013), Augier and Lindborg (2013)) point to the argument that mesoscale kink is a result of the relative dominance of this forward spectral flux of KE and APE over the forward enstrophy flux.

Investigations of mesoscale dynamics are often performed using high-resolution numerical models. With the increase in computational power, it has become a straight-

forward task to explicitly resolve a good part of the mesoscales in general circulation models (GCMs). In order to achieve a high effective resolution it is of paramount importance that these models obey the fundamental laws of physics. This applies specifically to the parameterization of the unresolved scales, which is needed due to the truncation of the model resolution at some wavelength within a macro-turbulent inertial range (see discussion in Schaefer-Rolffs and Becker (2018)). It has been long known that the small scale processes are inevitably linked to the large scale atmospheric flow because of the aforementioned forward energy cascades that are fed by baroclinicity. It is clear that the parameterization of unresolved scales should be compatible with the elementary hydrodynamical conservation laws (Becker (2001)). Otherwise even the simulated global budgets of angular momentum and energy may show systematic errors (Becker (2003a), Becker (2003b)). In recent years it has also become clear that another physical constraint needs to be fulfilled by models that are truncated in the inertial range of the mesoscales. This physical constraint is known as the scale-invariance (hereafter: SIC, Schaefer-Rolffs et al. (2015)), Schaefer-Rolffs (2019)).

Like the conservation laws, scale-invariance is automatically fulfilled for the scales resolved in a GCM. This does, however, not hold for the parameterized subgrid scales. For models that are truncated within the macro-turbulent inertial range of the mesoscales, fulfillment of the SIC by the subgrid-scale (SGS) parameterization is crucial for the proper simulation of the forward spectral cascades of KE and APE down to the resolution scale (Schaefer-Rolffs and Becker (2018)). The constraint of the SIC applies to the forward cascades of KE and APE, as well as to any tracer in the model that is subject to a forward cascade of tracer variance (Schaefer-Rolffs et al. (2015)). This constraint has been successfully applied to the diffusion of horizontal momentum using a high horizontal resolution version of the Kühlungsborn Mechanistic general Circulation Model (KMCM, Schaefer-Rolffs and Becker (2018)). The purpose of the first part of our study is to extend the SIC constraint also to the SGS parameterization of the horizontal macro-turbulent diffusion of sensible heat.

Once the macro-turbulent energy cascades are properly simulated by the model, a thorough assessment of theories regarding mesoscale dynamics is possible based on model data. One such theory that provides an explanation for the observed $-5/3$ exponential spectral slope in the mesoscales of the power spectra of horizontal momentum and temperature is known as the stratified turbulence (ST, Lindborg (2006)). Idealized ST theory can explain several features of the atmospheric mesoscale energy

cascades. Surprisingly, the characteristic conversion from KE to APE that is predicted for this macro-turbulent intertial range is also found in the process of gravity wave (GW) breaking due to dynamic instability and the subsequent dissipation of GW energy. On the other hand, the relative dominance of vortical KE modes in observed and simulated energy cascades associated with ST contrasts with the relative dominance of divergent modes found in atmospheric mesoscales (Lindborg (2015), Blažica et al. (2013), Schumann (2019), Waite (2020)). Other theories that have been put forth in order to explain the observed mesoscale $n^{-5/3}$ power law were based on surface quasi-geostrophic dynamics (Tulloch and Smith (2009)) or superposition of linear GWs (Callies et al. (2014)). The applicability of the surface quasi-geostrophic turbulence theory is controversial (Lindborg (2009)). The theory of superposition of linear GWs was shown to underestimate the degree of nonlinearity found in the mesoscales (Li and Lindborg (2018)) and it does not put any argument on any energy conversions and cascades. Therefore, in the second and main part of our study, we focus on the question of to what extent the theory of Stratified Macro-Turbulence (SMT), which is an extension of the idealized ST theory to the atmosphere, applies to the mesoscales as simulated by KMCM extended by a SGS horizontal diffusion scheme that fulfills the SIC.

The outline of this thesis is as follows: In chapter 2 we provide the theoretical basics of the research. Aside from the details of the mathematical formulation of our main method, i.e. the spectral KE and APE budget analysis, our focus is on the details of the Lorenz Energy Cycle and the concept of available potential energy in stratified fluids (Lorenz (1955), Lorenz (1967)). In chapter 3 we present the SIC and the details of its implementation in the SGS parameterization of the horizontal diffusion of sensible heat. We also discuss consequences for the model results when using the fully scale-invariant horizontal diffusion. In chapter 4 we compare the new model version of the KMCM that includes the fully scale-invariant horizontal diffusion with the analyses of Lambert (1984). In chapter 4, we also address the validity of our spectral APE budget analysis. In chapter 5 we provide a through theoretical discussion of the simulated mesoscale dynamics with respect to the theory of SMT. In particular, we evaluate the applicability of both SMT and GW saturation theory to the simulated mesoscales. Chapter 6 provides a summary of our work and an outlook.

Chapter 2

Theoretical Background

Mesoscale atmospheric flow refers to horizontal scales from several 10 m to about 1000 km and corresponding time scales from a few minutes to about one week Orlanski (1975). Compared to larger scales (such as quasi-geostrophic flow) and smaller scales (small-scale atmospheric turbulence), relatively little is known about the characteristic dynamics in the mesoscales. Therefore the study of dynamical processes in the mesoscales includes the interactions across scales that are associated with corresponding transfers of energy.

In order to quantify these transfers, we need to be able to formulate energy budgets for the atmosphere. For this purpose, we start with the conventional set of governing equations that are extensively used in General Circulation Models (GCMs), i.e. the general form of Primitive Equations (PEqs). For convenience, we use the PEqs for dry atmospheric flow and with pressure (denoted as p) as vertical coordinate:

$$\partial_t \vec{v}_h = \vec{v}_h \times (f + \xi)\vec{e}_z - \omega \partial_p \vec{v}_h - \vec{\nabla}_h \left(\Phi + \frac{\vec{v}_h^2}{2} \right) + \vec{R}, \tag{2.1}$$

$$\partial_p \Phi = -\frac{RT}{p}, \tag{2.2}$$

$$0 = \vec{\nabla}_h \cdot \vec{v}_h + \partial_p \omega, \tag{2.3}$$

$$d_t T = \frac{RT}{c_p p}\omega + \frac{1}{c_p}Q + \frac{1}{c_p}\epsilon. \tag{2.4}$$

Equation (2.1) is the horizontal momentum equations, where $\vec{v}_h$, f, ξ, ω, Φ and $\vec{e}_z$ represent the horizontal velocity vector, Coriolis frequency, relative vorticity, pressure velocity, geopotential and the unit vector in vertical direction, respectively[1]. The density ρ is given by RT/p according to the ideal gas law, where the scalar R is the molecular gas constant of air and T is the temperature. The vector $\vec{R} = \frac{RT}{p}\vec{\nabla}\Sigma$ represents the diffusion of momentum with the Reynolds stress tensor Σ and its details

---

[1] As usual, we apply the traditional approximation for the Coriolis force as well (Phillips (1966)).

will be explained in the next chapter.

Equation (2.2) is the hydrostatic approximation. It is used because the vertical accelerations of fluid parcels in mesoscale flow are usually very small against the gravity acceleration, as long as strong regional convective updrafts/downdrafts and high-frequency gravity waves are not considered explicitly. Thus the relation for the dominant forces in the vertical direction reduces to a balance between gravity and the vertical gradient of pressure.

Equation (2.3) is the continuity equation. It corresponds to the anelastic form of continuity equation when the height z is used as vertical coordinate (see Becker (2017), Appendix).

Equation (2.4) represents the prognostic thermodynamic equation in terms of enthalpy (i.e. $h = c_p T$) per unit mass, where the total time derivative is represented by symbol d_t and c_p is the specific heat capacity for constant pressure. Q represents a comprehensive diabetic heating term, which corresponds to the external or differential heating of the atmosphere plus the total turbulent sensible heat diffusion. The definition of this term and its components are provided in section 2.2. Finally the term $\epsilon = \frac{RT}{p}(\boldsymbol{\Sigma}\vec{\nabla}_h) \cdot \vec{v}_h$ is the frictional heating. By definition, it represents the irreversible heating due to the dissipation of kinetic energy. According to the 2nd law of thermodynamics, it has to be positive definite.

Following Lorenz (1967), we can write the global energy budget in z-coordinates to reduce mathematical complexity for our system defined with the above set of equations as follows,

$$\partial_t(\mathcal{KE} + \mathcal{PE} + \mathcal{H}) = -\oiint_{\partial\mathcal{G}} \left\langle \rho\left(c_p T + \Phi + \frac{\vec{v}_h}{2}\right)\vec{v}_h \right\rangle \cdot d\vec{f}$$
$$+ \int_{\mathcal{G}} \left\langle \rho Q \right\rangle dV + \oiint_{\partial\mathcal{G}} \left\langle \boldsymbol{\Sigma}\vec{v}_h \right\rangle \cdot d\vec{f}, \tag{2.5}$$

where,

$$\mathcal{KE} = \int_{\mathcal{G}} \left\langle \rho\frac{\vec{v}_h^2}{2} \right\rangle dV, \tag{2.6}$$

$$\mathcal{PE} = \int_{\mathcal{G}} \left\langle \rho\Phi \right\rangle dV, \tag{2.7}$$

$$\mathcal{H} = \int_{\mathcal{G}} \left\langle \rho c_p T \right\rangle dV. \tag{2.8}$$

In equation (2.5), the extend of the control volume $\mathcal{G}$ in spherical coordinates is given as follows:

$$\mathcal{G} = \left\{ \lambda = 0 \cdots 2\pi, z = z_s \cdots \infty, \phi = -\frac{\pi}{2} \cdots \phi_1 \leq \frac{\pi}{2} \right\}, \tag{2.9}$$

where λ is the longitude, ϕ is the latitude, $z_s = z_{s(\lambda,\phi)}$ is the surface height and ϕ_1 is some latitude farther north. By definition, the infinitesimally small vector area element $d\vec{f}$ is perpendicular to the closed surface of the control volume, i.e. $\partial \mathcal{G}$. Symbol $\langle \ \rangle^2$ denotes the temporal averaging.

For this control volume, we can neglect the frictional effects at its boundaries, meaning that the last term on the right-hand side can be dropped. Evidently, the northward energy flux term becomes zero when we integrate $\partial \mathcal{G}$ for all the latitudes until north pole, i.e. the whole atmosphere (Hartmann (1994)). Furthermore, considering that the total energy of the atmosphere does not change significantly over climatological time scales, left-hand side is zero in the climatological mean as well.

The conclusion from above arguments is that the differential heating of the total atmosphere is zero in climatological equilibrium Lorenz (1967), and the net diabatic heating is given by the frictional heating. This conclusion has significant implications regarding the energy transfers across the mesoscales. Since planetary and synoptic scales are well resolved in GCMs used for climate modeling, the energy transfer from synoptic scales to the mesoscales can be analyzed based on these models when evaluating the forward spectral fluxes at the resolution scale, which typically is at horizontal wavelengths of about 500 to 1000 km (Brune and Becker (2013), Augier and Lindborg (2013)). Note that in any GCM, the net forward energy flux at the resolution scale will result in dissipation by the sub-grid scales (SGS). With regard to high-resolution version of Kühlungsborn Mechanistic general Circulation Model (KMCM) with high resolution extending into mesoscales down to a horizontal wavelength of about 120 km, we can evaluate the energy transfers in the mesoscale over a significant range of scales. Note that the SGS and their unresolved interactions with the resolved flow must be modeled as turbulence parameterizations. Accordingly, the quantification of the SGS processes can only be assessed if the micro-scale energy dissipation processes are in some way modeled in accordance with the angular momentum and energy conserva-

---

[2] Since control volume $\mathcal{G}$ also corresponds to the system volume at the global scale, for long time averages it can be considered as being independent of temporal dimension. This allows us to change the order of the derivative and integrate for the volume to get the rate of change of the extensive properties of the system.

tion laws. Since in KMCM we account for diffusive processes in a physically consistent way, energy dissipation can be accounted in a consistent fashion. Therefore, in order to analyze these energy fluxes among KE (Kinetic Energy), PE (Potential Energy) and H (enthalpy) we first need to understand how the atmospheric motion is generated.

2.1   Availability of Energy For Stratified Fluids

In the previous section, we discussed the rate of change of the sum of the three energy reservoirs that can be used to describe the energetics of the atmosphere in the global mean[3]. We argued that the total energy of this system does not undergo significant changes, meaning their sum is constant in climatological equilibrium. Since the atmosphere is never in a steady state, we need to assess the transfers of energy between the three reservoirs to estimate the global energetics of the atmosphere. To further simplify our analysis we note that in a stratified system both PE and Internal Energy (IE[4]) can generate KE thus consider them together. Following Lorenz (1955), we therefore consider the sum PE and IE, i.e. the TPE in pressure coordinates;

$$
\begin{aligned}
TPE &= \int_{p_s}^{0} \langle \Phi + e \rangle \, dp = \int_{0}^{p_s} \left\langle \frac{p}{\rho g} + \frac{c_v T}{g} \right\rangle dp = \frac{1}{g} \int_{0}^{p_s} \langle (R + c_v) T \rangle \, dp \\
&= \frac{1}{g} \int_{0}^{p_s} \langle c_p T \rangle \, dp,
\end{aligned}
\tag{2.10}
$$

where, $p_s = p_{s(\lambda,\phi)}$ is the surface pressure. In order to estimate the possible energy transfers between TPE and KE, we construct a simple model that consists of two control volumes with fixed masses and uniform but different temperatures. They are standing side by side and are bounded by rigid walls on the sides and at the surface, just as physicist Max Margules depicted in his seminal papers in 1903 (Margules (1903)) and later in 1906 (Margules (1906)).

Following his 1903 paper, Figure 2.1 visualizes these two air parcels as a closed system. θ_i represents the potential temperatures[5] of each parcel and are given as

---

[3] It should be noted that we are not considering the latent energy as a prognostic quantity. Such a task requires an additional tendency equation for specific humidity, q. Our PEqs do not include tendency of q. Hence our study is based on dry air dynamics and latent heating is considered merely as a differential heating term.

[4] Internal Energy is defined as $IE = \int_{p_s}^{0} \langle e \rangle \, dp$, for e being the IE per unit mass.

[5] Potential temperature is defined as $\theta = T(p_{00}/p)^{R/c_p}$, where p_{00} is a constant reference pressure that

$\theta_2 > \theta_1$. Notice that top of each air mass has the same pressure but not the same height. Additionally, there is no external heat source. In the initial state, this closed system is at rest. Let us imagine that the mass is rearranged isentropically into a new state such that in the end state of this closed system every level becomes an isothermal surface, meaning stable stratification is achieved. Margules noted that during the rearrangement the system would attain a maximum value of KE.
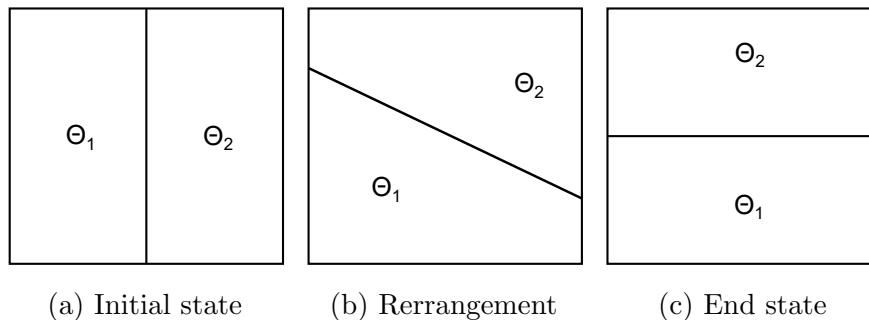

(a) Initial state   (b) Rerrangement   (c) End state

Figure 2.1: Margules' closed system of two air parcels with different uniform temperatures. In the beginning and at the end the amount of KE is 0. However, the transition from the initial state (named A) to the end state (named C) includes non zero KE due to rearrangement of the air masses within the system.

For given values of θ_1, θ_2, p_{surf} and p_{top}, we may calculate the TPE of the beginning and the end states using equation (2.10). According to Figure 2.1, a simple relation regarding the net generation of KE in connection to the beginning and the end states can be written as follows;

$$\delta KE = -\delta TPE = TPE_C - TPE_A. \tag{2.11}$$

Using equation (2.11) we can quantify the maximum velocity that could be obtained from such a closed system. Margules provided such values for different altitudes via accounting for the exponential decrease of pressure. For its time, the approximate speeds he calculated were impressively accurate (Haurwitz (1941), his section 91, Gill (1982), his section 7.8). Furthermore, this simple thought experiment demonstrates the fact that in stably stratified systems only a portion of the TPE is ready to be converted into KE. However, Margules' closed system cannot be used to quantify the energy cascades and accurate energy conversions. It was later recognized by mathematician and meteorologist Edward Lorenz that Margules considered only the KE that can be generated because his simple dynamical system did not cover the whole extent of the

---

satisfies $p_{00} > p$.

atmosphere.

In one of his most influential papers (Lorenz (1955)) Lorenz pointed out the fact that a single column or a certain height of a limited area (similar to the setting in Margules's closed system) cannot describe the total potential energy content in the atmosphere that is ready to be converted into KE. Lorenz simply generalized the idea of defining an "available" portion of the TPE to be converted to KE via the difference between two TPE states, by using the potential temperature as vertical coordinate for this stably stratified system. Let us similarly extend the TPE from equation (2.10) without the time averaging;

$$\frac{1}{g} \int_0^{p_s} c_p T \, dp = \frac{1}{g} \int_0^{p_s} c_p T \left(\frac{p_{00}}{p}\right)^\kappa \frac{p^\kappa}{p_{00}^\kappa} \, dp = \frac{c_p}{g p_{00}^\kappa} \int_0^{p_s} \frac{\theta}{(\kappa+1)} \, dp. \tag{2.12}$$

In the above equation, κ is the ratio $\frac{R}{c_p}$ and p_{00} is a reference ground level pressure that is uniform over the whole surface. We continue with integration by parts;

$$\begin{aligned}
\frac{c_p}{g p_{00}^\kappa (\kappa+1)} \int_0^{p_s} \theta \, dp &= \frac{c_p}{g p_{00}^\kappa (\kappa+1)} \left[-\theta p^{\kappa+1} \Big|_{\theta_s}^\infty + \int_{\theta_s}^\infty p^{\kappa+1} \, d\theta \right] \\
&= \frac{c_p}{g p_{00}^\kappa (\kappa+1)} \left[\theta_s p_{00}^{\kappa+1} + \int_{\theta_s}^\infty p^{\kappa+1} \, d\theta + \int_0^{\theta_s} p^{\kappa+1} \, d\theta - \underbrace{\int_0^{\theta_s} p^{\kappa+1} \, d\theta}_{p_{00}^{\kappa+1} \theta_s} \right] \\
&= \frac{c_p}{g p_{00}^\kappa (\kappa+1)} \int_0^\infty p^{\kappa+1} \, d\theta.
\end{aligned} \tag{2.13}$$

The last expression in equation (2.13) can include any distribution of pressure field in θ-coordinates. A minimum TPE that can be attained is a horizontally uniform pressure field that aligns with the isentropes, which is given by;

$$\frac{c_p}{g p_{00}^\kappa (\kappa+1)} \int_0^\infty \bar{p}^{\kappa+1} \, d\theta, \tag{2.14}$$

where $(\bar{\ })$ is the horizontal mean[6]. Equation (2.14) defines the minimum TPE for any given state of the atmosphere after a hypothetical global rearrangement of the air parcels has taken place. Using equation (2.13) we can also define the TPE before the rearrangement;

$$\frac{c_p}{g p_{00}^\kappa (\kappa+1)} \int_0^\infty \overline{p^{\kappa+1}} \, d\theta. \tag{2.15}$$

---

[6] The horizontal mean of a flow variable X is defined as: $\overline{X} = \frac{1}{4\pi} \int_0^{2\pi} \int_{-1}^1 X \, d\sin\phi \, d\lambda$.

Now that we can calculate a global measure between these two states by directly considering the total mass of the atmosphere and its isentropic displacements to reach a minimum state, Lorenz's famous Available Potential Energy (APE) can be defined:

$$A\hat{P}E = \frac{c_p}{gp_{00}^\kappa(\kappa+1)} \int_0^\infty \left(\overline{p^{\kappa+1}} - \bar{p}^{\kappa+1} \right) d\theta. \tag{2.16}$$

This is the exact formulation of APE[7]. It is readily seen that it is a positive definite quantity and describes the deviation from a certain stably stratified atmospheric state. In order to formulate the equation (2.16) in terms of the local temperature deviations again with the pressure as vertical coordinate, we can use the power series expansion and we assume that the atmosphere assumes small deviations for $(\bar{\theta}, \bar{p}, \overline{T})$. This leads to[8];

$$A\hat{P}E \approx \frac{g}{2} \int_0^{p_{00}} \frac{\overline{\widetilde{T}^2}}{\overline{T}^2 \overline{N}^2} \, dp. \tag{2.17}$$

In equation (2.17), ($\widetilde{}$) represents the deviations form the horizontal mean. With this form, it is also possible to define two different forms of APE that correspond to the zonal-mean[9] flow and the deviations from this flow (often called "eddies"):

$$A\hat{P}E_Z = \frac{g}{2} \int_0^{p_{00}} \frac{\overline{[T] - \overline{T}}}{\overline{T}^2 \overline{N}^2} \, dp, \tag{2.18}$$

$$A\hat{P}E_E = A\hat{P}E - A\hat{P}E_Z. \tag{2.19}$$

Accordingly, the total kinetic energy can also be split up into the KE from the zonal mean flow and eddies:

$$K\hat{E}_Z = \frac{1}{2g} \int_0^{p_{00}} \overline{[\vec{v_h}]^2} \, dp, \tag{2.20}$$

$$K\hat{E}_E = \frac{1}{2g} \int_0^{p_{00}} \left(\overline{\vec{v_h}^2} - \overline{[\vec{v_h}]^2} \right) dp. \tag{2.21}$$

The above forms of the zonal-mean and eddy energies are extensively used in climate studies. Consideration of three forms of energy (namely IE, PE and KE) is essentially reduced to two by realizing that only a tiny fraction of the TPE defined by equation (2.10) is available for conversion into KE. It is possible to write budget equations for

---

[7] Or more precisely defined, it is the "average APE per unit area of the Earth's surface". ($\hat{}$) symbol denotes the horizontal and mass-weighted vertical averaging, which results in a per unit area quantity.

[8] Please refer to Appendix A for the derivation of equation (2.17).

[9] The zonal mean of a flow variable X is defined as; $[X] = \frac{1}{2\pi} \int_0^{2\pi} X \, d\lambda$.

APE and KE. When these budget equations are studied together with certain observational facts about the energy source of the atmosphere and global wind measurements, they reveal important energy conversion paths. To briefly discuss these conversions, we refer to Lorenz's Monograph (Lorenz (1967)).

A simple budget equation for both APE and KE would at the least be composed of a common conversion term that describes how KE and APE exchange energies, a dissipation term for KE and finally a generation term for APE. Irreversible destruction of KE would increase the TPE of the system. This part is called the Unavailable PE, i.e. UPE = TPE − APE. UPE is in fact the TPE_{min} and dissipation of KE would regulate the thermodynamic state of the atmosphere thus essentially feeding the UPE reservoir. In our study, we do not consider the budget of UPE. By introducing the zonal-mean and eddy decomposition, the budget equations for APE and KE can be written as;

$$A\dot{\hat{P}}E_Z = -C_Z - C_A + G_Z, \tag{2.22}$$

$$A\dot{\hat{P}}E_E = -C_E + C_A + G_E, \tag{2.23}$$

$$K\dot{\hat{E}}_Z = C_Z - C_K - D_Z, \tag{2.24}$$

$$K\dot{\hat{E}}_E = C_E + C_K - D_E, \tag{2.25}$$

where the symbol ($\dot{}$) represents the partial time derivative. In above set of 4 equations, terms C, G and D respectively denote conversion, generation and dissipation of the corresponding energy reservoir. The subscripts Z and E denote the zonal and eddy components of the corresponding reservoir. Lorenz started his analysis by noting that the ultimate source of APE is the solar radiation and it would essentially be represented by G_Z. This term feeds the $A\hat{P}E_Z$ via the meridional temperature distribution in the troposphere.

C_A represents the cross-scale nonlinear energy transfer of APE along the spatial scales. Based on the measurements of horizontal and vertical eddy transport of heat it was discovered that the dominant transport of heat is not counter gradient (Starr and White (1954)) thus C_A mainly transfers $A\hat{P}E_Z$ into $A\hat{P}E_E$. On the other hand, based on wind measurements, the horizontal angular momentum transport was observed to be mainly counter-gradient along the gradient of angular velocity (Starr (1953)). Therefore C_K describes eddy to zonal-mean KE conversion, which corresponds to an

inverse energy cascade, that is from synoptic scales to planetary scales.

Consequently, Lorenz deduced that there is no other source for $\hat{KE}_E$ other than $\hat{APE}_Z$[10] and that the (on average) positive conversion term C_E represents baroclinic instability. This conversion occurs at synoptic scales with typical zonal wavenumbers around 6, corresponding to horizontal wavelengths of a few 1000 km at middle latitudes. Analysis of reanalyses and simulation results of free-running GCMs confirmed that there is a forward enstrophy cascade at smaller scales and an inverse energy cascade towards planetary scales (e.g., Boer and Shepherd (1983), Burgess et al. (2012), Brune and Becker (2013)), which is analogous to the 2D turbulence theory (Kraichnan (1967)). Therefore, the planetary and synoptic scale dynamics are often referred to as geostrophic turbulence (Salmon (1998)).

Since it was clear that C_E is the main process that converts APE into KE in the atmosphere, the remaining question with regard to the Lorenz Energy Cycle is how the generated KE is dissipated. Briefly, the D_Z is mainly concentrated in the lowest layers of the atmosphere in the form of frictional heating in the Prandtl layer (e.g., Becker (2003b)). Planetary scales dissipate their energy via D_Z by surface friction. D_E is mostly dominant in the free atmosphere above the boundary layer and comparable amounts of both vertical and horizontal frictional heating are contributing to it (Becker and Burkhardt (2007)).

With these considerations, Lorenz arrived at an elegantly simple picture of conversion between 3 dominant energy reservoirs. Figure 2.2 (reproduced after the textbook of "Physics of Climate" lecture at University of Rostock, Chapter 4.4, Becker (2019)) shows a simple schematic regarding the energetics we discussed above. Based on observational studies, assimilated model runs and GCM results, a low
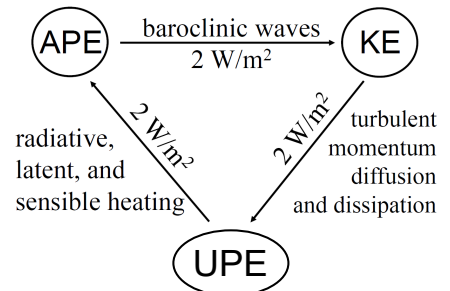

Figure 2.2: Schematic of the Lorenz Energy Cycle.

threshold of 2 W/m² is determined for the global conversion rates. As we mentioned in the previous subsection, the global average of the differential heating term "Q" is 0 for climatological time scales. Therefore, the net diabatic heating of the atmosphere is equal to the dissipation of KE. A thorough discussion of the energetics via the spectral

---

[10] The conversions from $\hat{APE}_Z$ to $\hat{KE}_E$ and from $\hat{KE}_Z$ to $\hat{APE}_E$ simply do not enter above expressions. Lorenz further argued that even increased resolutions in measurements did not support such conversions.

budget analyses of KE and APE for the planetary and synoptic scales from our 16 days of January simulations using KMCM is given in chapter 4, in which we refer to the above mentioned right-hand side terms of the equations from (2.22) to (2.25).

With the development in measurement techniques over the years, large-scale power spectra of winds and temperature became available. Nastrom et al. (1984) and Nastrom and Gage (1985) analyzed wind and temperature measurements in the Upper Troposphere-Lowermost Stratosphere (UTLS) region during nearly 7000 commercial flights. Figure 2.3 shows the obtained power spectra for the horizontal wind components and the potential temperature (also known as the Nastrom and Gage spectra).
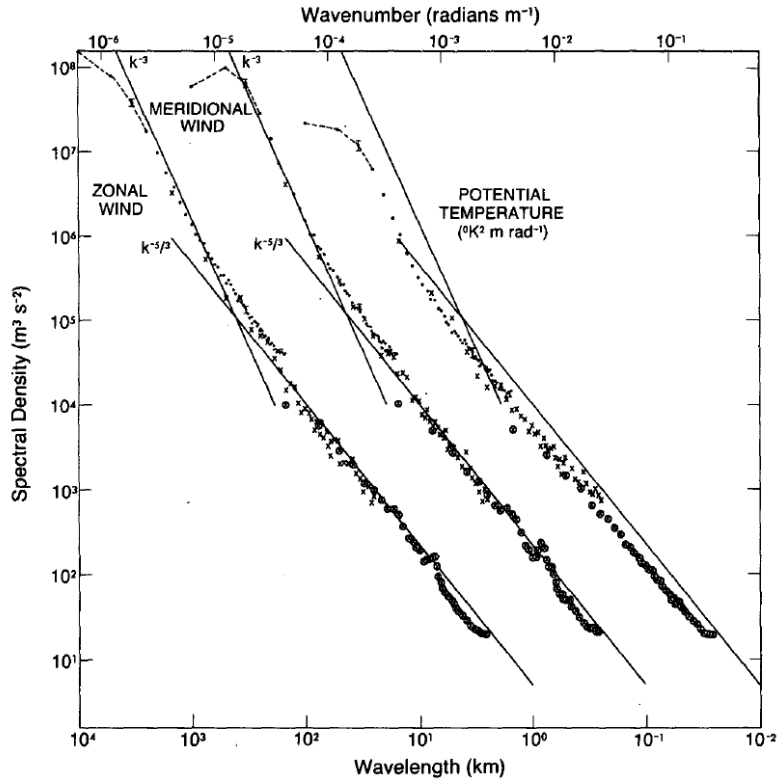
Figure 2.3: Power spectral density for zonal and meridional wind and potential temperature reproduced from Nastrom and Gage (1985), their Figure 3.

A clear -3 exponential slope for scales larger than 1000 km was found, which is in accordance with the geostrophic turbulence theory, where the dynamics are primarily determined by a forward cascade of enstrophy. Furthermore, there is a shallowing of the spectra for wavelengths larger than ~ 4000km. This behavior for scales larger than the scales where energy is injected due to baroclinic instability can be interpreted as the inverse energy cascade with a $-5/3$ exponential spectral slope, as is predicted by

14

the theory of geostrophic turbulence. This finding corresponds to the transfer from eddy KE to zonal-mean KE within the picture of the Lorenz Energy Cycle.

Towards larger wavenumbers, we can see again a shallowing of the spectra. More specifically, for wavelengths smaller than several hundred kilometers, there is a clear $-5/3$ exponential spectral slope for both wind components and the potential temperature. A smooth continuous spectra in mesoscales for winds and temperatures were identified, which was in disagreement with the earlier theories regarding the possibility of a spectral gap between the global and small scales. Existence of a continuous exponential spectral slope points out to the fact that there is an intermediate range of dynamics, which connects planetary and synoptic scales to smaller, more isotropic scales of motion.

Earlier interpretations regarding the mesoscale dynamics were based on the assumption of an inverse energy cascade hypothesis similar to planetary scale dynamics. More specifically, an inverse energy cascade that is fed by convection, storms, and other localized events was proposed, which would be governed by the scaling laws of two-dimensional turbulence (e.g., Lilly (1983)). However, both the correlation functions derived from wind measurements (Cho and Lindborg (2001)) and horizontal spectral KE budget analyses from numerical models (Koshyk and Hamilton (2001), Brune and Becker (2013), Augier and Lindborg (2013)) showed that KE in fact cascades towards smaller structures on average in the mesoscales. These findings of $-5/3$ horizontal energy spectra for winds and temperatures in combination with a forward KE cascade supported the notion that the theory of Stratified Turbulence (ST, Lindborg (2006), Billant and Chomaz (2001)) provides a consistent explanation for the macro-turbulent behavior of the mesoscales in the upper UTLS. ST describes the dynamics of freely decaying turbulent motions under strong stratification.

In idealized ST, KE and APE are equipartitioned in wavenumber space and are both transferred to scales smaller than the energy injection scale. Similar to classical isotropic Kolmogorov Turbulence (KT), a constant spectral energy flux is found within the inertial range. Since both APE and KE are subject to direct cascades, dissipation of both energy reservoirs plays an important role in mesoscales. As we mentioned in previous subsection, parameterization of KE dissipation in a GCM that resolves planetary and synoptic scales has to comply with fundamental conservation laws, since it is an indispensable part of the Lorenz Energy Cycle. Likewise, the APE cascades

and its dissipation in mesoscales are expected to play a non-negligible, if not equal, role as much as the KE cascades and dissipation. Subsequently, the parameterized turbulent dissipation of KE and APE in mesoscales in a GCM should also comply with an additional fundamental physical law, i.e. scale-invariance (Schaefer-Rolffs et al. (2015), Schaefer-Rolffs (2019)), which we discuss in chapters 3.2 and 5.2. It should be noted that the dissipation of APE is a neglected mechanism in the Lorenz Energy Cycle, hence does not enter the expressions of the system described by equations from (2.22) to (2.25).

However although ST provides a physically consistent framework to explain the direct cascades of APE and KE, the atmosphere is subject to a wide range of dynamical phenomena in the mesoscales that are not necessarily captured by the idealized picture of ST. On the other hand, the dynamics of ST may not be describable by GCMs run at sufficiently high resolutions because of numerical dissipation or deficiencies in the SGS parameterizations. In this study, we focus the on question of to what extent the macro-turbulent behavior in the mesoscales can be explained by ST. We follow Brune and Becker (2013) regarding the spectral analyses of the KE budget, and we extend the analysis by an account of the spectral APE budget. Brune and Becker (2013) used an idealized simulation performed with the KMCM at high spatial resolution and without explicitly accounting for the moisture cycle (dry model version). In this study, we use the same model setup, albeit with different parameterization of subgrid scales. It is important to note that our new simulations, like the former simulations of Brune and Becker (2013), do not include a mesoscale energy injection mechanism for APE. In the following section, we provide the APE budget formulation that is used in our analyses.

2.2   Spectral Budget Formulations

As mentioned in the previous section, Lorenz defined the APE as an integral quantity for the whole atmosphere. In order to define an APE spectrum and spectral budget in analogy to those for the KE, we first define the APE per unit mass as a function of space and time as (e.g., see Brune and Becker (2013), their Appendix B):

$$APE = \frac{g^2 \widetilde{T}^2}{2\overline{N^2}\overline{T}^2} = C\frac{1}{2}\widetilde{T}^2, \qquad (2.26)$$

where,

$$\overline{N}^2 = \frac{g}{\overline{T}}\left(\frac{g}{c_p} - \frac{gp}{R\overline{T}}\partial_p\overline{T}\right),\tag{2.27}$$

is the horizontally averaged Brunt–Väisälä frequency. The corresponding APE budget in grid space is derived[11] from the enthalpy equation (2.4) and for simplicity, we derive it in the pressure coordinates. We group the right-hand side contributions into 5 main terms and they are given as;

$$\partial_t APE = \underbrace{-\vec{v}_h \cdot \vec{\nabla}_h APE}_{\text{Horizontal Advection of APE}} \quad \underbrace{-\omega\partial_p APE}_{\text{Vertical Advection of APE}}$$
$$+\underbrace{\left(1 + \frac{\widetilde{T}}{\overline{T}}\right)\frac{R}{p}\widetilde{T}\omega}_{\text{Negative Buoyancy Production}} \quad +\underbrace{\frac{g^2}{c_p\overline{N}^2\overline{T}^2}\widetilde{T}Q}_{\text{Diabatic Heating}} \tag{2.28}$$
$$\underbrace{-\omega APE\frac{\partial_p\overline{N}^2}{\overline{N}^2}}_{\text{Vertical Exchange of APE}}\quad.$$

As it is discussed in Brune and Becker (2013), the last term in the right-hand side of equation (2.28) appears since the local APE in equation (2.26) is only an approximation. Its contribution is negligible if $\widetilde{T} << \overline{T}$. In order to formulate the spectral budget of APE, we use the expansion of the temperature into series of spherical harmonics[12] at a model layer l;

$$T_l(\lambda, \phi, t) = \sum_{m,n} T_{lmn}(t)Y_{nm}(\lambda, \phi),\tag{2.29}$$

such that the horizontally averaged APE at a given model layer l is calculated as:

$$APE_l = \frac{C_l}{8\pi}\int_{-1}^{1}\int_0^{2\pi} T_l^2\, d\lambda\, dsin\phi = \frac{C_l}{8\pi}\int T_l^2\, d\Omega = \frac{C_l}{8\pi}\sum_{m,n}(T_{lmn})^2.\tag{2.30}$$

Accordingly, the spectral APE contained in each total wavenumber n and model layer l can be written as a summation over zonal wavenumber m;

$$APE_{ln} = \frac{C_l}{8\pi}\sum_{m=-n}^{n}(T_{lmn})^2.\tag{2.31}$$

For $n = m = 0$, $APE_{ln} = 0$, such that equation (2.31) is valid for $n \geq 1$. This equation shows that the APE spectrum is the power spectrum of the temperature. Accordingly,

---

[11] For the derivation of the APE budget please refer to Appendix B

[12] Spherical harmonics, Y_{nm}, are real and normalized in the KMCM.

the spectral tendency for the APE budget can be defined as;

$$\partial_t APE_{ln} = \frac{C_l}{4\pi} \sum_{m=-n}^{n} (T_{lmn} d_t T_{lmn}). \tag{2.32}$$

The spectral APE budget is computed from equation (2.32) by substituting $d_t T_{lmn}$ by the individual spectral contributions to the prognostic spectral temperature tendency. These spectral contributions are in analogy to the grid-space tendency terms in right-hand side of equation (2.28). The explicit form of this spectral budget equation and the labels of the spectral APE tendency contributions that we use to refer frequently in our study are given as;

$$
\underbrace{\partial_t APE_{ln}}_{\text{Tendency of APE, } \mathbf{APE_t}} = \underbrace{\frac{C_l}{4\pi} \sum_{m=-n}^{n} \left[T_{lmn} \int (-\vec{v}_h \cdot \vec{\nabla}_h T)_l Y_{nm} \, d\Omega \right]}_{\text{Horizontal Advection of APE, } APE^{HA}}
$$
$$
+ \underbrace{\frac{C_l}{4\pi} \sum_{m=-n}^{n} \left[T_{lmn} \int (-\dot{\eta}\partial_\eta T)_l Y_{nm} \, d\Omega \right]}_{\text{Vertical Advection of APE, } APE^{VA}}
$$
$$
+ \underbrace{\frac{C_l}{4\pi} \sum_{m=-n}^{n} \left[T_{lmn} \int \left(\left(1 + \frac{\widetilde{T}}{\overline{\overline{T}}}\right) \frac{R}{p} \widetilde{T}\omega \right)_l Y_{nm} \, d\Omega \right]}_{\text{Negative Buoyancy Production, } APE^{NBP}} \tag{2.33}
$$
$$
+ \underbrace{\frac{C_l}{4\pi} \sum_{m=-n}^{n} \left[T_{lmn} \int Q_l Y_{nm} \, d\Omega \right]}_{\text{Diabatic Heating, } APE^{DH}}
$$
$$
+ \underbrace{\frac{C_l}{4\pi} \sum_{m=-n}^{n} \left[T_{lmn} \int \left(-\frac{\widetilde{T}}{2\overline{N}^2} \dot{\eta}\partial_\eta \overline{N}^2 \right)_l Y_{nm} \, d\Omega \right]}_{\text{Vertical Exchange of APE, } APE^{VE}},
$$

where η denotes the terrain following vertical hybrid coordinate (Simmons and Burridge (1981)) used in the KMCM. It should be noted that although the theoretical formulation of our APE budget is in pressure coordinates, we perform the budget calculations in the hybrid coordinates. The resulting discrepancies in the spectral APE budget analyses that are due to this difference between the theory and implementation are discussed in detail in chapter 4. Throughout our analyses (unless otherwise specified), we normalize each tendency term with the APE_{ln} at its corresponding total wavenumber n, in order to highlight the mesoscale contributions. The spectral flux of

any right-hand side spectral budget contribution from equation (2.33) is calculated as;

$$FAPE_{ln}^{[\ldots]} = \sum_{i=n}^{N_{cut}} APE_{ln}^{[\ldots]}, \tag{2.34}$$

where N_{cut} is the truncation wavenumber. In equations (2.28) and (2.33) we added the frictional heating ϵ to the differential heating term and named the resulting total diabatic heating as Q. The contributions to Q consist of;

- Horizontal frictional dissipation, $\epsilon_h = K_h|\mathbf{S}_{h0}|^2$

- Vertical frictional dissipation, $\epsilon_z = K_z(\partial_z \vec{v})^2$

- Horizontal diffusion of sensible heat, $\mu_h = \vec{\nabla}_h \cdot \left(c_p \frac{K_h}{Pr_h} \vec{\nabla}_h T \right)$

- Vertical diffusion of sensible heat, $\mu_z = \partial_z \left(\frac{T}{\theta} \frac{K_z}{Pr_z} \partial_z \theta \right)$

- Prescribed cumulus heating in tropics, Q_c

- Self-induced condensational heating in midlatitudes, $Q_m = \frac{|\omega| He(-\omega)}{\omega_m}$

- Temperature relaxation as a surrogate for radiative heating, $Q_{rad} = -\frac{T - T_c}{\tau}$

Detailed descriptions of Q_{rad}, Q_c and Q_m can be found in Schaefer-Rolffs and Becker (2018). Diffusion of sensible heat and frictional heating consists of vertical and horizontal parts.

Additionally, we also analyze the KE Budget. Its calculation is directly adopted from Brune and Becker (2013). Below we briefly recapitulate the calculation of the KE Budget. The velocity field in KMCM in grid space at a given model layer l based on spectral state variables of horizontal divergence, i.e D, and relative vorticity, i.e. ξ, is given as;

$$\vec{v}_{hl} = \sum_{n=1}^{N_{cut}} \frac{a_e^2}{n(n+1)} \sum_{m=-n}^{n} \left(\xi_{lmn}(\vec{e}_z \times \vec{\nabla}_h Y_{mn}) + D_{lmn} \vec{\nabla}_h Y_{mn} \right), \tag{2.35}$$

where a_e denotes the Earth's radius. Equation (2.35) is based on the Helmholtz decomposition on the sphere, which can be written as;

$$\vec{v}_h = \vec{e}_z \times \vec{\nabla}_h \psi + \vec{\nabla}_h \chi, \tag{2.36}$$

19

where ψ is the streamfunction and χ is the velocity potential. They are related to ξ and D as follows;

$$\xi = \vec{\nabla}^2 \psi, \tag{2.37}$$

$$D = \vec{\nabla}^2 \chi. \tag{2.38}$$

The corresponding tendencies of ξ and D in grid-space are given below. We also group the right-hand side contributions of these tendencies according to KE budget into 4 main terms:

$$\partial_t \xi = \vec{\nabla}_h \times \left[\underbrace{\vec{v}_h \times (f + \xi)\vec{e}_z}_{\substack{\text{Hor. Adv.} \\ \text{of KE from } \dot{\xi}}} \quad \underbrace{-\dot{\eta}\partial_\eta \vec{v}_h}_{\substack{\text{Ver. Adv.} \\ \text{of KE from } \dot{\xi}}} \quad \underbrace{-\frac{RT}{p}\vec{\nabla}_h p}_{\substack{\text{Adiab. Conv.} \\ \text{of KE from } \dot{\xi}}} \quad \underbrace{+\vec{R}}_{\substack{\text{Hor. Mom. Diff.} \\ \text{of KE from } \dot{\xi}}} \right] \cdot \vec{e}_z,$$

$$\partial_t D = \vec{\nabla}_h \cdot \left[\underbrace{\vec{v}_h \times (f + \xi)\vec{e}_z - \vec{\nabla}_h \left(\frac{\vec{v}_h^2}{2} \right)}_{\substack{\text{Hor. Adv.} \\ \text{of KE from } \dot{D}}} \quad \underbrace{-\dot{\eta}\partial_\eta \vec{v}_h}_{\substack{\text{Ver. Adv.} \\ \text{of KE from } \dot{D}}} \quad \underbrace{-\frac{RT}{p}\vec{\nabla}_h p - \vec{\nabla}_h \Phi}_{\substack{\text{Adiab. Conv.} \\ \text{of KE from } \dot{D}}} \quad \underbrace{+\vec{R}}_{\substack{\text{Hor. Mom. Diff.} \\ \text{of KE from } \dot{D}}} \right]$$

$$\tag{2.39}$$

The horizontally averaged KE at a model layer l is defined as;

$$KE_l = \frac{1}{4\pi} \int \left(\frac{\vec{v}_{hl}^2}{2} \right) d\Omega. \tag{2.40}$$

The spectral KE per unit mass at a model layer l using equation (2.35) is written as;

$$KE_{ln} = \frac{a_e^2}{8\pi n(n+1)} \sum_{m=-n}^{n} (\xi_{lmn}^2 + D_{lmn}^2), \tag{2.41}$$

such that

$$KE_l = \sum_{n=1}^{N_{cut}} KE_{ln}. \tag{2.42}$$

As it can be seen from equation (2.41), KE spectrum is the sum of the power spectra of relative vorticity and horizontal divergence. Based on this form we can easily construct a budget equation for KE since the tendencies of the prognostic variables ξ and D are explicitly computed in the KMCM. The tendency of the spectral KE at a model layer

is given by;

$$\partial_t KE_{ln} = \frac{a_e^2}{4\pi n(n+1)} \sum_{m=-n}^{n} (\xi_{lmn}\partial_t\xi_{lmn} + D_{lmn}\partial_t D_{lmn}).$$ (2.43)

The explicit form of the spectral KE budget (by using $\mathcal{C}_n = \frac{a_e^2}{4\pi n(n+1)}$ to simplify the form of the equation) and the corresponding labels of the spectral contribution terms that we use in our study are given below:

$$
\underbrace{\partial_t KE_{ln}}_{\text{Tend. of KE, } \mathbf{KE_t}} = \mathcal{C}_n \sum_{m=-n}^{n} \left[\begin{array}{l} \xi_{lmn} \int \left((\vec{v}_h \times (f+\xi)\vec{e}_z)_l \times \vec{\nabla}_h Y_{nm} \right) \cdot \vec{e}_z \, d\Omega \\ - D_{lmn} \int \left((\vec{v}_h \times (f+\xi)\vec{e}_z)_l \cdot \vec{\nabla}_h Y_{nm} + \frac{\vec{v}_{hl}^2}{2} \vec{\nabla}_h^2 Y_{nm} \right) d\Omega \end{array} \right] \left.\begin{array}{c} \\ \\ \\ \end{array}\right\} KE^{HA}
$$

$$
+ \mathcal{C}_n \sum_{m=-n}^{n} \left[\begin{array}{l} \xi_{lmn} \int \left((-\dot{\eta}\partial_\eta \vec{v}_h)_l \times \vec{\nabla}_h Y_{nm} \right) \cdot \vec{e}_z \, d\Omega \\ - D_{lmn} \int \left((-\dot{\eta}\partial_\eta \vec{v}_h)_l \cdot \vec{\nabla}_h Y_{nm} \right) d\Omega \end{array} \right] \left.\begin{array}{c} \\ \\ \\ \end{array}\right\} KE^{VA}
$$

$$
+ \mathcal{C}_n \sum_{m=-n}^{n} \left[\begin{array}{l} \xi_{lmn} \int \left(-\left(\frac{RT}{p} \vec{\nabla}_h p \right)_l \times \vec{\nabla}_h Y_{nm} \right) \cdot \vec{e}_z \, d\Omega \\ - D_{lmn} \int \left(-\left(\frac{RT}{p} \vec{\nabla}_h p \right)_l \cdot \vec{\nabla}_h Y_{nm} + \Phi_l \vec{\nabla}_h^2 Y_{nm} \right) d\Omega \end{array} \right] \left.\begin{array}{c} \\ \\ \\ \end{array}\right\} KE^{AC}
$$

$$
+ \mathcal{C}_n \sum_{m=-n}^{n} \left[\begin{array}{l} \xi_{lmn} \int \left(\vec{R}_l \times \vec{\nabla}_h Y_{nm} \right) \cdot \vec{e}_z \, d\Omega \\ - D_{lmn} \int \left(\vec{R}_l \cdot \vec{\nabla}_h Y_{nm} \right) d\Omega \end{array} \right] \left.\begin{array}{c} \\ \\ \\ \end{array}\right\} KE^{MD}
$$

(2.44)

Spectral flux of any right-hand side contribution from equation (2.44) is defined as;

$$FKE_{ln}^{[\ldots]} = \sum_{i=n}^{N_{cut}} KE_{ln}^{[\ldots]},$$ (2.45)

Chapter 3

Scale Invariant Horizontal Diffusion

According to conventional wisdom, the necessity for horizontal diffusion in GCMs is mainly a numerical problem, but not related to any physical process. Accordingly, ad hoc methods such as hyperdiffiusion and numerical filters are used to remove energy from the flow at the smallest resolved scales. These methods violate elementary hydrodynamical conservation laws and thus lead to non-negligible globally averaged energy imbalances, which result from the neglect of the frictional heating Becker (2003b). In chapter 2 we already established the relationship between the parameterized turbulent momentum diffusion term $\vec{R}$ and the frictional heating term ϵ. In the following, we explain in detail how these terms are related, which constraints should be taken into account for a physically consistent turbulent closure to simulate Lorenz Energy Cycle in high resolution GCMs in a consistent fashion. In subsection 3.2 we highlight the necessity of extending these concepts to horizontal sensible heat diffusion and present preliminary results regarding its importance in terms of mesoscale energy cascades.

3.1 Horizontal Momentum Diffusion and Scale Invariance Concept

A GCM cannot solve the Navier-Stokes equations because this would require spatial resolutions smaller than the Kolmogorov scale, which is about 1 cm in the troposphere. Nevertheless, the dissipation of energy by molecular viscosity and heat conduction at scales smaller than the Kolmogorov scale must be accounted for. As noted earlier, the dissipation of KE in the atmosphere is mainly due to surface friction (Becker (2003b)) or boundary layer turbulence in a more general sense (van Mieghem (1973)). The

dissipation of kinetic energy is given by the molecular frictional heating per unit mass:

$$\epsilon = \frac{1}{\rho}(\mathbf{P}\vec{\nabla}) \cdot \vec{v}. \tag{3.1}$$

In equation (3.1) $\mathbf{P}$ is the viscous stress tensor, $\vec{\nabla}$ is the 3 dimensional gradient operator and $\vec{v}$ is the three dimensional velocity vector. This term is positive definite and occurs as an internal heating rate at the right-hand side of the enthalpy equation per unit mass.

Due to the wide range of scales of motion required to properly simulate the atmospheric dynamics, the Navier-Stokes cannot be solved in atmospheric circulation models. Therefore we need to work with a narrower range of scales of motion and average over the smaller scales that are not explicitly accounted for. Such an averaging leads to the necessity to specify the Reynolds stress tensor term, i.e. $\mathbf{\Sigma}_3 = -\overline{\rho \vec{v}' \circ \vec{v}'}$, which describes the fluxes of momentum of the SGS motion and the index 3 indicates that both horizontal and vertical momentum diffusion is considered in this general form. In this notation, primes, i.e. ( )$'$, denote the spatial scales that are smaller than the resolution scale and the overline, i.e. $(\overline{})$, represents the spatial average over the resolution scale and the symbol $\circ$ denotes the tensor product. Parameterization of $\mathbf{\Sigma}_3$ is an indispensable part of any circulation model.

Fluid dynamical numerical simulations that employ a parameterization of the Reynolds stress tensor are generally known as the Large Eddy Simulation (LES). A widely used concept in turbulence closure methods within the LES framework is the generalization of the mixing-length approach of Ludwig Prandtl that was originally proposed by Joseph Smagorinsky (Smagorinsky (1963)). In LES, the molecular viscous stress tensor can usually be dropped since the resolution scale is much larger than the microscale such that the explicit contributions from $\mathbf{P}$ in the momentum equation are negligible. Since KMCM is an hydrostatic model, vertical velocities and accordingly the vertical momentum are also not considered. Furthermore, in the context of GCMs, mesoscales assume strongly anisotropic dynamics such that we also need an anisotropic turbulence closure. Accordingly, the Reynolds stress tensor of the horizontal momentum with its horizontal and vertical components can be given as;

$$\mathbf{\Sigma} = \mathbf{\Sigma}_h + \mathbf{\Sigma}_z, \tag{3.2}$$

where the horizontal and vertical stress tensors are defined in analogy to Fickian dif-

fusion as;

$$\mathbf{\Sigma}_h = \rho K_h \mathbf{S}_{h0}, \tag{3.3}$$

$$\mathbf{\Sigma}_z = \rho K_z \mathbf{S}_{z0}. \tag{3.4}$$

In equations (3.3) and (3.4) K_h, K_z, $\mathbf{S}_{h0}$ and $\mathbf{S}_{z0}$ are the horizontal diffusion coefficient of horizontal momentum, vertical diffusion coefficient of horizontal momentum, horizontal shear stress tensor and vertical shear stress tensor of horizontal momentum, respectively. It is of particular importance that the shear stress tensors in spherical geometry are symmetric, otherwise, the elementary constraint of the Eulerian law of angular momentum conservation is not fulfilled for finite control volumes (Serrin (1959), Becker (2001)). The shear stress tensors that we used in equations (3.3) and (3.4) comply with this constraint and they are defined as following;

$$\mathbf{S}_{h0} = \left[\left(\vec{\nabla}_h + \frac{\vec{e}_z}{a_e}\right) \circ \vec{v}_h\right] + \left[\left(\vec{\nabla}_h + \frac{\vec{e}_z}{a_e}\right) \circ \vec{v}_h\right]^T - D(\vec{e}_x \circ \vec{e}_x + \vec{e}_y \circ \vec{e}_y), \tag{3.5}$$

$$\mathbf{S}_{z0} = \vec{e}_z \circ \partial_z \vec{v}_h + \partial_z \vec{v}_h \circ \vec{e}_z, \tag{3.6}$$

where $\vec{e}_x$ and $\vec{e}_y$ denote the zonal and meridional unit vectors, respectively[1]. The index 0 in equations (3.3) and (3.4) indicates that the trace of the shear stress tensors are 0. The diffusion coefficients K_h and K_z are modeled analogously to Prandtl's mixing length ansatz (Prandtl (1942)). Their nonlinear forms are given as;

$$K_h = l_h^2 |\mathbf{S}_{h0}|, \tag{3.7}$$

$$K_z = l_z^2 |\partial_z \vec{v}_h|, \tag{3.8}$$

where l_h and l_z are the horizontal and vertical mixing lengths and the symbol $|\ |$ represents the Frobenius norm. Modeling of $\mathbf{\Sigma}$ with a symmetric stress tensor that also has the anisotropic nonlinear diffusion coefficients in equations (3.7) and (3.8) with constant mixing lengths is known as the Classical Smagorinsky model (hereafter: SMAG, Becker and Burkhardt (2007)). With the turbulence closure details for a GCM considered so far, we can finally express the turbulent diffusion term in equation (2.1)

---

[1] For the mathematical definitions of the gradients of the unit vectors in spherical coordinates, please refer to the Appendix of Becker (2001).

as;

$$\vec{R} = \frac{RT}{p}\vec{\nabla}\left(\frac{p}{RT}K_h\mathbf{S}_{h0}\right) + \frac{RT}{p}\partial_z\left(\frac{p}{RT}K_z\partial_z\vec{v}_h\right). \tag{3.9}$$

The form of the symmetric stress tensors defined in equations (3.5) and (3.6) ensure the positive definiteness of the frictional heating in accordance with the second law of thermodynamics as well as for the energy conservation law for arbitrary fluid volumes (Lindzen (1990), Becker (2003a)). This can be seen by explicitly writing ϵ with taking $\mathbf{\Sigma}_h$ and $\mathbf{\Sigma}_z$ defined as above;

$$\begin{aligned}
\epsilon &= \frac{1}{\rho}(\mathbf{\Sigma}_h\vec{\nabla}_h)\cdot\vec{v}_h + \frac{1}{\rho}(\mathbf{\Sigma}_z\vec{\nabla}_z)\cdot\vec{v}_h \\
&= K_h(\mathbf{S}_{h0}\vec{\nabla}_h)\cdot\vec{v}_h + K_z(\vec{e}_z\circ\partial_z\vec{v}_h + \partial_z\vec{v}_h\circ\vec{e}_z) \\
&= \underbrace{K_h|\mathbf{S}_{h0}|^2}_{\epsilon_h} + \underbrace{K_z(\partial_z\vec{v}_h)^2}_{\epsilon_z}.
\end{aligned} \tag{3.10}$$

The formalism behind the equation (3.10) assumes a quasi-stationary turbulent KE (TKE) equation, such that the formal frictional heating is the so-called shear production of the TKE. In the quasi-stationary TKE equation, this production is balanced by the dissipation from the molecular viscosity plus the buoyancy production.

The dynamics of resolved circulation not only require a proper representation of irreversible processes that fulfills elementary fluid mechanical constraints but also need to be able to account for the energy cascades in a physically consistent fashion. In this regard, the form of the nonlinear diffusion coefficient in equation (3.7), i.e. K_h, has proven to allow for a realistic simulation of the enstrophy cascade at synoptic scales with a -3 exponential spectral slope in a coarse resolution GCMs (Becker and Burkhardt (2007)). However, synoptic scales include also a small but non-negligible net forward energy cascade that feeds the forward energy cascades in the mesoscales. High-resolution simulations with the KMCM showed that the SMAG does not allow to simulate a realistic spectral behavior in the mesoscale (Brune and Becker (2013), Schaefer-Rolffs and Becker (2013), Schaefer-Rolffs and Becker (2018)). Moreover, the spectral KE increases with wavenumber close to the resolution scale, which is known as spectral blocking (Boyd (2001)). Thus an additional treatment for the energy accumulation at the high wavenumber end (which is mainly composed of ageostrophic modes) is needed.

The first successful simulation of the $-5/3$ exponential slope in the mesoscales using

a high-resolution GCM that included no (artificial) hyperdiffusion or numerical filtering methods was presented by Schaefer-Rolffs and Becker (2018). Their SGS parameterization was based on the so called Dynamic Smagorinky Model (DSM, Germano et al. (1991)). The fundamental idea behind the DSM is to introduce a space and time dependent variability of the mixing length. Such a variability is introduced in following form;

$$l_h^2 = c_s^2 \overline{\Delta} = \frac{|\mathbf{L}|}{|\mathbf{M}|} \overline{\Delta}, \tag{3.11}$$

where $\overline{\Delta}$ denotes the resolution scale and c_s is the dimensionless Smagorinsky parameter. We calculate this parameter as the ratio of norms of two tensors; namely the tensor $\mathbf{L}$, which is the Leonard tensor, and the tensor $\mathbf{M}$, which is the subgrid model kernel tensor (Sagaut (2006)). These tensors are constructed foremost by defining a filter scale ($\widehat{\Delta}$) that is larger than the resolution scale. The $\mathbf{L}$ is defined in analogy to the Reynolds stress tensor, assuming that the resolved winds of the GCM (indicated by overlining) are the smallest scales, and that we wish to estimate the Reynolds stress from the resolved scales smaller that $\widehat{\Delta}$. Thus, the definition of the tensor is written in components as;

$$L_{ij} = \widehat{\overline{v_i} \overline{v_j}} - \widehat{\overline{v_i}} \widehat{\overline{v_j}}, \tag{3.12}$$

The tensor $\mathbf{M}$, on the other hand, is defined in analogy with the Smagorinsky ansatz to describe the turbulent stress tensor due to resolved scales smaller than $\widehat{\Delta}$:

$$M_{ij} = -2\overline{\Delta}^2 \left[(\widehat{\Delta}/\overline{\Delta})^2 |\widehat{\overline{\mathbf{S}}}_{h0}| \widehat{\overline{S}}_{h0ij} - \widehat{|\mathbf{S}_{h0}| \overline{S}_{h0ij}} \right]. \tag{3.13}$$

In this definition of $\mathbf{M}$, the values of c_s with respect to the resolution scale and the filter scale are assumed to be the same. If our SGS parameterization was perfect we can solve $\mathbf{L} = c_s^2 \mathbf{M}$ to obtain c_s^2. However, this equity is not valid for all tensor components in all circumstances. Therefore, to obtain a positive definite Smagorinsky parameter we use equation (3.11) to define the dynamic Smagorinsky parameter. In other words, when the tensor norms are applied on $\mathbf{L}$ and $\mathbf{M}$, we ensure that the Smagorinsky parameter and consequently the dynamic diffusion coefficient K_h are positive definite, as we have shown in equation (3.10). Recently, the DSM was further developed and made independent of the resolution scale by introducing a second filter scale, denoted by $\widetilde{\Delta}^2$, which in terms of turbulence modeling concept is referred to as the generalized

---

[2] The symbols $(\overline{})$, $(\widetilde{})$ and $(\widehat{})$, which are used in this and next subsection, represent spectrally truncated spatial averages over a certain grid size. They should not be confused with the same

DSM (hereafter: gDSM, Schaefer-Rolffs (2017)).

In Figure 3.1, we show the comparison of temporally and vertically averaged KE spectra that is analyzed from 3 different KMCM runs, that utilizes different SGS schemes for the modeling of $\boldsymbol{\Sigma}$. These SGS schemes are two SMAG runs with different mixing length values and no numerical treatment for smallest scales and one gDSM run that utilizes DSM only for horizontal momentum diffusion, therefore labeled as "gDSM-Mom.". One SMAG run has $l_h^2 = 11.4\text{km}^2$, therefore labeled as "SMAG_11.4". The other has $l_h^2 = 22.8\text{km}^2$ and labeled as "SMAG_22.8". Temporal average is over 16 model days and vertical averaging is done between 300 and 150hPa altitudes. We first notice that the KE spectra for planetary and synoptic scales do not have a significant difference among these runs. This is not surprising since as we discussed earlier, the enstrophy cascades in synoptic scales (between $n \sim 10$ and $n \sim 50$) are well captured by the SMAG scheme. However, towards higher wavenumbers, where the direct energy cascades start to dominate over the enstrophy cascades in mesoscales, we see a clear difference among KE spectra with respect to the spectral KE amplitude and the shape of the curves. Both SMAG runs are incapable of simulating a realistic flattening of the mesoscale spectra. For "SMAG_11.4" KE spectrum, the difference is less in comparison to the gDSM run at the wavenumber of the mesoscale kink ($n \sim 120$), however, there is no simulated exponential $-5/3$ spectral slope in mesoscales. For "SMAG_22.8" there is not even a shallowing of the KE spectrum around the kink observed from the measurements of Nastrom and Gage (see Figure 2.3) such that the -3 spectral slope extends well into the mesoscales.

The main reason behind the proper shallowing in simulated mesoscales from the gDSM-Mom. run has to do with the fact DSM takes into account another physical constraint that has to be fulfilled in the governing equations of the model. This constraint is known as scale-invariance. It requires that every term of the governing equations that is relevant at the scales of a turbulent or macro-turbulent inertial range must keep its form in the case of a scale transformation. Recently, Schaefer-Rolffs et al. (2015) developed a Scale-Invariance Criterion (SIC) for LES parameterizations. Later on, this criterion was also applied to the geophysical fluid dynamical equations (Schaefer-Rolffs (2019)).

---

symbols from other chapters and subsections, which represent temporal or grid space averages such as horizontal or zonal means.
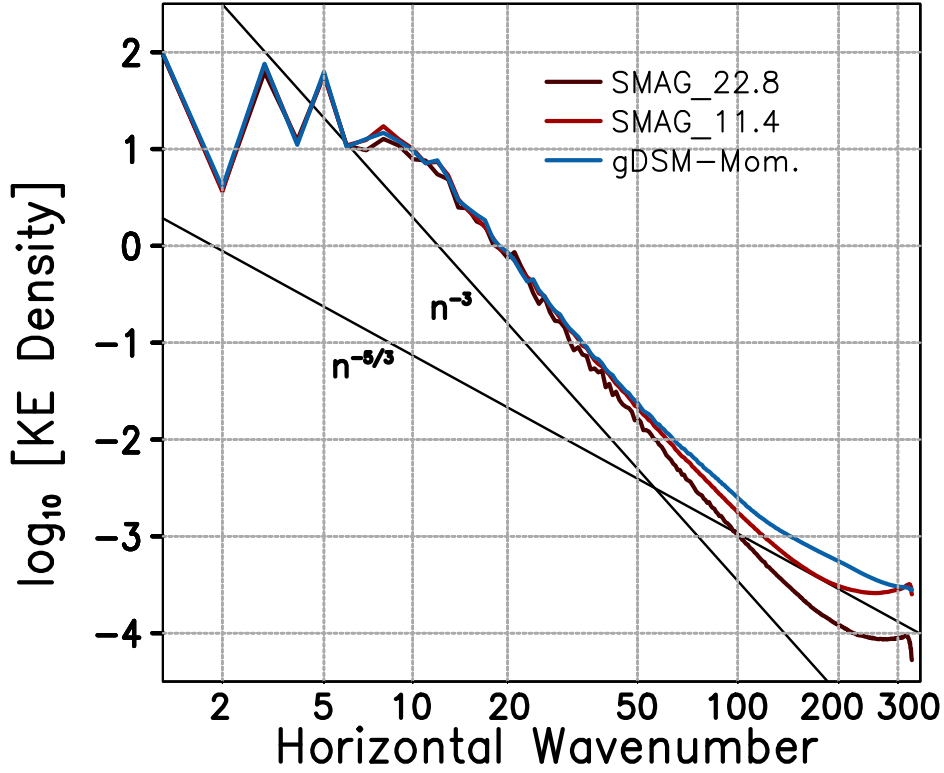
Figure 3.1: 16 days of temporally and vertically averaged KE spectral densities as a function of the total horizontal wavenumber n, from 3 different KMCM runs. Vertical averaging is done between 300 and 150hPa altitudes. For the description of the difference between the runs, please refer to the text. Black solid lines are labeled with their corresponding values of their spectral slope. Units of the KE spectra are in m^2/s^2.

The SIC can be used to determine whether a given parameterization scheme fulfills the aforementioned scale-invariance for the inertial range it is supposed to represent. Schaefer-Rolffs et al. (2015) confirmed that the constant mixing length formulation of the SMAG is not scale invariant, whereas the DSM and consequently the gDSM parameterization do preserve its form under scale transformations. As mentioned above, numerical models of geophysical fluid dynamics usually do not converge with increased resolution. The reason is that they usually do not comply with all the relevant physical constraints, unless the parameterizations that they employ are compatible with these laws.

3.2 Implementation of Scale Invariant Horizontal Diffusion

In previous subsection, we discussed the need for a scale invariant turbulent closure for a spectrally truncated momentum equation in order to account for the proper mesoscale cascade of KE. In this subsection, we extend the same concept to the closure of the sensible heat equation in order to properly account for the APE cascade and discuss the results with regard to the implementation of a scale invariant diffusion scheme. For this purpose, we start with the definition of the diffusion of sensible heat.

The rate of heating per unit volume of air via heat conduction (represented as ρQ_{sens}) is governed by heat fluxes across the boundaries of that volume. By denoting this heat flux as $\vec{W}$, the heating rate per unit mass is given as:

$$Q_{sens} = -\frac{1}{\rho}\vec{\nabla} \cdot \vec{W}. \tag{3.14}$$

The heat flux due to molecular heat conduction is formulated based on Fourier's Law (Fourier (1878)) and written as follows;

$$\vec{W} = -\kappa\vec{\nabla}T, \tag{3.15}$$

where κ is the material conductivity. When Reynolds averaging is applied to the equation (2.4), the eddy sensible heat flux has the form;

$$\vec{W}_t = c_p\bar{\rho}\overline{\overline{T''\vec{v}''}}, \tag{3.16}$$

where, $(\overline{\overline{}})$ denotes the density weighted spatial averaging over the resolution scale and $(\ )''$ denotes the small scale fluctuations over the density weighted averaging. In the lower and middle atmosphere, the contribution of $\vec{W}$ is negligible in the thermodynamic equation for the scales resolved even by high-resolution atmospheric circulation models. Following van Mieghem (van Mieghem (1973), his chapter 7), the eddy flux can be written in terms of a pressure perturbation and entropy perturbation (since according to turbulent mixing length assumption of Prandtl, it is the entropy that is conserved before it is mixed with the ambient flow). The pressure perturbation part can be neglected for the turbulence parameterization, since turbulent fluxes are local. The

entropy perturbation part can be rewritten in terms of potential temperature by making use of the anelastic approximation for resolved mesoscales[3]. With these modifications, the final form of the equation (3.16) at the resolution scale is as follows;

$$\vec{W}_t = c_p \overline{\overline{T}} \, \overline{\overline{\theta}}^{-1} \overline{\rho} \, \overline{\overline{\theta'' \vec{v}''}}. \tag{3.17}$$

The conventional way to parameterize the eddy flux of sensible heat is to adopt some form of a Fickian diffusion in analogy to equation (3.15). For this ansatz, we firstly assume anisotropy due to strong stratification of the atmosphere (i.e. $\vec{W}_t = \vec{W}_{ht} + \vec{W}_{zt}$) since the divergences of horizontal and vertical eddy sensible heat flux densities are comparable such that the horizontal sensible heat diffusion coefficient would be much larger than the vertical sensible heat diffusion coefficient. Furthermore, it is common practice to introduce turbulent horizontal and vertical Prandtl numbers, and to employ the horizontal and vertical momentum diffusion coefficients divided by the respective Prandtl number as turbulent heat diffusion coefficients. Noting furthermore that $\overline{\overline{T}} \, \overline{\overline{\theta}}^{-1} \vec{\nabla}_h \overline{\overline{\theta}} \approx \vec{\nabla}_h \overline{\overline{T}}$, this leads to the following ansatz (with dropping the double overbars) for the macro-turbulent sensible heat flux density (e.g., Becker (2003a), Becker (2017)) :

$$-\frac{1}{\rho}\vec{\nabla} \cdot \vec{W}_t = -\frac{1}{\rho}\vec{\nabla}_h \cdot \underbrace{\left(\underbrace{-c_p \rho \frac{K_h}{Pr_h} \vec{\nabla}_h T}_{\vec{W}_{ht}} \right)}_{\mu_h} \quad -\frac{1}{\rho}\partial_z \underbrace{\left(\underbrace{-c_p \rho \frac{T}{\theta} \frac{K_z}{Pr_z} \partial_z \theta}_{\vec{W}_{zt}} \right)}_{\mu_z}. \tag{3.18}$$

In equation (3.18) μ_h and μ_z represent the sensible heating rates per unit mass due to horizontal and vertical turbulent diffusion of sensible heat.

As we have explained in the previous section, the scale-invariance of the SGS horizontal momentum diffusion is crucial for the simulation of the KE cascades of the free atmosphere. It is worth noting that scale-invariance applies also not only with regard to the forward cascade of KE, but equally so for the forward cascade of APE. However, the conventional form of μ_h with constant horizontal turbulent Prandtl number, i.e. Pr_h, is not scale invariant, even if the diffusion coefficient from the DSM for the horizontal momentum equation is used. In order to fulfill the SIC for the eddy heat flux, we need to derive a dynamic horizontal Prandtl number (in what follows, we only consider the horizontal sensible heat diffusion). For this purpose, we have to introduce

---

[3] According to the anelastic approximation following holds: $\frac{T'}{T} = \frac{\theta'}{\theta}$ (Becker (2017)).

a second and a third filter scale[4] and consider the vector analogue of the Leonard Stress Tensor **L**;

$$\mathcal{L}_i = \widetilde{\widehat{\overline{v}_i \widehat{\overline{T}}}} - \widetilde{\widehat{\overline{v}}}_i \, \widetilde{\widehat{\overline{T}}} = \mathcal{T}_i - \widetilde{\tau}_i. \tag{3.19}$$

The vectors $\vec{\mathcal{T}}$ and $\vec{\tau}$ respectively correspond to the SGS horizontal sensible heat fluxes at the second $(\widetilde{\Delta})$ and first $(\widehat{\Delta})$ test filter scales, respectively. SGS horizontal sensible heat flux at the first filter scale is defined as;

$$\tau_i = -2\left(\frac{K_h}{Pr_h}\right)\partial_i\widehat{\overline{T}} = -2\left(\frac{c_s^2}{Pr_h}\widehat{\Delta}^2\right)|\widehat{\overline{\mathbf{S}}}_{h0}|\partial_i\widehat{\overline{T}}, \tag{3.20}$$

such that the corresponding subgrid model kernel vector is given as;

$$\mathcal{M}_i = -2\widehat{\Delta}^2\left[(\widetilde{\Delta}^2/\widehat{\Delta}^2)|\widetilde{\widehat{\overline{\mathbf{S}}}}_{h0}|\partial_i\widetilde{\widehat{\overline{T}}} - \widetilde{|\widehat{\overline{\mathbf{S}}}_{h0}|\partial_i\widehat{\overline{T}}}\right]. \tag{3.21}$$

Similar to the assumption made for c_s^2, Pr_h is assumed to be independent of the test filter scales. Consequently, the identity of Germano et al. (1991) applied to the turbulent sensible heat flux can be written as;

$$\mathcal{L}_i = \frac{c_s^2}{Pr_h}\mathcal{M}_i. \tag{3.22}$$

As in the case of scale invariant momentum diffusion, equation (3.22) is over determined, meaning that the value of Pr_h is not uniquely defined. We overcome this problem by invoking the second law of thermodynamics. In line with the condition imposed on the form of the parameterized stress tensor in the previous subsection, we require that the effective heat diffusion coefficient, i.e. $KT_h = \frac{K_h}{Pr_h}$, is positive definite such that the thermal dissipation from the heat diffusion parameterization is positive definite as well. This is a crucial requirement since we do not incorporate a prognostic turbulent parameterization.

The rate of change of entropy per unit volume due to the turbulent parameterization of heat diffusion and momentum diffusion can be written as:

$$\rho\partial_t s = -\frac{1}{T}\vec{\nabla}\cdot\vec{W}_t + \frac{1}{T}\epsilon. \tag{3.23}$$

---

[4] Here we directly impose the gDSM formalism that formulates the SGS stresses independently from the resolution scale. We calculate the different test scales with a double cut-off filter. Further details can be found in Schaefer-Rolffs (2017).

We have defined ϵ in previous subsection as a positive definite term, such that the contribution of mechanical dissipation to the entropy budget obeys the second law. We further rewrite the convergence of the eddy sensible heat flux as total boundary flux convergence and an additional entropy source with a temperature gradient;

$$\rho \partial_t s = -\vec{\nabla} \cdot \left(\frac{\vec{W}_t}{T} \right) - \frac{\vec{W}_t}{T^2} \cdot \vec{\nabla} T + \frac{1}{T} \epsilon. \tag{3.24}$$

The first term in the right-hand side of equation (3.24) represents the flux of entropy due to sensible heat diffusion across the boundary of a given air parcel and can be negative or positive. The second term is the internal entropy production due to the turbulent sensible heat flux, meaning that according to the second law of thermodynamics it has to be positive definite. Since we are only considering the implementation of a scale invariant horizontal diffusion of sensible heat in this study, we continue by writing this internal production term due to horizontal turbulent sensible heat diffusion with the SGS ansatz for $\vec{W}_{ht}$ in equation (3.18);

$$\rho \partial_t s_h^{internal} = \frac{c_p \rho \frac{K_h}{Pr_h} \vec{\nabla}_h T}{T^2} \cdot \vec{\nabla}_h T = c_p \rho \frac{K_h}{Pr_h} \frac{\vec{\nabla}_h T^2}{T^2}. \tag{3.25}$$

Hence, the thermal dissipation rate per unit mass due to horizontal heat diffusion must be written as :

$$T \partial_t s_h^{internal} = \sigma_{Th} = c_p \frac{K_h}{Pr_h} \frac{\vec{\nabla}_h T^2}{T}. \tag{3.26}$$

As it can be seen, the positive definiteness of σ_{Th} is only guaranteed if Pr_h is also positive definite[5]. Therefore, to fulfill the second law we define the dynamic horizontal Prandtl number as;

$$Pr_h = c_s^2 \frac{|\vec{\mathcal{L}}|}{|\vec{\mathcal{M}}|}. \tag{3.27}$$

The vector norms are defined as usual. Pr_h in equation (3.27) is a space and time dependent horizontal turbulent Prandtl number. Its distribution is governed by the temperature and velocity distributions, as well as by their gradients. Typically, the expansion of the horizontal derivative in μ_h includes 4 terms when the DSM scheme is applied. Since now we have a dynamic Pr_h with spatial and temporal variability, we add one more term in comparison to Becker and Burkhardt (2007) to the calculation

---

[5] Positive definiteness of K_h is given in equation (3.7) and the remaining terms are positive definite as well.

of the total SGS horizontal diffusion of sensible heat:

$$
-\frac{1}{\rho}\vec{\nabla}\cdot\vec{W}_{ht} = \underbrace{c_p\frac{K_h}{Pr_h}\vec{\nabla}_h^2 T}_{\mu_{h1}} + \underbrace{c_p\frac{l_h^2}{Pr_h}\vec{\nabla}_h(|\mathbf{S}_{h0}|)\cdot\vec{\nabla}_h T}_{\mu_{h2}} + \underbrace{c_p\frac{K_h}{\rho Pr_h}\vec{\nabla}\rho\cdot\vec{\nabla}_h T}_{\mu_{h3}}
$$
$$
+ \underbrace{c_p\frac{|\mathbf{S}_{h0}|\overline{\Delta}}{Pr_h}\vec{\nabla}_h(c_s^2)\cdot\vec{\nabla}_h T}_{\mu_{h4}} + \underbrace{c_p K_h\vec{\nabla}\left(\frac{1}{Pr_h}\right)\cdot\vec{\nabla}_h T}_{\mu_{h5}},
\tag{3.28}
$$

For the explicit form of μ_{h5} please refer to appendix C.

3.2.1 Model Specification

For our study regarding the complete scale invariant horizontal diffusion we perform global circulation experiments with the hydrostatic, high-resolution version of the KMCM(Becker (2003a), Brune and Becker (2013), Schaefer-Rolffs and Becker (2018)). The terrain following finite difference scheme of Simmons and Burridge (1981) in the vertical and spectral decomposition based on spherical harmonics in the horizontal directions (other spectral decomposition methods to describe and analyze the atmospheric global energy spectra have been proposed in the past as well, e.g. Žagar et al. (2015)) are used to solve for the following state vector;

$$
\vec{y}_{lnm} = \begin{bmatrix} \xi_{lnm} \\ D_{lnm} \\ T_{lnm} \\ p_{s,lnm} \end{bmatrix},
\tag{3.29}
$$

where $\vec{y}$ is composed of the relative vorticity ξ, horizontal divergence D, temperature T and surface pressure p_s. The index l enumerates the model levels, and n and m are the total horizontal wavenumber and zonal wavenumber, respectively. Our version of the KMCM employ 100 atmospheric levels. The highest level is in the lower mesosphere (~ 0.16hPa). The transformation from spectral space into physical space uses 512 Gaussian latitudes and 1024 equidistant longitudes. The tendency of $\vec{y}$ is integrated in time using the semi-implicit method as defined in Simmons and Burridge (1981), which is completed by a time filter (Asselin (1972)).

Except for the self-induced condensational heating in middle latitudes, the differen-

tial heating of the KMCM used in this study is similar to that used in the Held-Suarez benchmark test (Held and Suarez (1994)). This heating is specified to generate permanent January conditions. We use the full world orography in our model. However, this orography is strongly smoothed such that no orographic gravity waves are generated.

We performed several simulations with different model setups regarding the horizontal diffusion scheme. After equilibration of the model dynamics, we saved the last 16 days of each simulation. In the next sub-subsection we present the results from these simulations with respect to the nature of the simulated energy cascades in the mesoscales of the UTLS altitudes.

3.2.2 Results Regarding Scale Invariant Horizontal Diffusion

We have already seen the significant effect that scale-invariance of the horizontal momentum diffusion scheme has on the mesoscale energy cascades (see Figure 3.1). In Figure 3.2 we show the APE and KE spectra from 2 KMCM runs with different SGS schemes being used for the modeling of $\vec{W}_{ht}$. One employs the scale invariant gDSM scheme, and the other employs the SMAG scheme. Additionally, they both have the same scale invariant gDSM scheme for the modeling of Σ_h. Therefore, we label these runs as "gDSM-Mom." and "gDSM-Mom.+S.Heat". APE and KE spectra are averaged temporally for 16 days and vertically between 300 and 150hPa altitudes. As we can see from Figure 3.2a, the application of scale-invariance to the horizontal sensible heat diffusion did not introduce a significant change of the energy spectra at large and synoptic scales, as it should be. However, a close look on the mesoscales in Figure 3.2b reveals a clear improvement when the scale-invariance is accounted for also in the heat diffusion. The increase of APE with n at the highest wavenumbers that is seen with the gDSM-Mom. run is almost completely resolved with the new scheme. Both, the KE and APE spectra exhibit a $-5/3$ exponential spectral slope in the mesoscales down to the higher wavenumbers when we compare the dark green and light green curves to the dark blue and light blue curves. Or in other words, gDSM-Mom.+S.Heat run simulated the APE spectrum as expected from the Nastrom and Gage spectra (see Figure 2.3).

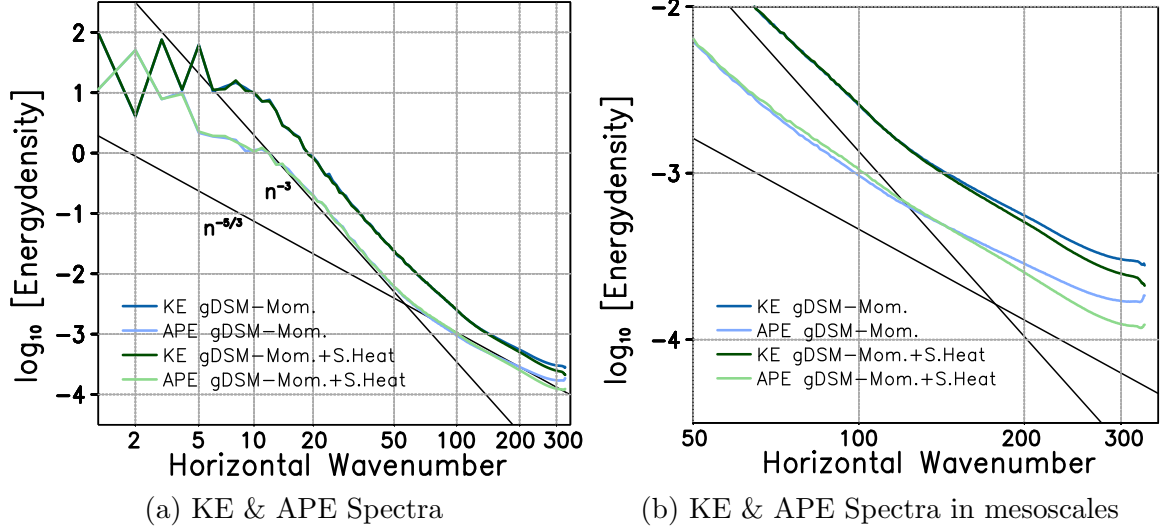(a) KE & APE Spectra   (b) KE & APE Spectra in mesoscales

Figure 3.2: (a) 16 days of temporally and vertically (between 300 and 150hPa altitudes) KE (darker colors) and APE (lighter colors) spectra from 2 different KMCM runs, which are labeled as gDSM-Mom.+S.Heat (green curves) and gDSM-Mom. (blue curves). For the description of the difference between the runs, please refer to the text. Black solid lines are labeled with their corresponding values of their spectral slope. (b) same as in (a), but zoomed on mesoscales. All spectra have units in m^2/s^2.

The observed slope of $-5/3$ of the atmospheric mesoscales hints to the existence of forward cascades of KE and APE. In order to further highlight the existence of this kind of macro-turbulence, we next look into the dissipation of both energies. This dissipation is expected to be in relation to the cascades since energy transfer to the smaller scales would essentially cross the threshold of the Ozmidov scale, beyond which the flow is isotropic due to negligible effect of the gravity force. In this regime, KT theory relates the amount of dissipated energy to the spectral energy flux at the Ozmidov scale. Since the forward macro-turbulent cascades in the atmospheric mesoscales are consistently accounted for by our scale invariant diffusion scheme, we can expect a similar balance between the forward spectral fluxes and the parameterized shear production as well as the thermal dissipation rate. Figure 3.3 shows the temporally (for 16 days) and zonally averaged horizontal turbulent diffusion coefficients and the horizontal dissipation rates of KE and APE with regard to the equations (3.10) and (3.26). As we mentioned in section 2.1, zonal mean is denoted by the square brackets, i.e. [ ]. The spatial correlation between $[K_h]$ and $[\epsilon_h]$ as well as between $[KT_h]$ and $[\sigma_{Th}]$ is a strong indicator of the existence of forward cascades of KE and APE. Furthermore, we notice from both Figures that the strongest forward cascades of energy take place in mid troposphere. This is not surprising since mid troposphere also accompanies the strongest enstrophy

cascade and KE injection due to breaking of baroclinic Rossby waves, which further results in the strongest direct energy cascades (Brune and Becker (2013)). A second region, where the forward cascades are pronounced, is at the subtropical midlatitudes and UTLS altitudes. Increased KE dissipation in these altitudes are associated with a vertical exchange of mesoscale KE, which are governed by the spontaneously generated primary Gravity Waves (GWs). Such vertical transport of mesoscale KE has been found in many GW resolving GCM studies (Koshyk and Hamilton (2001), Becker (2009), , Brune and Becker (2013), Augier and Lindborg (2013)). Once the primary GWs are generated in mid troposphere by the large scale flow, they travel upwards and contribute substantially to the forward energy cascades at UTLS heights by breaking and dissipating their energy.

(a) $[K_h]$ and $[\epsilon_h]$ (b) $[KT_h]$ and $[\sigma_{Th}]$
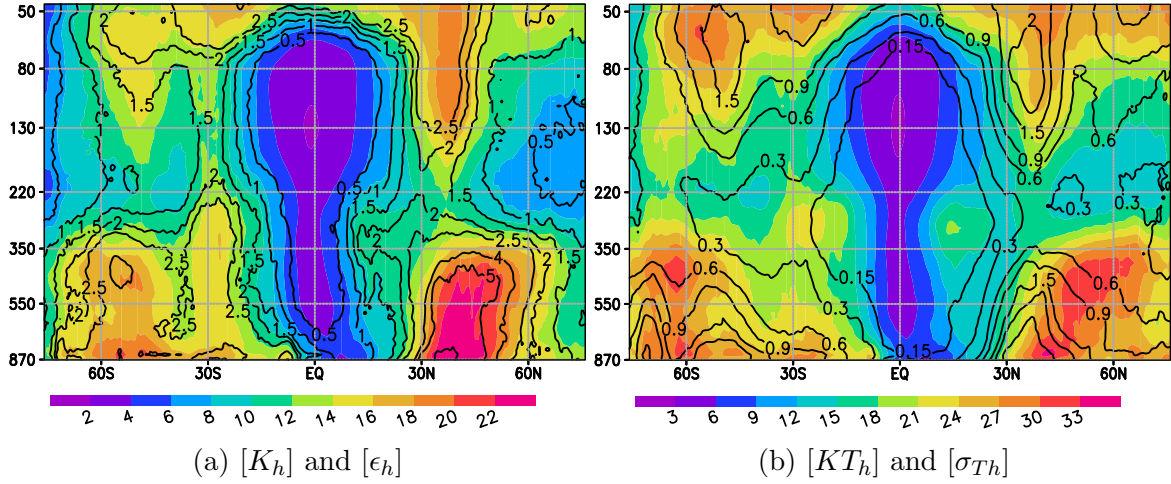
Figure 3.3: (a) Zonally and temporally averaged horizontal momentum diffusion coefficient (colors) and horizontal mechanical dissipation rate (contours with levels of 0.5 1 1.5 2 2.5 4 5 10 10^{-3}K/day) of KE. (b) Zonally and temporally averaged horizontal sensible heat diffusion coefficient (colors) and horizontal thermal dissipation rate (contours with levels of 0.15 0.3 0.6 0.9 1.5 2 3 10^{-3}K/day). Horizontal diffusion coefficients have units in 10^3m^2/s^2.

On the other hand, we see from Figures 3.3a and 3.3b that $[\epsilon_h]$ and $[\sigma_{Th}]$ have comparable values in the midlatitudinal UTLS. The fact that the mechanical and thermal dissipation rates have similar magnitudes in the UTLS confirms the existence of the forward cascades of both KE and APE with similar spectral fluxes, as is essential for the assumption that stratified macro-turbulence plays a major role in the mesoscale of the UTLS. Such dual cascades are also found in idealized ST theory of Lindborg, which provides a mechanism for a simulated $-5/3$ spectra for flows under strong stratification. It is remarkable that a similar type of dynamics is also observed in in the UTLS region of our January simulations.

36

Similar strengths of KE and APE spectral fluxes also imply that the turbulent Prandtl number would attain values close to 1 in these regions of pronounced forward cascades. Since our scale invariant diffusion scheme prognostically calculates a space and time dependent horizontal dynamic Prandtl number, we can investigate in zonally averaged picture if this argument holds. In Figure 3.4a we show the 16 days of temporally and zonally averaged horizontal dynamic Prandtl number. Similar to Figure 3.3, $[Pr_h]$ is also mostly pronounced at middle latitudes in both hemispheres and has distinct maxima in the mid troposphere and in the UTLS heights. In accordance with the previous discussion on the vertical exchange of mesoscale KE, mid tropospheric maximum of $[Pr_h]$ can be associated with the generation of primary GWs due to the breaking Rossby waves. And the second maximum in UTLS region is due to the dissipation of the energy of the primary GWs. Particularly, its value in these regions are strikingly close to 1. This is further evidence that the simulated KE-APE dual cascades are in similar strength as it is also predicted by the idealized ST theory. Figure 3.4 is also indicative of an additional maximum in the stratosphere above the equator. This maximum is located at 30 hPa(not shown), above which the sponge layer of the model starts to become active.

(a) $[Pr_h]$

(b) $\overline{Pr}_h$
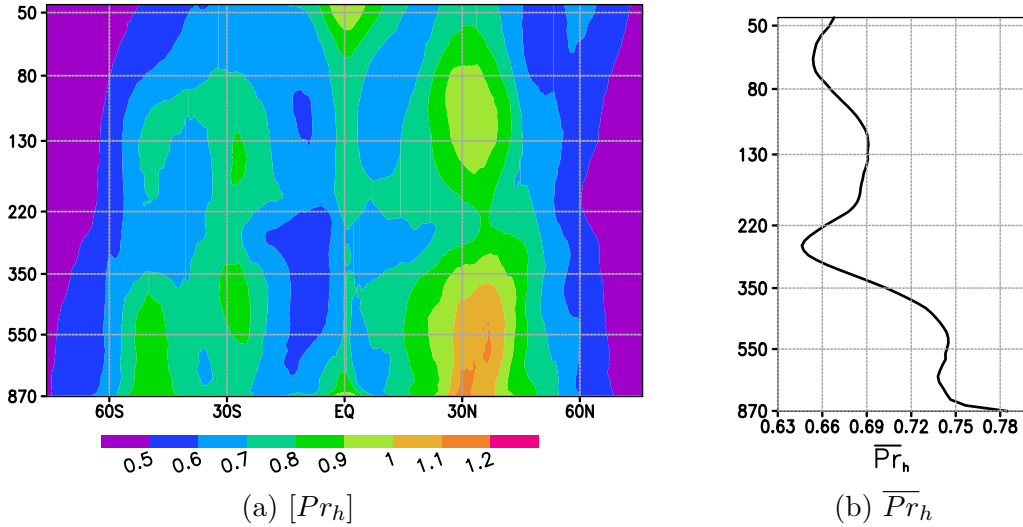
Figure 3.4: (a) Temporally and zonally averaged dimensionless horizontal dynamic Prandtl number, i.e. $[Pr_h]$. (b) Temporally averaged horizontal mean of horizontal dynamic Prandtl number, i.e. $\overline{Pr}_h$.

Horizontal mean (indicated with $(\overline{})$ symbol, as defined in section 2.1) of the dynamic Prandtl number in Figure 3.4b also has maxima in two different altitudes, namely mid troposphere and UTLS. Values of these maxima are less in comparison to the maxima we discussed above for Figure 3.4a due to the horizontal averaging, which also

includes the dynamically less active mesoscales of the poles. $\overline{Pr_h}$ in the UTLS ranges between $0.67 - 0.69$. Such values have also been hypothesized in the quasi-normal scale elimination (QNSE) theory for geophysical flows (Galperin and Sukoriansky (2010)) or in numerical studies of spectral eddy viscosity of ST (Remmler and Hickel (2014)).

We conclude this chapter by noting that there is a further significant feature found in our simulations when we apply our new, completely scale-invariant horizontal diffusion scheme. This effect is related to the simulation of saturated inertia GWs. An in depth discussion requires the analyses of the spectral budgets of APE and KE and the associated spectral fluxes, which we will address in chapter 5 (where we also investigate in detail the existence of ST in our simulations). Before we go into the detailed spectral study of the resolved mesoscales, we first provide an overview of resolved global scales in the next chapter using our spectral budget analyses that is described in section 2.2. Spectral budget analysis results for the planetary and synoptic scales are compared with similar GCM studies and with observational results with regard to the Lorenz Energy Cycle.

Chapter 4

Global Scale Analyses

In this chapter, we investigate the characteristics of both KE and APE at large scales based on spectral analyses using spherical harmonics. Particularly, the spectral APE properties are not thoroughly investigated in the literature although it is playing a crucial role in regulating the global circulation. Throughout this chapter, we compare KMCM results with the work of Steven J. Lambert on the vertically integrated spectral APE and KE budget analyses in terms of the two-dimensional total wavenumber for the First GARP Global Experiment (FGGE) year observations (Lambert (1984)). His calculations are based on the Global FGGE level III-b analyses of ECMWF reanalyses.

We start our discussion by comparing the small wavenumber behavior of the spectra of both energy reservoirs in Figure 4.1. APE and KE spectra from Figure 4.1b are calculated using a mass weighted vertical integration for 15 levels between 1000 and 10hPa for the month of January 1979. Similarly, KMCM spectra in Figure 4.1a are also calculated using a mass weighted vertical integration between 990 and 50hPa altitudes and also temporally averaged for 16 days. We did not include levels above 50 to exclude the effects of the sponge layer of the model that starts around 30hPa altitude. Both spectra share similar characteristics for the largest scales, i.e. $n < 7$. The distinct maxima of KE at odd wavenumbers for this range is an indicator of the symmetry of the zonal jets about the equator. Similarly, the maximum of APE at $n = 2$ is a reflection of the fact that the temperature has a maximum around the equator, which decreases towards the poles. The clear -3 slope beyond a total horizontal wavenumber of about 7 is associated with geostrophic turbulence, which is characterized by a net forward cascade of enstrophy Boer and Shepherd (1983). These features of both KE and APE regarding the planetary scales agree well between KMCM spectra and global-scale observations of Lambert (1984) as well as Boer and Shepherd (1983).

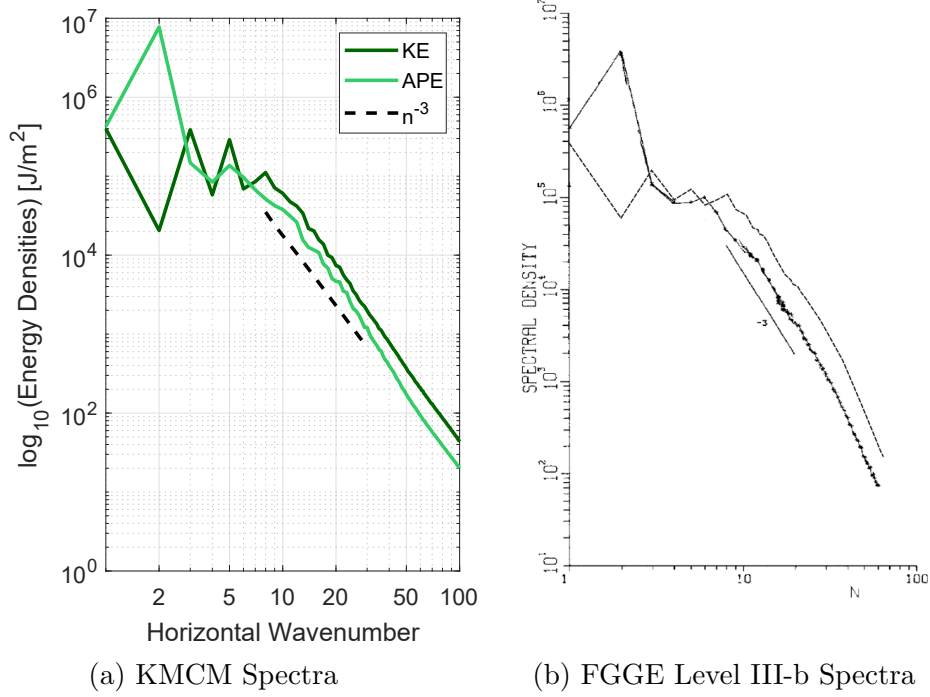(a) KMCM Spectra (b) FGGE Level III-b Spectra

Figure 4.1: (a) 16 days of temporally and vertically averaged KE and APE spectra from KMCM. Mass weighted vertical averaging is performed between 990 and 50hPa altitudes. (b) Reproduced KE (dashed curve) and APE (solid curve) spectra from Lambert (1984), for the month of January 1979. Spectra in both panels have units in J/m^2.

The dynamics for $n \geq 7$ is mainly governed by baroclinic instability. This means that the dynamics of the synoptic scales must be assessed by a coupled consideration of the KE and APE. A straightforward way to analyze the coupling between KE and APE is to investigate the respective horizontally averaged budgets. In order to simplify the calculations, we write the KE budget in the pressure coordinate system, which would be comparable with the APE budget formulation of equation (2.28) in section 2.2. Multiplying equation (2.1) by the horizontal velocity vector, the KE budget in grid space is given as;

$$\partial_t KE = -\vec{v}_h \cdot \vec{\nabla}_h KE - \omega \partial_p KE - \vec{v}_h \cdot \vec{\nabla}_h \Phi + \vec{v}_h \cdot \vec{R}. \qquad (4.1)$$

We further regroup the horizontal and vertical derivatives with the help of the hydrostatic equation and the continuity equation in pressure coordinates, i.e. $\frac{\partial \omega}{\partial p} + \vec{\nabla}_h \cdot \vec{v}_h = 0$. Following Lorenz (1955) we apply the horizontal mean to equation (4.1) and to the APE

40

equation (2.28) (see also Brune and Becker (2013), Apendix B);

$$\partial_t \overline{K_E} = -\partial_p(\overline{\omega K_E}) - \frac{R}{p}\overline{\widetilde{T}\omega} - \partial_p(\overline{\widetilde{\Phi}\omega}) + \overline{\vec{v}_h \cdot \vec{R}}, \qquad (4.2)$$

$$\partial_t \overline{APE} = -\partial_p(\overline{\omega APE}) + \frac{R}{p}\overline{\widetilde{T}\omega} + \frac{g^2}{c_p \overline{N}^2 \overline{T}^2}\overline{\widetilde{T}Q} + \left(\frac{2\overline{N}^2 R\overline{T}}{g^2 p} - \frac{\partial_p \overline{N}^2}{\overline{N}^2}\right)\overline{APE\omega}. \quad (4.3)$$

Furthermore, by integrating in vertical direction, vertical energy fluxes (i.e. $-\partial_p(\overline{\omega K_E})$, $-\partial_p(\overline{\widetilde{\Phi}\omega})$ and $-\partial_p(\overline{\omega APE})$) disappear due to the usual kinematic boundary conditions, i.e. $\omega = 0$ for $p = 0$ and for p_{00}, where p_{00} is a constant reference pressure. As we discussed in section 2.1 regarding the LEC, APE is generated by the 3rd term in the right-hand side of the equation (4.3). Generated APE is then converted to KE by the conversion term, which is the second term in equations (4.2) and (4.3). Generated KE is then dissipated by the last term in equation (4.2). It is then clear to see that a closed coupled budget for the atmosphere system regarding LEC is achieved only if the vertical exchange term of APE, i.e. the term multiplied with $\overline{APE\omega}$, is effectively 0[1]. We can directly calculate this term in wavenumber space from KMCM and compare with other budget contributions to check if this argument holds for our simulated 16 days of January. In Figure 4.2a we show the temporally (for 16 days) averaged spectral budget contributions to the spectral APE budget between 500 and 55hPa, as described in equation (2.33). All spectral contribution terms and the spectral total tendency of APE are summed over all wavenumbers. This is the same as horizontal averaging applied in equations (4.2) and (4.3), and it is indicated with the sum symbol, i.e. Σ, next to labels of APE budget terms in Figure 4.2a. It is clear to see from this figure that the horizontally and temporally averaged tendency of the APE (APE_t, black curve) is negligible in comparison to other terms, indicating that the 16 days of January simulations are well balanced, and that our account of the APE budget is accurate. The contribution from the vertical exchange term, APE^{VE}, is also insignificant with respect to other 4 contributing terms. This means that the assumption regarding the irrelevance of the vertical exchange of APE holds for our spectral APE budget calculation.

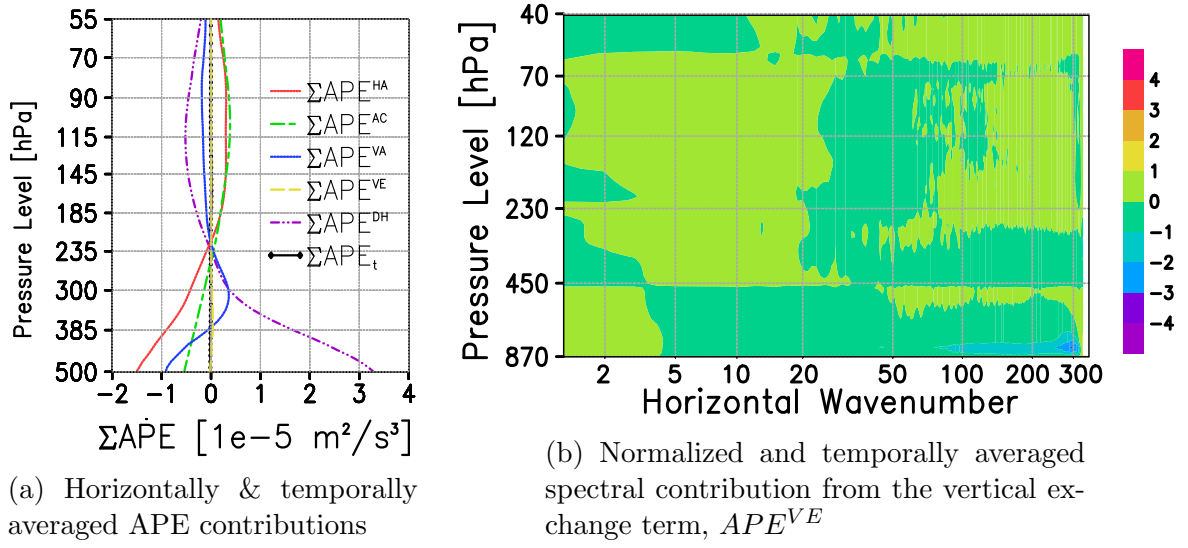[1] As we mentioned in section 2.1, dissipation of APE is neglected within the context of LEC.

(a) Horizontally & temporally averaged APE contributions

(b) Normalized and temporally averaged spectral contribution from the vertical exchange term, APE^{VE}

Figure 4.2: (a) 16 days of horizontally and temporally averaged budget contributions to the APE budget in units of $10^{-5} \mathrm{m}^2/\mathrm{s}^3$. Contributions are summed over all wavenumbers. Labels of these terms are provided in equation (2.33). (b) 16 days of temporally averaged spectral vertical exchange term contribution, i.e. APE^{VE} from equation (2.33), to the APE budget in units of $10^{-5} 1/\mathrm{s}$ that is normalized with APE_n for each wavenumber and level to highlight the mesoscale values.

Furthermore, in Figure 4.2b we show the APE^{VE} term as a function of the total wavenumber, n. The small contribution from this term at the mesoscales ($n > 100$) in the lower troposphere is an artifact due to formulating the APE budget in p-coordinates. Whereas the KMCM is formulated in a terrain following vertical hybrid coordinate system, and accordingly the APE budget is also calculated on hybrid levels without any interpolation of field variables to pressure coordinates. For the levels above mid troposphere p and η surfaces are similar and become identical above about 100hPa.

Equations (4.2) and (4.3) explicitly show that when vertically integrated, any net generation of KE is only possible via the buoyancy production term, i.e $-\frac{R\widetilde{T}\omega}{p}$. This coupling term transfers the APE that is generated by differential heating (3rd term in the right-hand side of the equation (4.3)) into KE. By vertically integrating our spectral budget formulations over certain altitude regimes we can investigate this statement for the large and synoptic scales.

In Figures 4.3a and 4.3b we show the vertically integrated and temporally averaged (for 16 days) KE and APE budgets for $n \leq 100$. Vertical integration is applied from 870 to 40hPa. The large-scale generation of APE by APE^{DH} at the smallest wavenumbers

represents the term G_Z in equations (2.22) to (2.25) that represent the decomposition of the global-mean APE and KE budgets according to Lorenz (1955). For $n < 10$, APE^{DH} includes positive contributions from the temperature relaxation term (Q_{rad}, which is a surrogate of the radiative heating), i.e. $APE^{DH_{Rad}}$, and the parameterized latent heating terms (Q_c and Q_m, see subsection 2.2), i.e. $APE^{DH_{Lat}}$. The strong energy input from APE^{DH} at planetary scales is balanced by the horizontal nonlinear advection term, i.e. APE^{HA}. For $n > 3$, APE^{HA} is positive. A closer inspection revealed that this term remains positive down to the resolution scale (not shown). This means that APE^{HA} transfer APE from planetary scales to synoptic scales and even to the mesoscales; it therefore corresponds to the C_A term in equations (2.22) and (2.23), which is the conversion of zonal-mean APE into eddy APE due to baroclinic instability. Note that the vertical advection term APE^{VA} shows a similar behavior like the $APE^{DH_{Rad}}$ and $APE^{DH_{Lat}}$, with a strong generation of APE at $n = 2$ and some destruction of APE at $n = 5$ and 6. The absolute values of APE^{VA} are, however, smaller than those from APE^{DH}. The large-scale generation of APE by vertical diffusion is caused by the differential heating due to surface sensible heat.

(a) APE Budget

(b) KE Budget
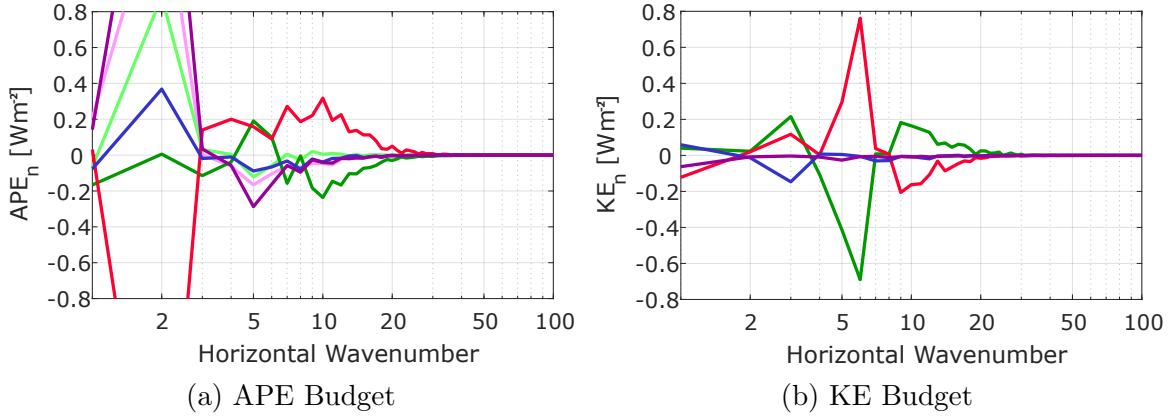
Figure 4.3: Vertically integrated (mass weighted, between 870 and 40hPa) and temporally (for 16 days) averaged spectral budget contributions for APE and KE for wavenumbers smaller than 100. Contributing terms are not normalized with the APE at the corresponding wavenumber as in Figure 4.2b and their units are in W/m². Terms and their respective colors for the curves are given as follows: APE^{HA}(——), APE^{VA}(——), APE^{NBP}(——), APE^{DH}(——), $APE^{DH_{Rad}}$(——), $APE^{DH_{Lat}}$(——), KE^{HA}(——), KE^{VA}(——), KE^{AC}(——), KE^{MD}(——).

The conversion term in the APE budget that is due to negative buoyancy production, i.e. APE^{NBP}, is positive for wavenumbers 5 and 6 and is negative or negligible otherwise. The corresponding adiabatic conversion in the KE budget, i.e. KE^{AC}, is opposite to this behavior. In fact, for all wavenumbers smaller than 100, APE^{NBP} and

KE^{AC} have opposite signs. Figure 4.3b indicates a positive conversion of APE into KE for $n = 3$, which is together with KE^{HA} balanced by the vertical advection of KE, i.e. KE^{VA}. A significantly negative value for KE^{AC} is found at wavenumbers 5 and 6 this time in balance with KE^{HA}. This behavior is mirroring the above mentioned balance between APE^{VA} and the large scale forcing terms at $n = 5$ and $n = 6$. Overall the dynamics in the regime between $n = 1$ and 8, which contains this alternating adiabatic conversion across wavenumbers between APE and KE and the subsequent distribution of energy via the nonlinear advective terms partially correspond to the simulated mean-meridional circulation in troposphere (Becker (2012)). The conversion term in this range corresponds to C_Z in equations (2.22) and (2.24). This picture regarding the simulated planetary scale energetics are in full accordance with the contributions to spectral APE and KE from global observations as reported by Lambert (1984) for the month of January. For wavenumbers beyond 10, we have no significant contribution from APE^{DH}, which is a further confirmation that the model does not include any significant generation of eddy APE, i.e. for our permanent January conditions G_E in equation (2.23) is negligible.

Regarding the synoptic scales from about $n = 7$ to $n = 30$, the spectral APE and KE budgets in Figure 4.3a and 4.3b show opposite behaviors regarding horizontal advection and adiabatic conversion. This finding is in accordance with the LEC. More specifically, KE is generated at the expense of APE via adiabatic conversion, which corresponds to positive C_E in equations (2.22) and (2.25). The APE at these scales is again maintained by a forward cascade due to APE^{HA}, which corresponds to the conversion of zonal-mean APE to eddy APE as mentioned above. This generation of KE from about $n = 7$ to $n = 30$ by adiabatic conversions is balanced by negative spectral contributions from KE^{HA}. This corresponds to the inverse energy cascade of geostrophic turbulence, or negative C_K in equations (2.22) and (2.25).

As mentioned in section 3.1, the forward cascade of enstrophy at synoptic scales (from about $n = 7$ to $n = 80$) gives rise to an n^{-3} KE spectrum (see Figure 4.1). Here, we are interested in the spectral budgets of KE and APE and how the spectra are related to the enstrophy cascade and the inverse KE cascade towards the planetary scales. To better analyze these energy transformations, we now consider the spectral fluxes instead of the spectral tendencies. Information as to how we calculate the spectral energy fluxes can be found in section 2.2. Please note that we label the flux of a certain budget term as $FKE^{[\ldots]}$ and $FAPE^{[\ldots]}$. In Figure 4.4a we show the 16 days of

temporally and mass weighted vertically integrated spectral fluxes of total nonlinear advection of KE, i.e. $FKE^{HA} + FKE^{VA}$. We perform the vertical integration for the spectral advective fluxes of KE and APE for all model layers, instead of between 870 and 40hPa altitudes. In Figure 4.4b we reproduced also the mass weighted vertically integrated total nonlinear advection flux of KE calculations from the global-scale observations as reported by Lambert (1984).

Comparison of Figures 4.4a and 4.4b shows that the spectral fluxes of KE due to total KE advection from the KMCM agree reasonably well with the analysis of Lambert, given the differences in the data sources computation methods. For the regime between wavenumbers $n = 3$ and $n = 20$ KE is transferred towards larger scales, which corresponds to $C_K < 0$ in equations (2.24) and (2.25). This inverse KE cascade from synoptic scales to planetary scales is about half a decade of wavenumbers wider in the KMCM when compared to the results of Lambert (1984). Its intensity is stronger as well since almost the double amount of energy flux exists for KMCM than the flux calculated from the FGGE Level III-b reanalyses. Consequently, the wavenumber at which total advective fluxes change direction to transfer energy to smaller scales is also different. Nearly constant flux of KE at the synoptic scales in KMCM simulations indicates that at a given wavenumber in this range KE is transferred to higher wavenumbers in a scale invariant fashion. In comparison Figure 4.4b shows a clear concave function property with a maxima around $n = 30$. This could be an indicator that the KE transfer to neighboring scales at this range of wavenumbers in the atmosphere is not solely due to freely cascading inertial forces. However, an alternative explanation according to Boer and Shepherd (1983) is that the neglect of the effect of SGS on the calculation of the global advective KE energy flux would result in such a pronounced maximum as well as the large non zero value at the largest wavenumber end of the assimilated observational data. Boer and Shepherd (1983) reported that by including a model that estimates the SGS scale effects that is based on the dissipation of enstrophy at an intermediate cutoff wavenumber n, they obtained a wider inverse energy cascading regime (similar to the KMCM result in 4.4a) for the estimated KE flux in comparison to the KE flux that is calculated only using the resolved observational data. Inclusion of the SGS effects mitigated the problems due to the nature of observational data and also resulted in a smoother increase of KE flux from inverse cascading regime to a direct cascading wavenumber without a pronounced maximum (not shown here, see Figure 13 from Boer and Shepherd (1983)).

45

(a) KMCM $HA + VA$ Flux for KE

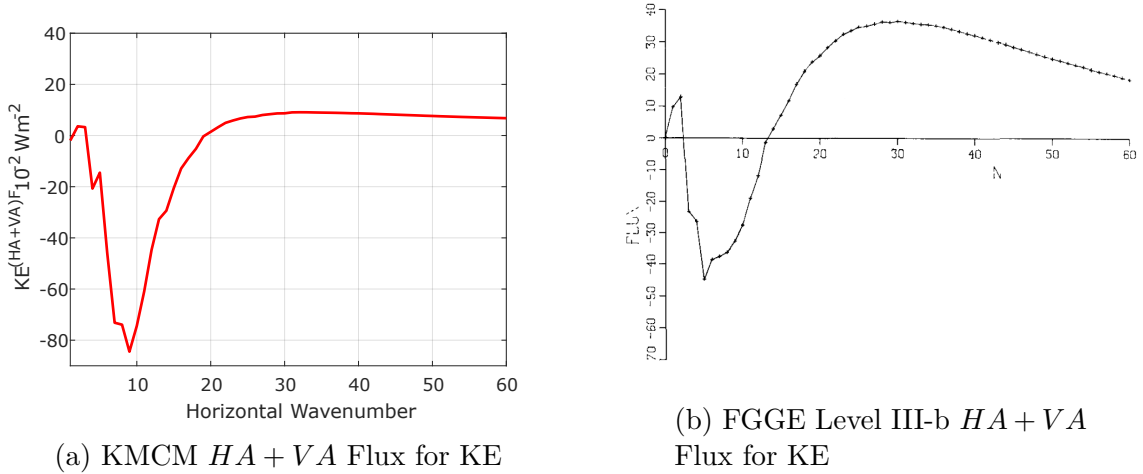(b) FGGE Level III-b $HA + VA$ Flux for KE

Figure 4.4: (a) 16 days of temporally and mass weighted vertically integrated (between the model surface and model top) total nonlinear KE flux from January simulations with the KMCM. (b) Global mass weighted vertically integrated and temporally averaged total nonlinear KE flux reproduced from the analyses of Lambert (1984) for the month of January 1979. Note that the KMCM result is plotted akin to Lambert's result in (b), i.e. for the range of wavenumbers $n = 0$ to $n = 60$. Curves in both panels have units in W/m^2.

We continue by comparing the total nonlinear advective flux of APE. Again, we show the temporally averaged and mass weighted vertically integrated total advective fluxes of APE from KMCM and Lambert's analyses. Similar to the comparison in Figure 4.4, $FAPE^{HA} + FAPE^{VA}$ in Figure 4.5a also shares similar features with the Lambert's analysis in Figure 4.5b. The peak at the lower wavenumbers followed by a strong decrease for the total nonlinear APE flux is in good agreement between the two results, although the peak from $FAPE^{HA} + FAPE^{VA}$ in KMCM at $n = 3$ shows much more strong downscaling of APE than the curve in Figure 4.5b. This forward spectral flux of APE is a further confirmation that the contributions from the spectral nonlinear advection terms of APE^{HA} and APE^{VA} partially correspond to $C_A > 0$ in equations (2.24) and (2.25), i.e. positive flux of the above mentioned energy transfer from the zonal-mean APE into eddy APE. An important difference between FGGE Level III-b reanalysis and KMCM simulation result is that for $n > 22$ the total advective flux for APE in Lambert's analysis is negative and decreasing with increasing n, whereas in the KMCM this flux is positive down to the truncation scale. These negative values for flux of APE in Figure 4.5b for $n > 22$ are deemed unrealistic by Lambert (1984) due to the inconsistencies at the smallest scales in the data for the month of January 1979. Nevertheless, the small but non-negligible continuous forward spectral flux of APE and KE in Figures 4.4a and 4.5a are further confirmation of

the dual forward energy cascades for both energy reservoirs, which is hidden behind the dominant forward enstrophy cascade in synoptic scales. Another important detail about the simulated globally averaged total spectral advective fluxes of KE and APE is that both spectral fluxes are equal to 0 at both ends of the resolved wavenumber range (values for $n > 60$ are not shown in Figures 4.4a and 4.5a). This means that the globally averaged nonlinear fluxes of KE and APE that are calculated from our spectral budget analyses are conservative and only act to redistribute the energy in a given wavenumber to other wavenumbers, as they should.

(a) KMCM $HA + VA$ Flux for APE

(b) FGGE Level III-b $HA + VA$ Flux for APE
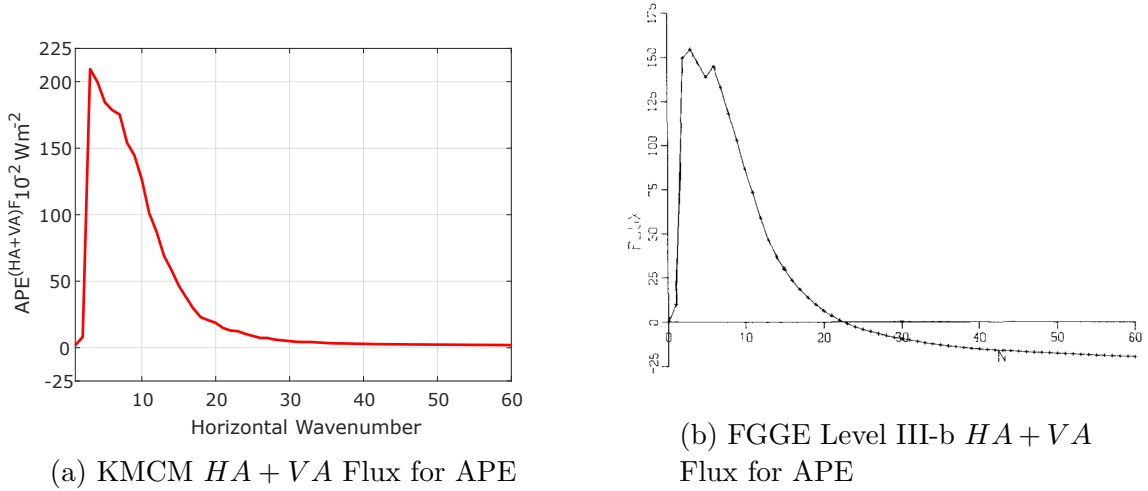
Figure 4.5: (a) Similar to Figure 4.4a, but for the total nonlinear APE flux from January simulations with the KMCM. (b) Similar to Figure 4.4b, but for the global total nonlinear APE flux reproduced from the analyses of Lambert (1984). Note that the KMCM result is plotted akin to the Lambert's result in (b), i.e. for the range of wavenumbers $n = 0$ to $n = 60$. Curves in both panels have units in W/m^2.

It should be noted that Figure 4.3 suggests that there are only two main mechanisms, which are dominant at synoptic wavenumbers , i.e. $n > 8$, and regulates the dynamics; namely the adiabatic conversion (or buoyancy production) and nonlinear horizontal advection of APE and KE. Therefore, in Figure 4.6 we show the temporally averaged and mass weighted vertically integrated adiabatic conversion fluxes from our January simulations with the KMCM and Lambert's analyses, as well as the adiabatic conversion flux, reproduced from the work of Augier and Lindborg (2013), who performed a globally averaged spectral KE and APE budget analyses on the GCM results based on the AFES model simulations for 10 days of the month of June (see Hamilton et al. (2008)). Adiabatic conversion flux from the KMCM is calculated using the $-FAPE^{NBP}$ term. It is temporally averaged for 16 days and mass weighted vertically integrated between 870 and 40hPa altitudes, as shown with the solid green curve in Fig-

ure 4.6a. In comparison to the calculation of the vertical averages of $FKE^{HA}+FKE^{VA}$ and $FAPE^{HA} + FAPE^{VA}$, we did not include all levels of the model for the vertical averaging of the $-FAPE^{NBP}$. This is because the APE^{NBP} term in equation 2.33 is in pressure coordinates, although we perform our calculations in terrain following hybrid coordinates. As we previously explained in this chapter for the case of APE^{VE}, the discrepancy between the two coordinate systems is pronounced the most at the lowest model layer and in order to mitigate numerical errors as much as possible, we again excluded these layers. Furthermore, the adiabatic conversion flux from Lambert's analyses is also plotted with the black curve in Figure 4.6a. This flux is calculated using the tabulated conversion tendency values from Lambert (1984) (see his Table 2) that are only provided until $n = 20$. We then used equation 2.34 for these tabulated conversion tendency terms to calculate the spectral conversion flux. This means that our calculation for this spectral flux is only an estimate of the actual globally assimilated data for the month of January from the FGGE year. Finally, the spectral flux of the adiabatic conversion tendency that we show in Figure 4.6b is reproduced from the analyses of Augier and Lindborg (2013) (see their Figure 1). This term is also calculated using a mass weighted vertically integration over the 24 model layers from the AFES model that extends until 1hPa altitude. For $\mathcal{C} > 0$, KE is converted to APE and vice versa in their framework. However, their analyses is performed directly on the pressure surfaces such that the conversion term is not subject to low level discrepancies as we explained before.

Model data and Lambert's analysis agree qualitatively well in Figures 4.6a and 4.6b for the largest scale. A globally averaged conversion rate around 1.93W/m² at $n = 0$ for $-FAPE^{NBP}$ is a reasonable value as we will explain later in this chapter, even though the lowermost model levels are highly unreliable in our calculations. As we mentioned in section 2.1, the globally averaged conversion rate is central within the context of LEC, since the KE generated via this conversion is ultimately balanced by the net diabatic heating of the atmosphere, i.e. the frictional heating due to destruction of the generated KE. Our calculation for the conversion flux of January from FGGE year at $n = 1$ gives a slightly larger value than 3W/m². This value was also reported from Lambert's dataset. Beyond $n = 20$ we only have data from GCMs to compare the characteristic of the conversion flux. For this range, KMCM and AFES differ in the sign of the spectral flux of APE due to adiabatic conversion (buoyancy production). For the KMCM, this spectral flux is positive at synoptic wavenumbers, while it is negative for

the AFES model. This discrepancy is due to the inaccuracy of the APE budget at the lowest model levels. As we will show in next chapter, the vertically integrated spectral flux of APE due to adiabatic conversion is not reflecting the typical behavior of this conversion in the high wavenumber regime at the free atmospheric altitudes, where we expect the ST type mesoscale macro-turbulent energy cascades to exist[2] Instead, it is negative for synoptic and mesoscales in the free atmosphere, similar to the AFES model result in figure 4.6b.
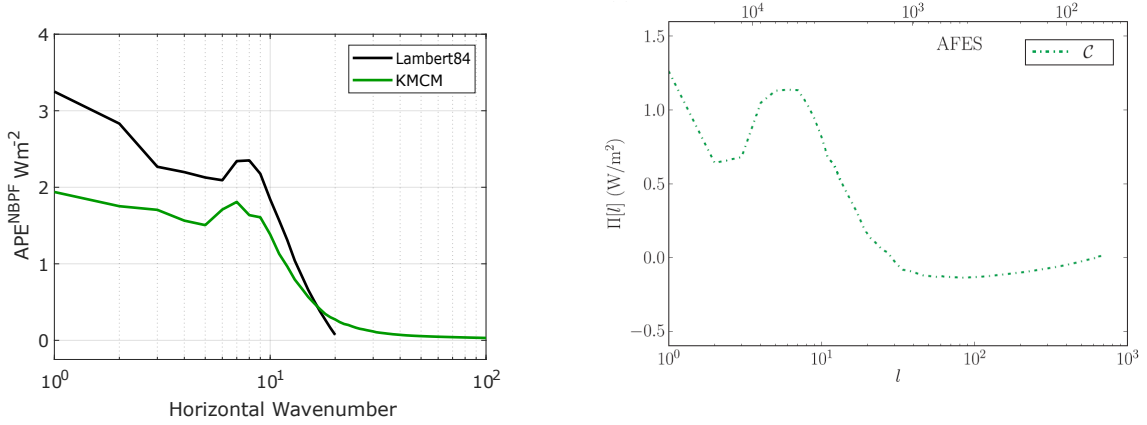
(a) KMCM & FGGE Level III-b AC Flux   (b) AFES Model AC Flux

Figure 4.6: (a) 16 days of temporally averaged and vertically integrated (mass weighted, between 870 and 40hPa) spectral flux of the adiabatic conversion tendency (solid green curve), i.e. $-FAPE^{NBP}$, from January simulations with the KMCM and also the reproduced spectral flux of the adiabatic conversion (solid black curve) based on Lambert's analyses for the month of January 1979. For the calculation details of the black curve, please refer to the text. (b) Globally averaged spectral flux of the adiabatic conversion tendency from the AFES model (see Hamilton et al. (2008)) and reproduced after the analyses of Augier and Lindborg (2013). l is the total horizontal wavenumber in their analyses. Curves in both panels have units in W/m².

Finally, to determine the intensity of the LEC simulated by the KMCM, we further calculated the temporally and globally averaged and vertically integrated adiabatic conversion rate in grid space using,

$$< AC >= -\frac{1}{g4\pi} \int_0^{p_s} \int_0^{2\pi} \int_{-1}^1 \left\langle -\vec{v}_h \cdot \vec{\nabla}_h \Phi - \frac{RT}{p} \vec{\nabla}_h p \right\rangle ds in\phi \, d\lambda \, dp, \qquad (4.4)$$

where, symbol $\langle \ \rangle$ represents the temporal averaging as we introduced in chapter 2 and triangular brackets, i.e. $< \quad >$, denote the vertically integrated global averaging.

---

[2] It should be noted that within the inertial range of idealized ST cascades for APE and KE the buoyancy production is negative, that is conversion is from KE to APE.

The second term in equation (4.4) with the horizontal pressure gradient appears in comparison to equation (2.1) because of the terrain following hybrid vertical coordinate system of the model. For our 16 days of January simulations, $< AC >$ was found to be about $2.19\mathrm{W/m}^2$. This corresponds to the exact simulated globally averaged conversion rate on a climatological timescale. It is more accurate than the value estimated by using the spectral $-FAPE^{NBP}$ term, since it does not suffer from the numerical discrepancies at the lowest model levels. Particularly, it agrees well with the eddy conversion term (C_E in equations (2.23) and (2.25)) from one of the earliest observation-based estimates of the intensity of the Lorenz Energy Cycle by Oort (1964). It also agrees reasonably well with more recent estimates based on climate models (Boer and Lambert (2008)).

The Lorenz energy cycle is simulated in a thermodynamically consistent fashion by models only if the adiabatic conversion rate is balanced by the net diabatic heating of the atmosphere, i.e. by the vertically integrated and globally averaged frictional heating (Lorenz (1967), Becker (2003b)). We also computed the globally averaged and vertically integrated vertical and horizontal dissipation rates from equation (3.10). A value of $\sim 2.26\mathrm{W/m}^2$ was found for total KE dissipation in the temporal mean, which is quite close to the value of $< AC >$. The main contribution to this net frictional heating is from vertical diffusion of the horizontal momentum in the atmospheric boundary layer, more specifically from the surface friction (Becker (2003b)). For our simulation we found $1.96\mathrm{W/m}^2$ for the net frictional heating due to vertical diffusion of the horizontal momentum. As noted by Becker (2003b), this frictional heating is not sufficient for thermodynamically consistent simulation of the Lorenz energy cycle, because the corresponding heating from horizontal momentum diffusion needs to be taken into account as well. Indeed, an inconsistent momentum diffusion and the resulting deficiency in frictional heating can easily lead to significant spurious radiative forcing in global climate models. According to Becker and Burkhardt (2007) and Schaefer-Rolffs and Becker (2018), $< \epsilon_h >$, that is the net frictional heating due to horizontal diffusion of the horizontal momentum, amounts to $\sim 0.33\mathrm{W/m}^2$. In our simulations we find a very similar value of $< \epsilon_h > \approx 0.3\mathrm{W/m}^2$. This horizontal dissipation is the end route of part of APE converted into KE that does not cascade upscale, but cascade downscale. This downscaling is part of the forward spectral KE flux in the mesoscales that is transferred from synoptic scales, which is due to the horizontal and vertical advection of horizontal momentum.

Summarizing, in this chapter we utilized new model results from the high-resolution

KMCM with a scale-invariant horizontal diffusion scheme for horizontal momentum and sensible heat, and we analyzed the vertically integrated spectral fluxes of KE and APE due to advection and adiabatic conversion (buoyancy production) from planetary to synoptic scales. Consistent with previous estimates, the KMCM simulates a reversed cascade of KE toward the planetary scales and a forward cascade at synoptic scales. We also confirmed that APE is subject to a forward cascade at all scales. Furthermore, the intensity of the Lorenz energy cycle in KMCM has realistic intensity and is simulated in a thermodynamically consistent fashion, that is, the global-mean (horizontally averaged and vertically integrated) adiabatic conversion of APE into KE is reasonably well balanced by the global-mean frictional heating. In the next chapter, we analyze the spectral budgets and fluxes in the mesoscales from the mid troposphere to the lower stratosphere in order to determine the mechanisms that give rise to the -5/3 power law in the Nastrom-Gage spectrum.

Chapter 5

Mesoscale Energy Cascades

In this chapter, we focus on the energy cascades in the mesoscales that gives rise to the $-5/3$ exponential spectral slope for both KE and APE for horizontal wavelengths that are typically smaller than 400 km (see Figure 2.3) in the upper troposphere and lower stratosphere (UTLS). Accordingly, this chapter is divided into two parts. The first part provides results from KMCM simulations that show the clear existence of the necessary conditions at UTLS altitudes that are needed for the emergence of the Stratified Macro-Turbulence (SMT). A level by level analysis of the spectral fluxes and budget contributions to both KE and APE, as well as the zonally averaged diagnosed ST statistics, highlight the similarities between the resolved SMT dynamics and the traditional picture of Stratified Turbulence (ST). The second part provides a theoretical interpretation of SMT with regard to saturated GWs and how the strongly nonlinear nature of these GWs accounts for a forward cascade of KE and APE. The simulation of saturated westward GWs in the UTLS lends further confidence to this interpretation. Our concluding results of this section accentuate the importance of scale invariant SGS diffusion for the forward energy cascades of the saturated westward GWs.

5.1 Stratified Macro-Turbulence in Mesoscales

Similar to classical isotropic KT, the $-5/3$ exponential spectral slope for the energy spectra in ST develops over an inertial range in which energy cascades to smaller scales. Stratification is a necessary condition for ST type inertial cascades to exist. In order to measure the strength of the stratification, the horizontal Froude number, i.e. Fr_h, is used. For given characteristic horizontal velocity U_h and horizontal length scale l_h, Fr_h can be written as:

$$Fr_h = \frac{U_h}{Nl_h}, \tag{5.1}$$

where N is the buoyancy frequency. $Fr_h << 1$ has been known as a necessary condition for ST to exist (Riley et al. (1981), Lilly (1983)) and more recently Lindborg (2006) noted that 0.02 is the maximum value for Fr_h that supports ST type cascades. However, even if the condition of $Fr_h << 1$ is fulfilled, ST may still not develop. This is true even in the case of very large horizontal Reynolds number, i.e. $Re_h = \frac{U_h l_h}{\nu} >> 1$, where ν is the kinematic viscosity. Reason for the inhibition of the ST in such cases is that multi-scale motion can still be averted by stratification if the vertical friction of horizontal momentum is comparable to the vertical advection of the horizontal momentum.

The cases, in which ST develops, can be identified from the equations of motion by invoking the hypothesis that ST should possess a self-similar scaling for its dynamics (just as in KT). This is done by defining a scale dependent aspect ratio for flows under stratification, i.e. $\alpha = l_h/l_v$, where l_v is the characteristic vertical length scale. In ST, l_h at the largest scale of the inertial range (i.e. the integral length scale of ST) is determined by the energy injection. Accordingly, due to the anisotropic nature of ST, most energetic structures evolve in the horizontal direction. Unlike l_h, l_v is not an imposed scaling parameter on the flow. Rather it is assumed that it adjusts dynamically to the given horizontal size of the eddies (Billant and Chomaz (2001)). By utilizing this α for the nondimensionalized equations of motion for a stratified, incompressible flow, two distinct dynamical regimes can be identified (Brethouwer et al. (2007)). Particularly, another dimensionless parameter that is based on the combination of the Re_h and Fr_h is used for identifying whether ST would develop or not for a given flow under stratification. Namely, if $Re_h Fr_h^2 = U_h^3/(N^2 \nu l_h)$ is very large than 1, then the viscosity in vertical direction is insignificant and ST inertial range develops. If it is smaller than or on the order of 1, large scale dynamics in vertical are determined by a balance between inertial and viscous forces, for which no energy cascade can occur. Similar to KT, the forward flux of KE in ST is also ultimately balanced by the KE dissipation. This balance at the Kolmogorov microscale corresponds to the well known estimate of Taylor (1935);

$$\epsilon \approx \frac{U_h^3}{l_h}.$$ (5.2)

By adopting this estimation, we may rewrite $Re_h Fr_h^2$ as;

$$Re_h Fr_h^2 = Re_b = \frac{\epsilon}{N^2 \nu}.$$ (5.3)

Re_b is known as the buoyancy Reynolds number (Smyth and Moum (2000), Brethouwer et al. (2007)). Therefore, when a stratified turbulent flow fulfills conditions of $Fr_h << 1$ and $Re_b >> 1$ then the ST dynamics prevail[1].

Accordingly, Fr_h and Re_b provide a consistent way to check for the possible existence of ST. We may apply equations (5.1) and (5.3) to our 16 days of January simulations for this purpose. To do so, we need to define the characteristic horizontal length and velocity scales for the UTLS mesoscales. For a given wavenumber n within the assumed SMT inertial range, the corresponding U_h can be defined as;

$$U_{h(n)} = \sqrt{2E_{KE(n)}} = \sqrt{2 \int_n^\infty e_{KE(n')} \, dn'}, \tag{5.4}$$

where e_{KE} is the horizontal spectral KE density and E_{KE} is the horizontal integral scale KE density at total wavenumber n. It has been long understood that the change of the exponential spectral slope from -3 to $-5/3$ is linked to the relative dominance of the spectral forward energy flux over the forward enstrophy flux (Tung and Orlando (2003), Brune and Becker (2013)). Although the exact wavenumber for which the forward energy flux starts to dominate varies with altitude, this variation is only modest in UTLS. According to our results in section 3.2.2, the mesoscale kink takes place around $n = 120$ (see Figure 3.2b). Therefore it is reasonable to select this wavenumber for the largest scale of SMT and to define the mesoscale velocities as;

$$\begin{aligned}
\vec{v}_{h(n \geq 120)} = &\sum_{n=1}^{N_{cut}} \frac{a_e^2}{n(n+1)} \sum_{m=-n}^{n} \left(\xi_{mn}(\vec{e}_h \times \vec{\nabla}_h Y_{mn}) + D_{mn} \vec{\nabla}_h Y_{mn} \right) \\
&- \sum_{n=1}^{120} \frac{a_e^2}{n(n+1)} \sum_{m=-n}^{n} \left(\xi_{mn}(\vec{e}_h \times \vec{\nabla}_h Y_{mn}) + D_{mn} \vec{\nabla}_h Y_{mn} \right)
\end{aligned} \tag{5.5}$$

where $N_{cut} = 330$. In equation (5.5) we simply subtract the large scale horizontal wind calculated from the spectral expansion between $n = 1$ and 120 from the horizontal wind calculated using the full spectral expansion. From this method[2] we can write the resolved mesoscale KE;

$$KE_{(n>120)} = \frac{|\vec{v}_{h(n \geq 120)}|^2}{2}. \tag{5.6}$$

---

[1] ST characterized by $Fr_h << 1$ and $Re_b >> 1$ is also known as the Strongly Stratified Turbulence (SST).

[2] The same method was used to calculate the mesoscale transient KE for mesospheric altitudes in Becker (2009).

For wavenumbers beyond the truncation scale, i.e. for $n > 330$, we have to diagnose the SGS KE. We calculate KE_{SGS} via the following relation;

$$KE_{SGS} = \sqrt{\frac{\epsilon K^{tot}}{C_\mu}}, \tag{5.7}$$

where K^{tot} is the total horizontal momentum diffusion coefficient. This form is adopted from Launder and Spalding (1973), where they relate the SGS energy to the diffusion coefficient of the turbulent flow and to the dissipation rate via the $k - \epsilon$ theory of turbulence. Value of C_μ is 0.09 and taken from their derivation. As a result, the characteristic horizontal velocity of SMT for KMCM can be defined as;

$$U_h = \sqrt{2(KE_{(n>120)} + KE_{SGS})}. \tag{5.8}$$

The corresponding characteristic horizontal length scale is calculated using equation (5.2):

$$l_h = \frac{U_h^3}{\epsilon}. \tag{5.9}$$

In the next subsection, we present results to investigate the existence of SMT in mesoscales with regard to the characteristic parameters and spectral nature of the idealized ST.

5.1.1 Indications of Idealized Stratified Turbulence in Mesoscales

Since $Fr_h << 1$ and $Re_b >> 1$ are necessary conditions for ST to exist, we are interested in finding the spatial correlations, where both of these dimensionless parameters are pronounced and have values that fulfill these conditions. Figures 5.1a and 5.1b show the temporally averaged zonal means of Fr_h and Re_b from equations (5.1) and (5.3) from lower troposphere up to 50hPa. Temporal average is over 16 model days. From Figure 5.1a we see that above 870hPa, all values are below 0.02, which means we have strong enough stratification according to the largest limit of $Fr_h = 0.02$ as noted by Lindborg (2006) for ST to exist. According to Figure 5.1a, Fr_h decreases from the tropics toward higher latitudes and from lower troposphere to the stratosphere. The low values of Fr_h found in our simulation of the atmosphere demand strong energy injection for SMT to develop. Figure 5.1b shows that the spatial distribution of Re_b is quite similar to that of Fr_h. More specifically, maximum values of Re_b are also

concentrated in the equatorial lower troposphere and decrease towards the poles and toward higher altitudes. Typical values in the mid troposphere at middle and lower latitudes are $Re_b \sim \mathcal{O}(10^4)$. Such values have also recently been reported from the Unmanned Aerial Vehicle measurements of turbulence parameters up to an altitude of ~ 4.5km in the vicinity of Shigaraki Observatory, Japan (Luce et al. (2019)). To our knowledge, there is no other observational study performed in troposphere and lower stratosphere that estimated the value of Re_b.

(a) $[Fr_h]$　　　　　(b) $[Re_b]$
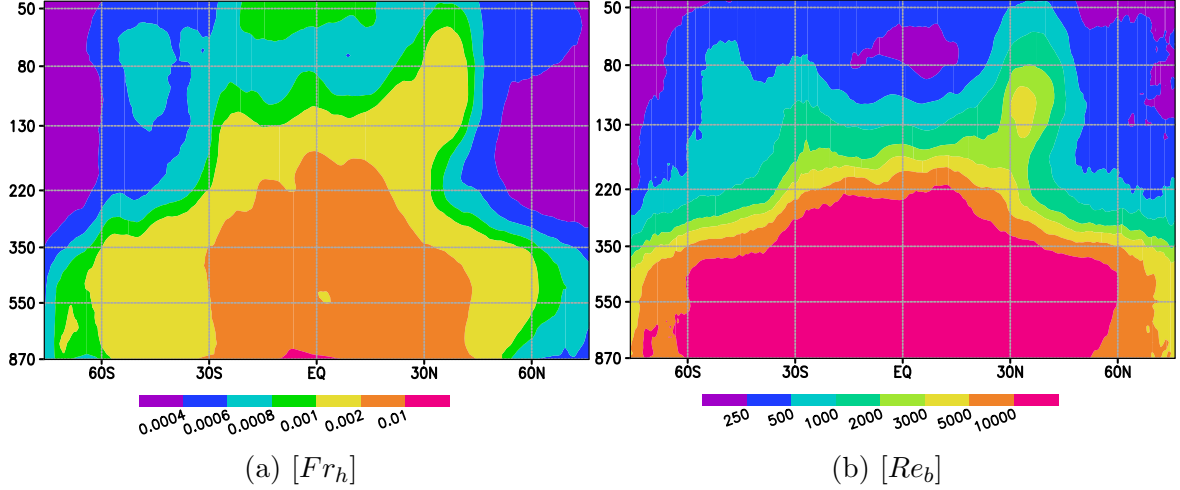
Figure 5.1: Zonally and temporally averaged dimensionless parameters of ST: horizontal Froude number in (a) and buoyancy Reynolds number in (b). Color increments are irregular for both panels.

For UTLS altitudes there are two pronounced regions for Re_b and Fr_h. The first one resides around northern subtropical mid-latitudes between 220 and 60hPa altitude. Here Re_b has a clear maximum between 150 and 95hPa. Fr_h does not display such a clear maximum in the same altitude and latitude range, even though Fr_h is maximum in the same area too. This spatial correlation is a strong indicator for the presence of pronounced macro-turbulent activity. A similar conclusion can be made also for the maximum around 50S latitude (summer hemisphere) and between 130 and 75hPa altitudes, which is less pronounced than the corresponding maximum in the winter hemisphere.

As shown by Riley and deBruynKops (2003), DNS of stably stratified flow with imposed forcing of the large-scale vertical vorticity component will develop small-scale turbulence (KT), when the conditions $Fr_h << 1$ and $Re_b >> 1$ are fulfilled. Furthermore, these authors showed that there is a significant increase of available potential energy over time, which was initially zero because the density field was horizontally

uniform. The spread of spectral energy for both APE and KE over time is possible because the KE injected at large scales cascades to smaller scales. Since Figures 5.1a and 5.1b indicate that $Fr_h \ll 1$ and $Re_b \gg 1$ holds at UTLS altitudes, we expect forward spectral fluxes of KE and APE in this regime. To test this hypothesis we use the horizontal advection flux terms for APE and KE that we defined in section 2.2, i.e. FKE^{HA} and $FAPE^{HA}$. Figure 5.2 shows temporally (for 16 days) and vertically (between 220 and 60hPa, in line with Figure 5.1) averaged nonlinear horizontal advection fluxes for KE and APE. Both FKE^{HA} and $FAPE^{HA}$ are positive throughout the subsynoptic and mesoscales wavenumbers, meaning both KE and APE cascade from large to small scales.
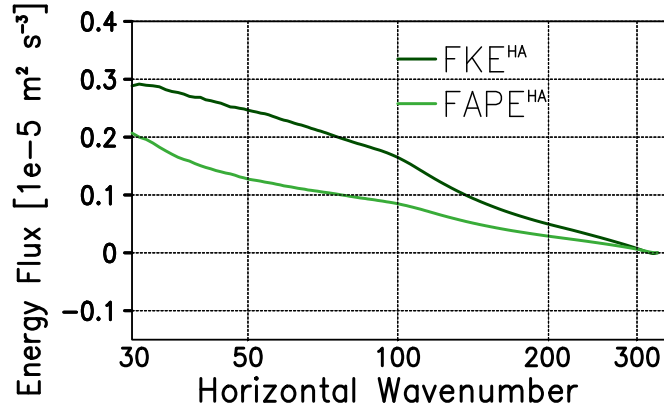
Figure 5.2: 16 days of temporally and vertically averaged horizontal advection fluxes of spectral KE and APE budgets. Vertical averaging is done between 220 and 60hPa. Units of the fluxes are in $10^{-5}\mathrm{m}^2/\mathrm{s}^3$. Note that the x-axis is zoomed in for total horizontal wavenumbers in the range of $30 > n > 330$.

Similar to KT, also SMT (and ST) should show spectral energy fluxes that are constant (independent of wavenumber) over the inertial range. Such constant spectral flux is not observed for the mesoscales in KMCM. We believe that this discrepancy is related to the underresolved vertical scales of SMT at UTLS altitudes. It has been long known that stratified turbulent flows are very demanding in terms of vertical resolution for DNS (Lindborg (2006)), LES (Khani and Waite (2014)) as well as for GCM (Skamarock et al. (2019)). For the LES of ST, Khani and Waite (2015) argued that in order to capture several key characteristics of ST, a maximum grid spacing of $\frac{\Delta}{L_b} < 0.24$ is required, where Δ is the resolution scale of the LES and $L_b = \frac{2\pi U_h}{N}$ is the buoyancy length scale of ST. L_b characterizes the thickness of the vertical structures of ST and marks the overturning scale of sheared layers (Waite and Bartello (2004), Waite (2011)). In order to assess whether the vertical spacing in KMCM meets this vertical

resolution limit for mesoscale cascades of KE and APE or not, we need an estimation of the spectral values of L_b that depend on the total horizontal wavenumber. For this, we need a characteristic horizontal velocity that is defined in wavenumber space. Following Brune and Becker (2013), we can calculate an integral scale horizontal velocity at a given wavenumber n as;

$$U_{(n)} = \sqrt{\sum_{n'=n}^{N_{cut}} e_{KE(n')}}. \qquad (5.10)$$

This allows to specify the buoyancy length scale of the resolved SMT as;

$$L_{b(n)} = \frac{2\pi U_{(n)}}{N}. \qquad (5.11)$$

Although (5.11) does not include a SGS velocity component like (5.8), $L_{b(n)}$ is still a useful variable to derive an estimate of the vertical resolution requirements to adequately simulate an SMT inertial range. The vertical grid spacing at UTLS altitudes in the high-resolution T330 version of KMCM is ~ 200m. As it can be seen from Figure 5.3, all mesoscale values of $L_{b(n)}$ ($n > 100$) are below the vertical resolution scale. Additionally, Waite (2016) argued that mixing length based vertical diffusion schemes for horizontal momentum and sensible heat that are modified with a Richardson number based stability criterion (which we also employ in the current version of the KMCM) also inhibit the occurrence of a constant spectral flux of energy by inducing a too strong vertical mixing. This effect likely prevents the development of a clean SMT inertial range in addition to the effect of a too coarse vertical numerical resolution. For the moment we have not further investigated the exact reason for not having constant spectral fluxes of KE and APE.
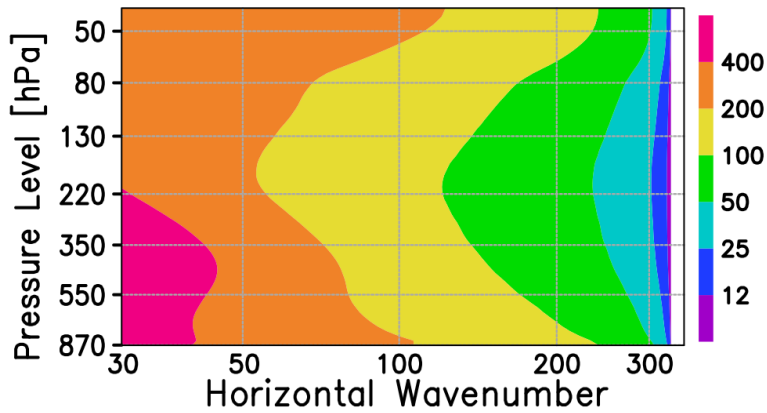
Figure 5.3: Buoyancy length scale (in units of m) as defined in equation (5.11). Note that, similar to Figure 5.2, the total horizontal wavenumber axis is zoomed.

Strong downscale transfer of APE and horizontal KE leads inevitably to strong dissipation of energy. Figure 5.4a confirms this relation. Particularly the regions, where according to Figures 5.1a and 5.1b we claimed ST should exist, show significant dissipation rates for both KE and APE. Similar to KT, the scaling arguments of ST relate the spectral energies to the dissipation rates;

$$e_{KE(n)} = C_1 \epsilon_h^{2/3} n^{-5/3}, \qquad e_{APE(n)} = C_2 \frac{\sigma_{Th}}{\epsilon_h^{1/3}} n^{-5/3}, \qquad (5.12)$$

where C_1 and C_2 are constants and σ_{Th} is the (horizontal) thermal dissipation (see section 3.2). The theory of idealized ST assumes an approximate equipartition between KE and APE (Billant and Chomaz (2001), Lindborg (2006)) and the corresponding mechanical and thermal dissipation rates. For flows with very high Re_b it was found recently that the ratio of thermal to mechanical dissipation is smaller than 1, suggesting larger KE content than APE according to the scaling laws defined in (5.12)(Maffioli and Davidson (2016), Portwood et al. (2019)). Figure 5.4a shows that ϵ_h is larger than σ_{Th} almost everywhere in the troposphere and lower stratosphere. Essentially this is the reason why KE is larger than APE at UTLS altitudes in Figure 5.4b. This suggests that SMT in the UTLS is simulated by the KMCM in accordance with the scaling laws of ST.

(a) $[\epsilon_h]$ and $[\sigma_{Th}]$ (b) KE and APE Spectra
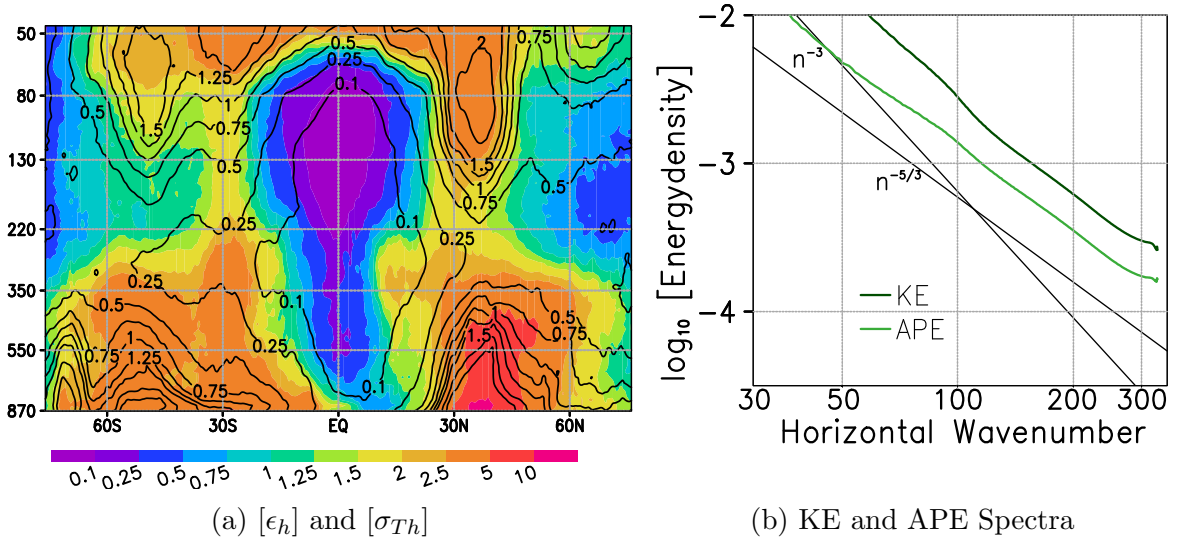
Figure 5.4: (a) Zonally and temporally averaged horizontal dissipation rates for KE and APE, i.e. ϵ_h (colors, units in 10^{-3}K/day) and σ_{Th} (contours, with levels of 0.1 0.25 0.5 0.75 1 1.25 1.5 2 10^{-3}K/day). (b) Temporally and vertically (between 220 and 60hPa) averaged spectra of KE and APE with units in m^2/s^2.

Most of the properties of ST that we have covered so far are very similar in nature to KT. The fundamental differences between ST and KT are naturally related to the effects of buoyancy in ST. In particular, the forward cascade of KE in ST is associated with conversion of KE into APE, which is subject to a forward cascade as well. A typical example of such a conversion is the vertical wind shear layers (e.g., Kelvin-Helmholtz instability), which trigger dynamical instability and the transition to turbulence. Figure 5.5a shows the spectral flux of the negative buoyancy production (i.e. $FAPE^{NBP}$ term, see equations (2.33) and (2.34) in section 2.2) contribution to the APE budget from the 16 days averaged January results of KMCM. Above ~ 350hPa, this flux is positive, meaning that the transfer of energy is from KE to APE. Also, note that this effect increases with height. Between 220 and 60hPa, i.e. the altitude range where we identified indications of pronounced SMT the values of $FAPE^{NBP}$ are comparable to the horizontal advection fluxes of APE and KE (see Figure 5.2). This result is fully in agreement with the energetics of ST events and it's observed repeatedly in many idealized ST studies (Riley et al. (1981), Brethouwer et al. (2007), Augier et al. (2015), Riley and deBruynKops (2019)).

(a) $FAPE^{NBP}$ (b) APE^{NBP}
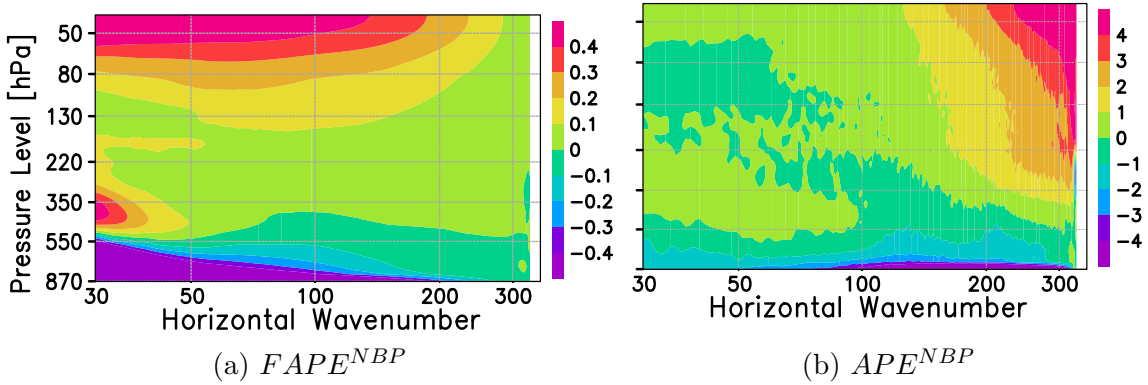
Figure 5.5: (a) Temporally averaged spectral flux of the negative buoyancy production ($FAPE^{NBP}$ in units of 10^{-5}m^2/s^3). (b) Normalized and temporally averaged APE budget contribution from the negative buoyancy production term (APE^{NBP} in units of 10^{-5}1/s). Normalization is done with the spectral APE in order to highlight the mesoscale contribution.

Furthermore, it can be seen from Figure 5.5a that the conversion term is significantly negative for the mesoscales in the lower troposphere. As we mentioned in chapter 4, mass weighted vertically integrated values of $-FAPE^{NBP}$ are significantly affected by these lower levels. Therefore, in Figure 4.6a the globally and mass weighted vertically averaged negative buoyancy production term in mesoscales are positive and have the opposite characteristic in comparison to the free atmosphere.

An important process regarding the buoyancy production term in ST is a phenomena known as restratification(Holloway (1988), Carnevale et al. (2001), Howland et al. (2020)). As explained in Avsarkisov (2020), scales that are close to the Ozmidov scale are subject to an inverse conversion process. During this process APE is converted back to KE. In physical space this means that vertically displaced layers are going back to their equilibrium position. Augier et al. (2015) interpreted the decrease of conversion flux with increasing wavenumber as restratification, which is also visible in Figure 5.5a above 150hPa and for $n > 150$. Note, however, that this behavior is likely different in nature from the re-stratification described by Avsarkisov (2020). As it can be seen from Figure 5.5b, there is no negative values for APE^{NBP} between 220 and 60hPa, meaning that conversion from APE to KE does not take place. Considering the scales that we resolve, we state that consistent with the theory of ST, there is no restratification in the KMCM.

5.1.2 Stratified Turbulence Dominated by Gravity Waves

Now we turn our attention to the role of GW dynamics on the applicability of ST theory. According to Brune and Becker (2013), GW energetics play a central role in generating the kink in the energy spectra from synoptic scales to the mesoscales. More specifically, the nonlocal vertical exchange of KE due to spontaneously generated GWs was argued to maintain the energy cascades that give rise to the spectral $-5/3$ exponential slope. The generation of these GWs is linked to the breakdown of baroclinic Rossby waves in mid-latitudes (O'Sullivan and Dunkerton (1995), Plougonven and Zhang (2014)). The resulting vertical energy transfer from GWs is also present in the current KMCM simulation that includes a scale invariant DSM scheme for horizontal diffusion (see sections 3.1 and 3.2). Figure 5.6a reflects this vertical transfer of energy in terms of the adiabatic conversion term in the KE budget. Mesoscale KE is decreased in the mid troposphere by the KE^{AC} term, and it is increased in the UTLS region. Although both APE^{NBP} and KE^{AC} represent the reversible conversion of energy in the tendency equation of the respective energy reservoir, KE^{AC} (i.e. the horizontal gradient of the geopotential in pressure coordinates) also includes the divergence of the vertical potential energy flux, which represents the major part of the vertical energy flux due to GWs and is therefore pivotal for the energetics of GWs(Koshyk and Hamilton (2001), Augier and Lindborg (2013), Becker and Vadas (2018)). Comparison of Figures

5.5b and 5.6a shows that the divergence of the vertical potential energy flux is at least as important as the internal conversion between KE and APE.
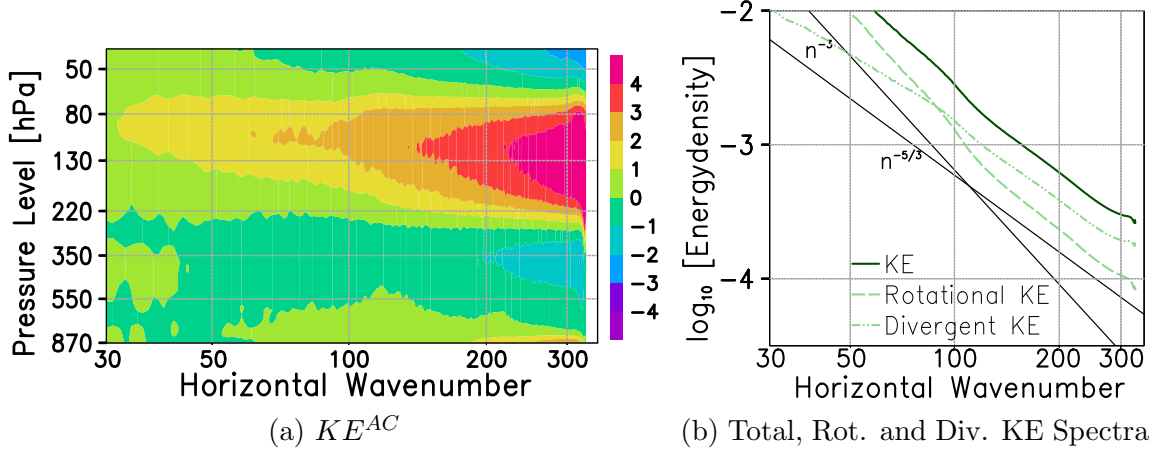

(a) KE^{AC}

(b) Total, Rot. and Div. KE Spectra

Figure 5.6: (a) Normalized and temporally averaged KE budget contribution from the adiabatic conversion term, i.e. KE^{AC}, in units in $10^{-5}1/s$. Normalization is done with the spectral KE at each respective total wavenumber. (b) Temporally and vertically (between 220 and 60hPa) averaged spectra of total, rotational and divergent KE with units in m^2/s^2.

Knowing that GW energetics play a significant role, the divergent part of the KE is expected to be prevalent at UTLS altitudes as well. Vertically averaged spectra of KE and its Helmholtz decomposition into rotational and non-rotational (divergent) parts are displayed in Figure 5.6b and support this argument. The relative dominance of divergent over rotational KE is therefore reasonable with the fact that vertical energy exchange from mesoscale GWs plays an important role at these altitudes. Note, however, that a relative dominance of the rotational modes (or at most an equipartition of rotational and divergent modes) is found in idealized simulations of ST. On the other hand, the fact that $\Delta_z > L_b$ at UTLS altitudes in the present model may result in a rather weak contribution from the rotational modes as well. Nevertheless, dominance of divergent KE over rotational KE due to a vertical KE transfer is observed in many GCM studies (Koshyk et al. (1999), Waite and Snyder (2009), Burgess et al. (2012), Žagar et al. (2017)).

It is important to note that the fact that the vertical energy exchange due to GWs being important to explain mesoscale KE and APE spectra in the UTLS does not necessarily imply that these GWs are governed by quasi-linear dynamics. It has been argued previously that the $-5/3$ spectral slope of the mesocale energy spectra in the UTLS does not require a macro-turbulent inertial range, but can be considered as a spectral superposition of inertia GWs that are subject to only weak nonlinear

interactions (Callies et al. (2014), Callies et al. (2016)). Recently Li and Lindborg (2018) argued that such an interpretation should be considered with caution regarding the degree of nonlinearity. To appropriately assess the degree of nonlinearity, they proposed to use a Rossby number, Ro, for the mesoscales that is given as;

$$Ro_\xi = \frac{|\xi_{(k_{max})}|}{f}, \tag{5.13}$$

where f is the Coriolis parameter (planetary vorticity) and $\xi_{(k_{max})}$ is the integral relative vorticity that depends on a certain maximum horizontal wavenumber k_{max}, which is calculated using longitudinal and transverse structure functions derived from aircraft measurements for the range of $[k_{min}, k_{max}]$ in mesoscales (Lindborg (2015)). Li and Lindborg (2018) showed that if this wavenumber range, $k \in [k_{min}, k_{max}]$, is large enough, then the UTLS winds satisfy the condition $Ro_\xi \sim \mathcal{O}(1)$. This is a further condition for ST in addition to $Fr_h << 1$ and $Re_b >> 1$. In particular, if Ro_ξ is of order one or larger, then nonlinear terms are much larger than the Coriolis force terms in the dynamics of the mesoscales. According to Li and Lindborg (2018), the mesoscale motions are subject to strongly nonlinear dynamics in this case. Therefore it is desirable to be able to calculate Ro_ξ in a GCM to assess the degree of nonlinearity for inertia GWs in mesoscales. However, calculation of $\xi_{(k_{max})}$ in a GCM requires an account for the unresolved part of the range of wavenumbers. We do not define a ξ_{SGS} in our study. Therefore, in order to be able to account for the SGS range in calculation of the Rossby number, we use the following alternative definition;

$$Ro_U = \frac{U_h}{f l_h}. \tag{5.14}$$

where U_h and l_h include the SGS part in a physically consistent fashion according to equations (5.8) and (5.9). A similar form of the Rossby number that depends on the velocity rather than relative vorticity was used to identify the transition from geostrophic turbulence to ST in Waite and Bartello (2006). Figure 5.7 shows the 16 days of temporally and zonally averaged Ro_U. In comparison to Figures 5.1a and 5.1b, we again see two pronounced regions in the subtropical UTLS, where Ro_U is significantly larger than 0.1 (the maximum value associated with quasi-geostrophic flow), especially in the northern winter hemisphere, where baroclinic wave activity, and hence the energy cascades toward the mesoscales, is much stronger than in the southern summer hemisphere. These local maxima of Ro_U nicely coincide with the

previously identified maxima of Fr_h and Re_b (see Figures 5.1a and 5.1b). Lindborg (2005) also identified $Ro \sim 0.1$ as the lowest Rossby number for which forward cascades associated with ST to prevail. Furthermore, Waite and Bartello (2006) argued that the vertical scale of motion transitions from quasi-geostrophic scaling. i.e. $(fl)/N$, to the ST scaling, i.e. L_b, for $Ro \sim \mathcal{O}(1)$, meaning that mesoscale motions are strongly nonlinear in accordance with the scaling laws of ST. Therefore it is perfectly safe to state that the simulated mesoscale in the KMCM are strongly nonlinear in nature.
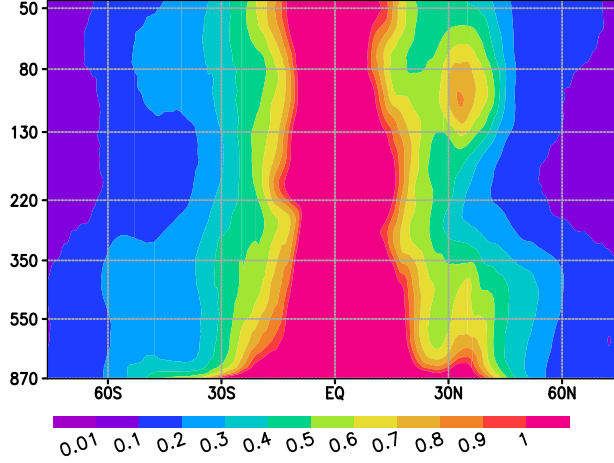
Figure 5.7: Zonally and temporally averaged dimension-less turbulent Rossby Number, according to equation (5.14).

Since mesoscale motions are mostly composed of GWs, we call this type of a cascade mechanism Stratified Macro-Turbulence, i.e. SMT. It is particularly important to realize that SMT is a direct result of the GWs that are created from the breakdown of baroclinic Rossby waves and cascade KE and APE in accordance with the scaling laws of idealized ST. In other words, the energetics of the mesoscales in the UTLS as simulated by the current version of the KMCM is akin to the energetics of ST. In the next section we provide a theoretical basis and numerical evidence as to how these spontaneously generated GWs are involved in the forward energy cascades in the mesoscales and the resulting energy spectra, even if the ST is underresolved, as discussed above.

5.2 Anelastic Gravity Wave Energetics

In order to understand how GWs can contribute to the UTLS energy cascades, we need to consider the dynamical process by which GW energy transitions into the

turbulent energy. If a buoyancy wave is spontaneously generated in the lower or mid troposphere, it may propagate to higher altitudes without necessarily being subject to GW breakdown that is accompanied by wave overturning and the spatially localized and intermittent dissipation of wave energy. GWs not subject to wave breaking are usually assumed to propagate conservatively. However, such GWs would not contribute to the energy cascades and their wave energy would not be transferred to smaller temporal and spatial scales. The absence of a spectral gap at simulated UTLS mesoscales suggests that the resolved GWs in this region are indeed not conservative within the conventional linear picture of GW dynamics, and that they cascade energy to smaller spatial (and temporal) scales. Therefore, the nonconservative GW energetics needs to be explained in the context of SMT, and the simulation of these waves with numerical truncation in the corresponding macro-turbulent inertial range requires an adequate turbulent diffusion scheme to represent the interactions with the non-resolved scales. To better understand the connection between nonlinear GWs dynamics and SMT we define the GW scale energy equations for KE and APE, i.e. KE^{GW} and APE^{GW}, in the anelastic approximation (Becker (2017)).

We firstly derive the anelastic KE^{GW} equation in height coordinates. Furthermore, we derive these expressions for mid-frequency GWs such that Coriolis term can be dropped. We start with the Eulerian form of the anelastic horizontal momentum equation that is complemented with a macro-turbulent SGS diffusion scheme;

$$(\partial_t + \vec{v}_h \cdot \vec{\nabla}_h + w\partial_z)\vec{v}_h = -\frac{1}{\rho_r}\vec{\nabla}_h p + \vec{\nabla}_h(K_h\mathbf{S}_{h0}) + \frac{1}{\rho_r}\partial_z(\rho_r K_z \partial_z \vec{v}_h), \qquad (5.15)$$

where the subscript r denotes a hydrostatic reference state that depends only on z. Next, we linearize equation (5.15) about a mean flow, multiply with a GW scale horizontal velocity, i.e. $\vec{v}_h^*$ (GW scale perturbations are represented with an asterisk, i.e. ( )*), and we average spatially and temporally over the corresponding GW scales, which is denoted by an overbar, i.e. ($\overline{}$). This leads to;

$$\overline{\vec{v}_h^* \cdot (\partial_t + \vec{U}_h \cdot \vec{\nabla}_h + W\partial_z)\vec{v}_h^*} = -\overline{\vec{v}_h^* \cdot (w^*\partial_z \vec{U}_h)} - \overline{\vec{v}_h^* \cdot \frac{\vec{\nabla}_h p^*}{\rho_r}} \\ + \overline{\vec{v}_h^* \cdot \vec{\nabla}_h(K_h\mathbf{S}_{h0}^*)} + \overline{\vec{v}_h^* \cdot \frac{1}{\rho_r}\partial_z(\rho_r K_z \partial_z \vec{v}_h^*)}. \qquad (5.16)$$

Here $\vec{U}_h$ is the mean horizontal velocity vector, and W is the mean vertical velocity. At this point, we make use of the assumption of small diffusion tendencies and argue

that the work performed by macro-turbulent friction on a GW scale control volume is negligible, thus allowing to write:

$$\overline{\vec{v}_h^* \cdot \vec{\nabla}_h(K_h \mathbf{S}_{h0}^*)} = -K_h \overline{|\mathbf{S}_{h0}^*|^2}$$
$$\frac{1}{\rho_r}\overline{\vec{v}_h^* \cdot \partial_z(\rho_r K_z \partial_z \vec{v}_h^*)} = -K_z \overline{(\partial_z \vec{v}_h^*)^2}. \quad (5.17)$$

We now apply the single-column approximation of GWs as well as the the assumption from relation (5.17), manipulate the pressure gradient term (please refer to Appendix D for details) and rewrite equation (5.16) as (see also Becker (2017), his equation 7);

$$(\partial_t + W\partial_z)\frac{\overline{\vec{v}_h^{*2}}}{2} = -(\overline{\vec{v}_h^* w^*}) \cdot \partial_z \vec{U}_h - \frac{1}{\rho_r}\partial_z(\overline{p^* w^*}) + \frac{g}{T_r}\overline{T^* w^*} - K_h\overline{|\mathbf{S}_{h0}^*|^2} - K_z\overline{(\partial_z \vec{v}_h^*)^2}. \quad (5.18)$$

Equation (5.18) describes the tendency of KE^{GW}. It is governed by vertical fluxes of GWs and a mean wind shear, a macro-turbulent diffusion in vertical & horizontal and a buoyancy production term that describes the exchange with the APE^{GW} reservoir. As a next step, we derive the anelastic APE^{GW} equation, again in height coordinates. We start with the enthalpy equation in anelastic approximation that is complemented with a macro-turbulent SGS diffusion scheme and diabatic heating;

$$c_p(\partial_t + \vec{v}_h \cdot \vec{\nabla}_h + w\partial_z)\check{T} + w d_t T_r = -gw\left(1 + \frac{\check{T}}{T_r}\right) + Q$$
$$+ c_p\vec{\nabla}_h \cdot \left(\frac{K_h}{Pr_h}\vec{\nabla}_h\check{T}\right) + \frac{c_p}{\rho_r}\partial_z\left(\rho_r\frac{T_r}{\Theta_r}\frac{K_z}{Pr_z}\partial_z\Theta\right), \quad (5.19)$$

where subscript r again denotes a hydrostatic reference state and $(\check{\ })$ denotes the deviations from that reference state. Note that we neglected the frictional heating terms from horizontal and vertical momentum diffusion, because these will lead to third-order nonlinearities in the APE budget for GWs. Our purpose here is to expand the GW energy equations only to second order in the GW perturbations. The APE in the anelastic approximation is defined as;

$$APE_{anelastic} = APE_\alpha = \frac{g^2\check{T}^2}{2N_r^2 T_r^2}, \quad (5.20)$$

where $N_r^2 = g^2/(c_p T_r)$. By multiplying equation (5.19) with $(g^2 T_r)/(c_p)$ we arrive at

the APE budget of the anelastic perturbations[3]:

$$(\partial_t + \vec{v}_h \cdot \vec{\nabla}_h + w\partial_z)APE_\alpha = - gw\left(\frac{\check{T}}{T_r} + \frac{APE_\alpha}{c_p T_r}\right) + \frac{g^2}{c_p N_r^2 T_r^2}\check{T}Q$$
$$+ \frac{g^2}{N_r^2 T_r^2}\check{T}\vec{\nabla}_h \cdot \left(\frac{K_h}{Pr_h}\vec{\nabla}_h\check{T}\right) \quad (5.21)$$
$$+ \frac{g^2}{\rho_r N_r^2 T_r^2}\check{T}\partial_z\left(\rho_r \frac{K_z}{Pr_z}\left(\frac{g}{c_p} + \partial_z\check{T}\right)\right)$$

Similar to the steps we performed between equations (5.15) and (5.16), we average both sides of equation (5.21) over the GW scales to get the APE^{GW} equation. After neglecting all triple terms we get;

$$\overline{(\partial_t + \vec{U}_h \cdot \vec{\nabla}_h + W\partial_z)APE_\alpha} = - \overline{gW\left(\frac{\check{T}}{T_r} + \frac{APE_\alpha}{c_p T_r}\right)} - \frac{g}{T_r}\overline{\check{T}^* w*}$$
$$+ \frac{g^2}{c_p N_r^2 T_r^2}\overline{\check{T}Q} + \frac{g^2}{c_p N_r^2 T_r^2}\overline{\check{T}^* Q^*}$$
$$+ \frac{g^2}{N_r^2 T_r^2}\overline{\check{T}\vec{\nabla}_h \cdot \left(\frac{K_h}{Pr_h}\vec{\nabla}_h\check{T}\right)} \quad (5.22)$$
$$+ \frac{g^2}{\rho_r N_r^2 T_r^2}\overline{\check{T}\partial_z\left(\rho_r \frac{K_z}{Pr_z}\left(\frac{g}{c_p} + \partial_z\check{T}\right)\right)}$$

Application of the single-column approximation[4] and assuming that the external diabatic heating is zero at the GW scales, we can write the GW-related APE budget as (see also Becker (2017), his equation 12);

$$(\partial_t + W\partial_z)\overline{APE_\alpha} = - \frac{g}{T_r}\overline{\check{T}^* w^*}$$
$$+ \frac{g^2}{N_r^2 T_r^2}\overline{\check{T}^*\vec{\nabla}_h \cdot \left(\frac{K_h}{Pr_h}\vec{\nabla}_h\check{T}^*\right)} \quad (5.23)$$
$$+ \frac{g^2}{\rho_r N_r^2 T_r^2}\overline{\check{T}^*\partial_z\left(\rho_r \frac{K_z}{Pr_z}\partial_z\check{T}^*\right)}$$

If we further realize that the anelastic perturbations from the reference state and the GW scale perturbations are same in amplitude by definition according to the GW theory, we can drop the ($\check{\ }$) and ( )$_\alpha$ notations. Finally, similar to relation (5.17) we

---

[3] We also neglect dT_r/dz and use following relation: $(T_r\partial_z\Theta)/\Theta_r = (T_r\partial_z(\Theta_r + \check{\Theta}))/\Theta_r = g/c_p + \partial_z\check{T}$.
[4] We also have $\partial_z T_r = 0$, which means the background is isothermal for our GW scale. Additionally, $WAPE_\alpha = 0$ for terms that appear in the right hand side, which corresponds to the condition of no vertical exchange of APE in resolved mesoscales that we show to be a valid approximation in chapter 4.

assume that there are no net fluxes from turbulent diffusion into a GW control volume defined by our averaging, we arrive at the tendency equation of the APE^{GW};

$$(\partial_t + W\partial_z)APE^{GW} = (\partial_t + W\partial_z)\frac{g^2\overline{T^{*2}}}{2T_r^2 N_r^2} = -\frac{g}{T_r}\overline{T^* w^*}$$
$$-\frac{g^2}{N_r^2 T_r^2}\frac{K_h}{Pr_h}\overline{(\vec{\nabla}_h T^*)^2} \qquad (5.24)$$
$$-\frac{g^2}{\rho_r N_r^2 T_r^2}\frac{K_z}{Pr_z}\overline{(\partial_z T^*)^2}$$

Similar to the KE^{GW} equation (except the vertical GW scale fluxes), the right-hand side of the APE^{GW} equation is composed of contributions from negative buoyancy production and from turbulent dissipation. The left-hand sides of equations (5.18) and (5.24) are equal zero when the temporal averaging is performed over many GW cycles such that a quasi-steady state is reached. These budgets for the GW KE and APE apply to the mesoscales in the UTLS because the typical vertical wavelengths of GWs that exist at these altitudes are not very large (e.g. small in comparison to those at mesospheric or thermospheric altitudes). That is, we can safely assume that compressibility effects at the GW scale are negligible in the UTLS, and therefore the anelastic approximation applies.

5.2.1 Energy Deposition in Resolved Mesoscales

Perhaps the most important detail regarding the GW energetics is that in case of no external diabatic heating at the GW scale, energy conversions are due 1) generation of GW kinetic energy due to the energy deposition term, 2) conversion of GW kinetic energy into GW potential energy via negative buoyancy production, and 3) dissipation of GW kinetic and potential energy. In the model, the latter is described via the parameterization of macro-turbulent diffusion. It is straightforward to show that the assumption of negligible GW generation by external diabatic heating is correct in our current model setting. To show this we evaluate all right-hand side terms from the spectral APE budget. In Figure 5.8 we show the temporally averaged (16 days) spectral contributions to the spectral APE budget plotted from 550 to 40hPa altitude for all terms from equation (2.33), except the APE^{VE} term (since this term is negligible for our APE budget in free atmosphere as we showed in chapter 4). As it can be seen, the spectral contribution from the Q_c, Q_m and Q_{rad} terms are effectively zero in comparison

to all other contributing terms, therefore proving that our assumption of no generation of GWs due to external diabatic heating to be valid.
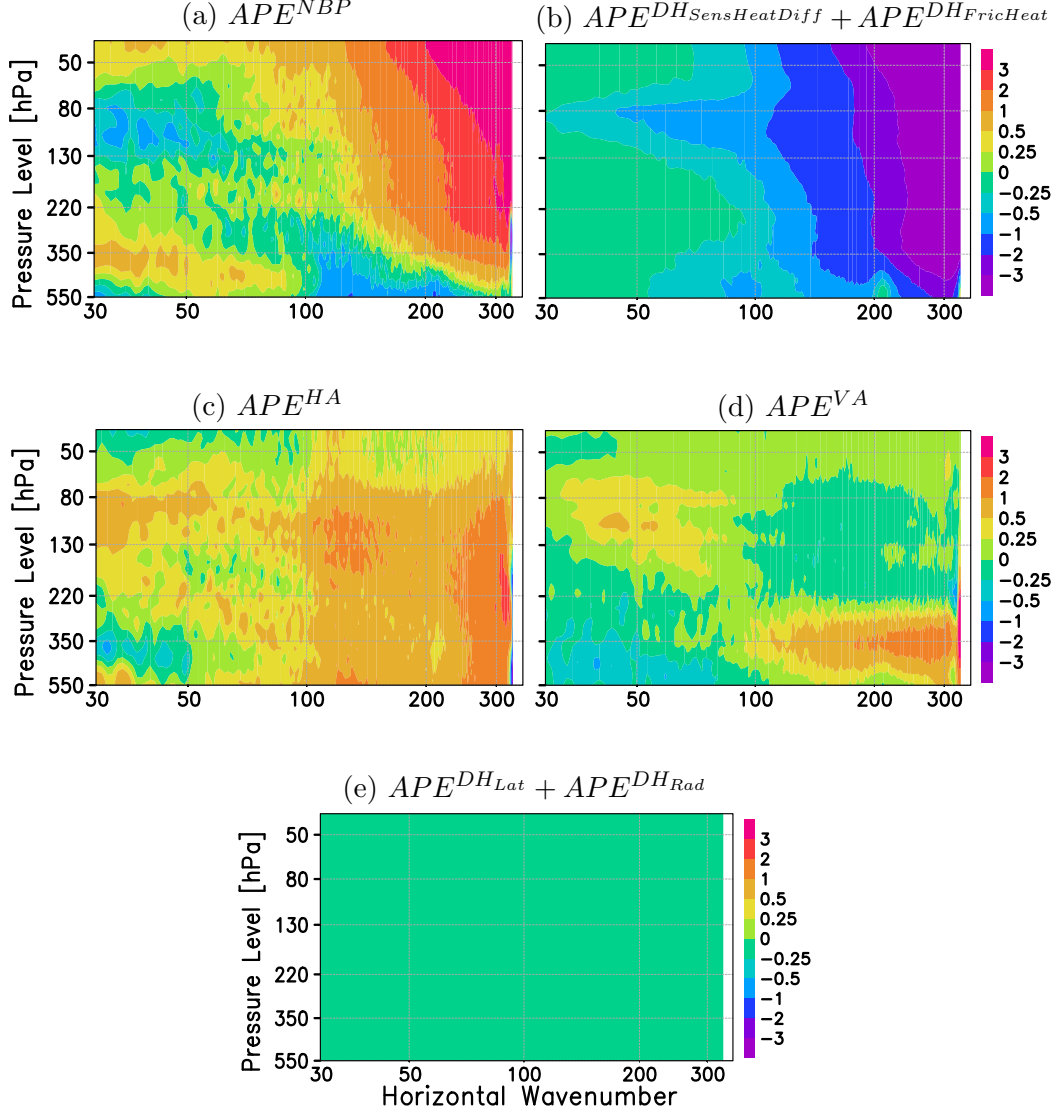

Figure 5.8: 16 days of temporally averaged and normalized contributions to the spectral APE budget as defined in equation (2.33) in units of $10^{-5} 1/s$. (a) Negative buoyancy contribution, i.e. the APE^{NPB} term. (b) Diabatic heating contribution from the sum of total turbulent diffusion of sensible heat and the total frictional heating, i.e. the $APE^{DH_{SensHeatDiff}} + APE^{DH_{FricHeat}}$ term. (c) Horizontal advection contribution, i.e. the APE^{HA} term. (d) Vertical advection contribution, i.e. the APE^{VA} term. (e) External diabatic heating contribution from the sum of the prescribed cumulus heating term Q_c in the tropics, the self-induced condensational heating term Q_m in midlatitudes and the temperature relaxation term Q_{rad} as a surrogate for radiative heating. Note that all figures have the same color increments and that the color bars use nonlinear scaling to highlight small deviations from zero.

Since there's no forcing of GWs by external diabatic heating in our model in the free

atmosphere, and as long the mesoscale spectral energies in the UTLS are not simply a reflection of upward propagating GWs generated in the lower troposphere, the most likely explanation of the simulated KE and APE spectra in our mesoscales is that they reflect maco-turbulent cascades of KE^{GW} and APE^{GW}. Evidently, the explicit simulation of these macro-turbulent cascades in a numerical model that is truncated within the corresponding inertial range will depend crucially on the way that non-resolved scales are represented by some SGS diffusion scheme. Nevertheless, energy deposition of GWs propagating from below into the UTLS may play a significant role in the mesoscale energetics of the UTLS. Usually, energy deposition of GWs (Hines and Reddy (1967)) is considered a purely dissipative process in the single-column, steady-state picture (Becker (2017)). However, when considering theory of GW saturation (Lindzen (1981)) in this picture, it is clear that GW saturation and the resulting GW breakdown initiates a cascade to smaller-scale GWs and eventually to KT (e.g., Fritts and Werne (2000), Vadas and Fritts (2002)). That is, GW saturation can only be associated directly with GW dissipation in the net within the framework of GW parameterization schemes (e.g., Becker (2004), Becker and McLandress (2009)). In the following, we will analyze how GW saturation and GW energy deposition are involved in the resolved mesoscale energetics of the UTLS.

The energy deposition consists of a vertical pressure flux convergence and a vertical shear production term, which correspond to the second and first term, respectively, on the right-hand side of equation (5.18). In fact, in accordance with Becker (2017), we may express the energy deposition term, i.e. E, from the mean KE^{GW} equation as;

$$E = -\frac{1}{\rho_r}\partial_z\overline{p^*w^*} - (\overline{\vec{v}^*w^*})\cdot\partial_z\vec{U}_h = -\frac{g}{T_r}\overline{T^*w^*} + K_h\overline{|\mathbf{S}_{h0}^*|^2} + K_z\overline{(\partial_z\vec{v}_h^*)^2}. \qquad (5.25)$$

Equation (5.25) directly shows that in the case of nonconservative wave propagation, energy deposition of mean KE^{GW} can also be expressed by the negative buoyancy production, i.e. $-gT_r^{-1}\overline{T^*w^*}$, plus the turbulent dissipation of GW KE. Furthermore, according to the steady state version of equation (5.24), the negative buoyancy production has to be positive definite. In steady state, the transfer of KE^{GW} to APE^{GW} balances the turbulent dissipation of GW APE. If we further assume that the GWs are subject to strongly nonlinear dynamics governed by the scaling laws of ST, then, both the mechanical and thermal dissipation rates have similar magnitudes. Hence, *the negative buoyancy production term should be about half the energy deposition term.* This

hypothesis can be easily tested using our spectral KE and APE budget formulation via the corresponding spectral contributions in the mesoscales.

As is shown in Appendix D, the sum of the vertical pressure flux convergence, i.e. $-\rho_r^{-1}\partial_z\overline{p^*w^*}$, and the buoyancy production term, i.e. $gT_r^{-1}\overline{T^*w^*}$, corresponds to the adiabatic generation of KE. In our spectral budget analyses, where this term is represented by the FKE^{AC} term. The shear production term, i.e. $-(\overline{v^*w^*})\partial_z\vec{U}_h$, is part of the vertical advection of horizontal momentum, which in our spectral budget analyses is represented by the FKE^{VA} term. By summing up FKE^{AC} and FKE^{VA} and adding the negative buoyancy production term from the spectral APE budget, i.e. $FAPE^{NBP}$, we can calculate the energy deposition term from our model in wavenumber space. In Figure 5.9 we show the 16-day average of the ratio of the energy deposition to the negative buoyancy production, i.e. $E/(-gT_r^{-1}\overline{T^*w^*})$, in wavenumber space. For $n > 120$ and altitudes between ~ 180 and ~ 80hPa, the model result roughly agrees with the relation $E \approx 2(-gT_r^{-1}\overline{T^*w^*})$. Thus according to our reasoning, the resolved GWs at UTLS altitudes should be characterized by an ST-type macro-turbulence cascade that is characterized by similar amounts of total KE and APE dissipation rates.
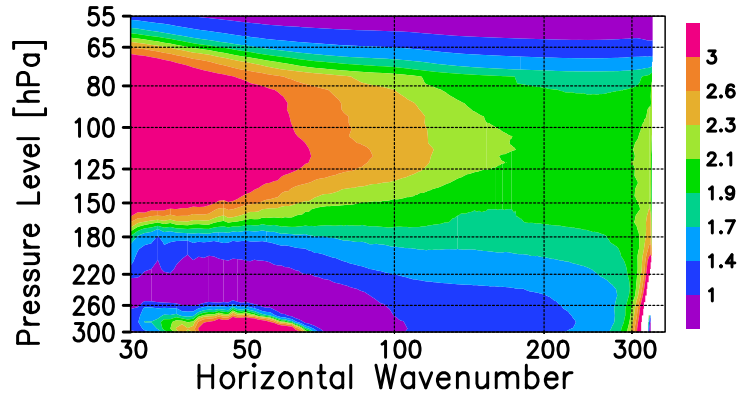

Figure 5.9: 16-day average of the ratio of spectral fluxes due to energy depositon, i.e. $E = FKE^{AC} + FKE^{VA} + FAPE^{NBP}$, and the negative buoyancy production term, i.e. $-gT_r^{-1}\overline{T^*w^*}(FAPE^{NPB})$.

The concept of Lindzen (1981) describes the transition of the GW energy into KT and its subsequent dissipation as a result of convective instability of a monochromatic GW. Application of this concept in quasi-linear GW theory is expressed in terms of turbulent vertical diffusion coefficient. This diffusion coefficient damps the GW such as to keep the temperature profile that is due to the wave plus the background at marginal convective instability. In Lindzen's theory, the turbulent Prandtl number is equal 1. Later on, it was shown that the Lindzen scheme can also be formulated

with larger turbulent Prandtl numbers (e.g. Liu (2000)), as was recommended by the considerations of Fritts and Dunkerton (1985). The concept of GW saturation was also used to explain the universal behavior of the vertical wavenumber spectra of GWs which are usually characterized by an exponential -3 slope. Such a slope is also compatible with the assumption that the observed GW spectra result from a macro-turbulent inertial range that is subject to the scaling laws of ST (Billant and Chomaz (2001), Lindborg (2006), Maffioli (2017)). In this thesis, we shall hypothesize that when SMT involves energy deposition from mid-frequency GWs, the GW modes in the SMT regime appear to be, on average, at the saturation level. For the regime of interest here, namely the subtropical UTLS, we can provide some indication that GW saturation plays a role in the mesoscales when considering, for example, the turbulent vertical diffusion coefficient in the KMCM, K_z. For the extended model version described in Becker and Vadas (2020) (their Appendix A), the K_z is scaled by the usual Richardson number criterion, that is, K_z becomes large when the static stability decreases and vertical wind increases. This is typically the case when vertically propagating GWs are refracted towards smaller vertical wavelengths. For the subtropical UTLS region, we see from Figure 5.10a that there is westward mean wind shear above the subtropical jets. Hence, westward propagating GWs in this regime should be subject to increasing dynamic instability with increasing height, resulting in some damping by K_z (and by our horizontal diffusion scheme as well). Note that eastward propagating GWs generated in the mid and lower troposphere are presumably filtered by the subtropical jet such that mainly westward propagation directions are expected for the GWs in the subtropical UTLS. These waves encounter increasing instability with height due to the westward wind shear. Hence, we expect the maximum K_z above the jet levels. This is confirmed by the black contours in 5.10a.

Figure 5.10b show the energy spectra for $n > 30$ that result from averaging the resolved energy spectra vertically from 180 to 80hPa. The fact that the divergent KE is roughly equal to the APE and much larger than the rotational KE for $n > 100$ indicates that the GW modes in this regime ($n > 100$) are mid-frequency GWs, as is assumed also in Lindzen's saturation theory. Together, Figures 5.10a and 5.10b lend further confidence to our hypothesis that the SMT regime in the UTLS can presumably be described also by GW modes with amplitudes at their saturation levels. For the resolved SMT in the KMCM, the saturation levels are maintained mainly by strong nonlinear interactions (energy cascades) rather than by damping via different diffu-

sion coefficients for individual monochromatic GWs that do not interact at all. Note, however, that precisely this picture of superposition of linear GW modes subject to saturation has long been assumed to hold as an explanation for the universal behavior of the vertical wavenumber GW spectra (see Smith et al. (1987); Fritts and Alexander (2003)).
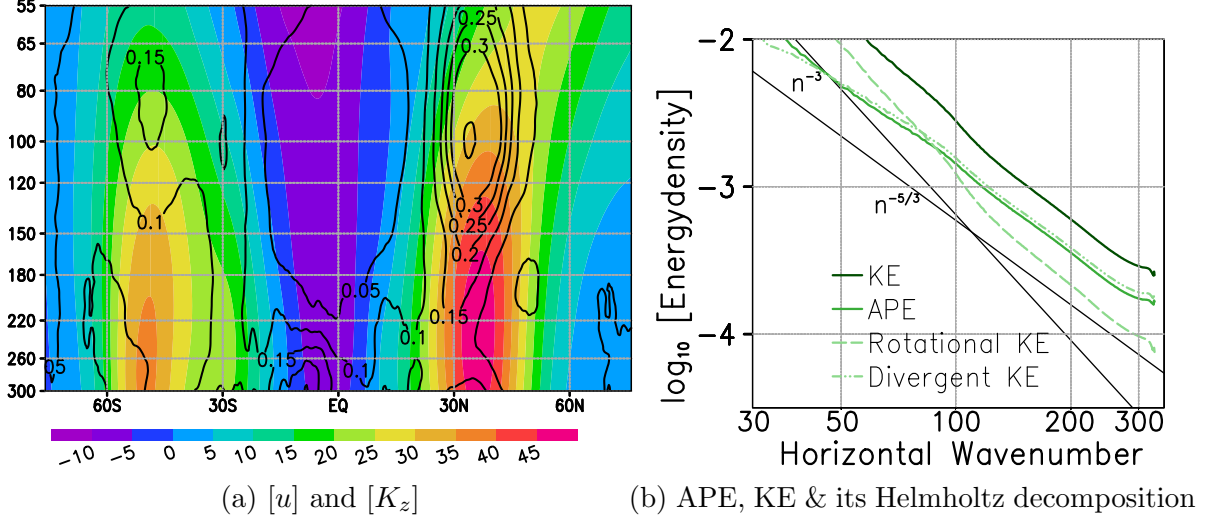

(a) $[u]$ and $[K_z]$ (b) APE, KE & its Helmholtz decomposition

Figure 5.10: (a) Zonally and temporally averaged zonal wind, i.e. $[u]$ (colors) in units of m/s, and dynamic vertical momentum diffusion coefficient, i.e. $[K_z]$ (contours, with levels of 0.05 0.1 0.15 0.2 0.25 0.3 0.4 m^2/s). (b) Similar to Figure 5.6b, temporally and vertically (between 180 and 80hPa) averaged spectra of APE and total, rotational and divergent KE in units of m^2/s^2.

5.2.2   Mesoscale Cascades Maintained by Westward Gravity Waves

In order to further support our hypothesis of SMT in the subtropical UTLS in combination with saturating GWs, we now inspect a typical snapshot of the GW phases along with the instantaneous background wind in longitude-height plots (Figure 5.11). In Figure 5.11a we show the GW field for the whole of resolved mesoscale range, i.e. for $50 < n < 330$. The westward oriented GW packet that resides between 15E and 30E and around 150hPa altitude has a phase that clearly extends from 50hPa to lower altitudes ($\sim$ 300hPa). Additionally, we also see a GW packet centered at about 30E and 550hPa altitude, which has phases that extend to about 260hPa from below. This GW packet presumably also propagates westward, but downward. Minor

indications of eastward propagating GWs with upward (downward) group propagation above (below) an altitude of about $300 - 250$hPa can be inferred east of 40E. Such shapes for GW phases resemble partly the X-shaped structure of the GWs that are generated by spontaneous emissions due to strong horizontal and vertical wind shears in the UTLS (Plougonven and Zhang (2014), Becker et al. (2022), Vadas et al. (2022)). In this picture, generated GWs propagate upward and downward into different horizontal directions away from the source region. These GWs have scaled amplitudes that are largest towards lower altitudes, which is the case for the westward GW packet around 15E and 30E that has upward group propagation. Furthermore, from Figures 5.11e and 5.11f we see that this GW source is in the exit region of a strong eastward zonal jet, which is typical for GW generation by spontaneous emission in the UTLS (Zhang (2004)). This finding further confirms our hypothesis that westward GWs generated by spontaneous emission in the UTLS would be subject to saturation as they propagate upward into the lower stratosphere due to westward vertical wind shear.

In Figure 5.11 we also show GW fields for various intermediate total horizontal wavenumber ranges. The aforementioned westward GW packets above and to the west of the jet exit region and the eastward GW packets farther to the east can be easily seen in Figures 5.11b, 5.11c and 5.11d. However these smaller scale GW packets are isolated patches that no longer resemble an X-structure as is expected from spontaneously generated GWs, nor do they have phases that extend to lower altitudes, where the source region is. This picture of isolated GW packets for higher wavenumber intervals in mesoscales contrasts the GWs that are visible when all wavenumber $n > 50$ are taken into account (Figure 5.11a). This is particularly evident to the east of the aforementioned GW source, where the small-scale GWs appear to undergo dissipating, while those GWs propagating to west are first refracted to larger vertical wavelengths before they dissipate above the source level due to westward wind share as mentioned above. Therefore, Figures 5.11b, 5.11c and 5.11d may be considered as an illustration of how SMT looks like in physical space in terms of the GW field in an instant of time for different spectral regimes in the UTLS. Indeed, if we consider the picture of strongly nonlinear dynamics in a macro-turbulent inertial range consisting of GW modes, it is well conceivable that patches of GWs appear in certain spectral windows with indications of the usual mechanisms associated with GW generation, instability and dissipation via diffusion in the model. In other words, the forward spectral flux in horizontal wavenumber space should lead to instances where certain spectral elements

are populated and depopulated due to nonlinear interactions (advection terms) and macro-turbulent diffusion in certain regions.
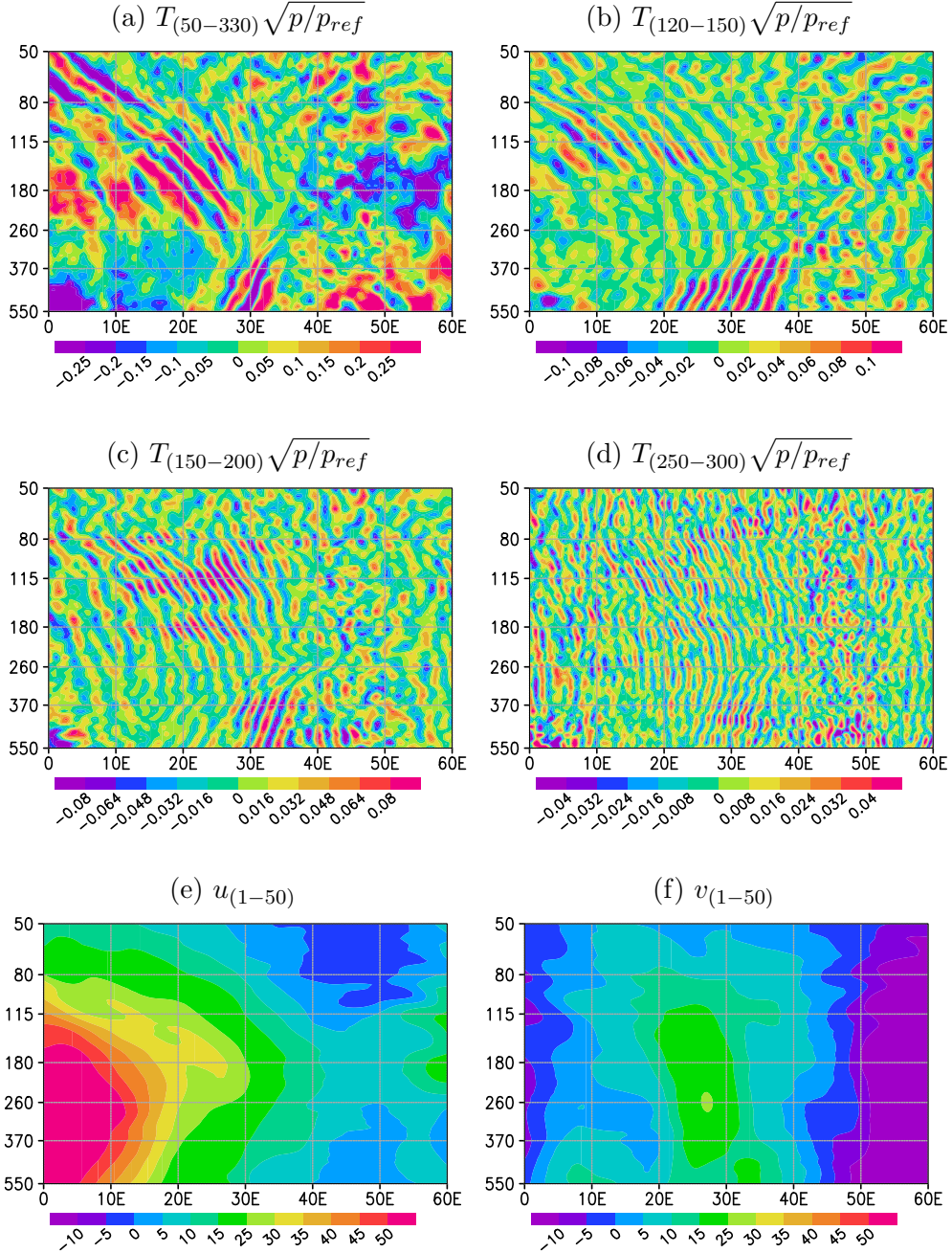

Figure 5.11: (a)-(d) Instantaneous longitude-height snapshots of temperature perturbation (in units of K) calculated based on a certain total horizontal wavenumber range (this range is given in the panel labels above each figure) and scaled with $\sqrt{p/p_{ref}}$ (for $p_{ref} = 1013$hPa) at each pressure level to highlight the mid tropospheric wave amplitudes. (e) & (f) Instantaneous longitude-height snapshots of the large scale (for the wavenumber range of $1 < n < 50$), zonal wind, i.e. $u_{(1-50)}$, and the meridional wind, i.e. $v_{(1-50)}$, with units in m/s. All snapshots are taken at 30N latitude and on the 5th day, 2nd hour & 5th minute of the 16 days of simulation time.

In order to provide further insight to this behavior of the highly nonlinear saturation mechanism, we rewrite the equations (5.18) and (5.24) in steady state form using the energy deposition definition from equation (5.25):

$$E + \frac{g}{T_r}\overline{T^* w^*} = K_h \overline{|\mathbf{S}_{h0}^*|^2} + K_z \overline{(\partial_z \vec{v}_h^*)^2} \tag{5.26}$$

$$-\frac{g}{T_r}\overline{T^* w^*} = \frac{g^2}{N_r^2 T_r^2} \frac{K_h}{Pr_h} \overline{(\vec{\nabla}_h T^*)^2} + \frac{g^2}{\rho_r N_r^2 T_r^2} \frac{K_z}{Pr_z} \overline{(\partial_z T^*)^2}. \tag{5.27}$$

Equation (5.26) and (5.27) highlight the fact that in the steady-state single-column picture, there is a balance between the energy deposition plus the buoyancy production and the total mechanical dissipation, as well as a balance between the negative buoyancy production and the total thermal dissipation. In the idealized picture of Lindzen's saturation mechanism, each individual GW mode is damped by a specific diffusion coefficient. In the resolved picture of strongly nonlinear mesoscale dynamics, however, the nonlinear interactions keep each individual GW mode on average at its saturation level. During the energy cascades from large to small scales, GW modes appear and disappear in certain regions and at certain times, thus resulting in isolated patches of GWs as plotted in Figures 5.11b, 5.11c and 5.11d.

This picture is further substantiated in Figures 5.12a, 5.12c and 5.12e. In these 3 figures we show the resolved balance between the spectral horizontal advection fluxes of KE (FKE^{HA}) and APE ($FAPE^{HA}$) as well as the steady state saturation balance for KE^{GW} ($E - FAPE^{HA} + FKE^{TotDiff}$) and for APE^{GW} ($FAPE^{NBP} + FAPE^{TotDiff}$) as described in equations (5.26) and (5.27). If the idealized saturation mechanism described by Lindzen was the explanation for the universal behavior of mesoscales, the cyan and brown curves in Figures 5.12a, 5.12c and 5.12e would be equal 0. Instead of this idealized picture, we see that these curves have significant negative values (meaning that more mesoscale energy is dissipated than is added via energy deposition), and that these negative values are almost exactly balanced by the spectral horizontal advection fluxes of KE and APE due to resolved forward macro turbulent cascades. This holds not only for the lower stratosphere, but also for $180 < p < 350$hPa (remaining lower altitudes are not shown in Figure 5.12). Since the absolute spectral diffusion tendencies (not the fluxes) are most relevant at the largest n, i.e. close to the truncation scale, the energy deposition feeds part of the macro-turbulence from 350 to 80hPa. Hence, energy deposition from upward propagating GWs plays a crucial role in maintaining the macro-turbulent forward cascades of mesoscale KE and APE.
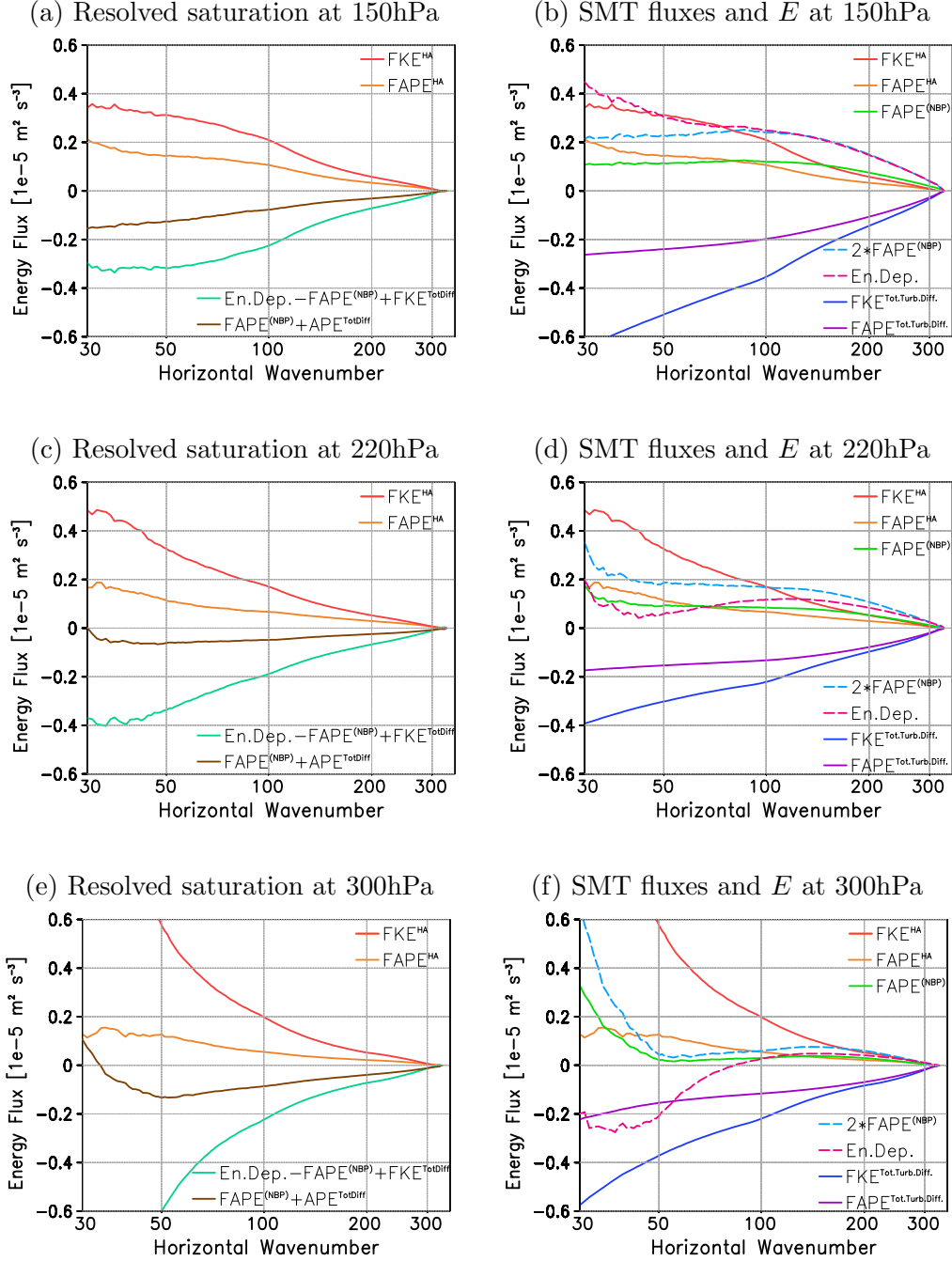
Figure 5.12: 16-day average of the spectral fluxes in units of $10^{-5}\text{m}^2/\text{s}^3$ at three different altitudes, i.e. at 150hPa, 220hPa and 300hPa. Panels in (a), (c) and (d) show the idealized picture of saturation mechanism as described in equations (5.26) and (5.27) for resolved spectral modes together with the spectral fluxes due to horizontal nonlinear advection of KE and APE. Panels (b), (d) and (e) show the relevant SMT fluxes and the energy deposition term, i.e. E from equation (5.25). Terms and their respective colors for the curves are given as follows: $FKE^{HA}(\text{—})$, $FAPE^{HA}(\text{—})$, $FAPE^{NBP}(\text{—})$, $FKE^{TotDiff}(\text{—})$, $FAPE^{TotDiff}(\text{—})$, $E(\text{—})$, $(2*FAPE^{NBP})(\text{—})$, $(E-FAPE^{NBP}+FKE^{TotDiff})(\text{—})$, $(FAPE^{NBP}+FAPE^{TotDiff})(\text{—})$.

As it can be seen from Figures 5.12b, 5.12d and 5.12f, the relative importance of E increases from the upper troposphere to the lower stratosphere. Especially in Figure, 5.12b, the previously mentioned relation of $E \approx 2(-gT_r^{-1}\overline{T^*w^*})$ holds almost perfectly, as indicated by overlapping magenta and light blue dashed curves at 150hPa altitude. This suggests that the macro-turbulence in the lower stratosphere is strongly maintained E due to GWs from below, rather than by energy injection due to baroclinic waves, which applies at about 350 to 180hPa. Therefore, the GW dynamics in the lowermost stratosphere is consistent with the constraint $E \approx 2(-gT_r^{-1}\overline{T^*w^*})$ that follows from the horizontally averaged picture (single-column approximation) combined with the assumption of similar dissipation rates for KE and APE. As Brune and Becker (2013) showed, the formation of the forward spectral fluxes in the mesoscales due to horizontal advection of KE and APE are also largely maintained by the strong energy injection due to breaking of baroclinic waves. This can be seen from the strong contributions from horizontal advection of KE at smaller wavenumbers in Figure 5.12f. Thus for these altitudes, we do not expect the constraint $E \approx 2(-gT_r^{-1}\overline{T^*w^*})$ to hold.

The foregoing results suggest that the saturation mechanism in the real atmosphere that gives rise to the universal behavior of the vertical wavenumber spectra of GWs is governed by the scaling laws of SMT. The schematic in Figure 5.13 illustrates the general underlying mechanism by considering the spectral fluxes at spectral element at an arbitrary wavenumber n_{meso} that lies within the macro-turbulent inertial range. The energy deposition of the GWs from below feeds part of the macroturbulent cascades and in return, the forward cascades of APE and KE at each spectral element keep the GWs at the saturation level. As KE and APE cascade to smaller and smaller scales, the horizontal wavenumber spectra assume a $-5/3$ exponential spectral slope, while the vertical wavenumber spectra should follow a -3 law, as is predicted by the scaling laws of SMT and is observed for GWs in the real atmosphere.

The applicability of the concept of SMT that is maintained by energy deposition is supported by comparable magnitudes for forward spectral fluxes of KE and APE, as well as by the negative buoyancy production in Figure 5.12b. Additionally, a permanent conversion of KE into APE by negative buoyancy production term appears to be a general feature of SMT, whether the forward cascades are maintained by energy deposition (lowermost stratosphere, Figure 5.12b) or baroclinic waves (upper troposphere, Figures 5.12d and 5.12f). This is suggested by our simulation results for these different altitude regimes because $FAPE^{NBP}$ (solid green curves in the right column of

Figure 5.12) is always positive (conversion of KE into APE) in the mesoscales. Further support for the applicability of SMT to both the upper troposphere and regimes at higher altitudes, where the forward cascades are maintained by energy deposition, is provided by the fact that the simulated dissipation rate of KE and APE have similar magnitudes at the smallest resolved scales.
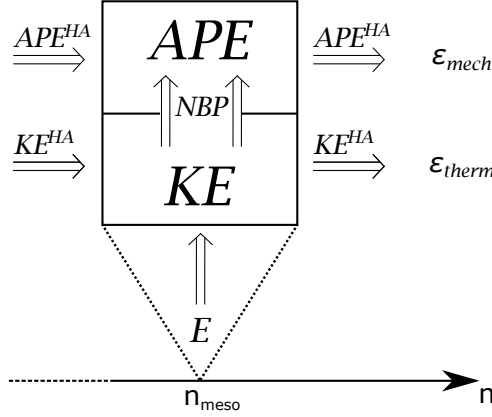

Figure 5.13: Schematic picture of mesoscale energetics of resolved Lindzen type saturation that is subject to SMT-type forward cascades.

5.2.3 Significance of Scale Invariance for Energy Deposition

In comparison to ST theory, the idealized system of saturated linear waves can neither explain a cascade mechanism nor can it predict the shallowing of the mesoscale horizontal wavenumber spectra with an approximate $-5/3$ exponential slope that is found for the mesoscale GWs in the UTLS of the KMCM (e.g., Figure 5.10b). Given the macro-turbulent nature of the mesoscale GW spectra, it is tempting to conclude that simply resolving several decades of horizontal wavenumbers in a circulation model (and applying a correspondingly high vertical resolution as well) should be sufficient to simulate the nonlinear interactions that give rise to the forward energy cascades and the resulting KE and APE horizontal wavenumber spectra. Such a conclusion does, however, not apply. In subsections 3.1 and 3.2.2, particularly via the results shown in Figures 3.1 and 3.2 we argue that numerical (spatial) resolution is only a necessary condition to simulate the mesoscale energetics and spectral behavior within the the resolved scales, and that in addition, the mathematical constraints imposed by the scale invariance that holds in the resolved macro-turbulent inertial range must be fulfilled by the SGS diffusion scheme. The consequences of not fulfilling the scale invariance

criterion (SIC) can be further highlighted by numerical sensitivity experiments by employing turbulent diffusion schemes that do not fulfill the SIC. Let us recall that the derivation of the relation $E \approx 2(-gT_r^{-1}\overline{T^*w^*})$ requires the assumption of about similar dissipation rates of KE and APE, which is a direct consequence of assuming ST-type cascades that should be reflected by the dissipation rates simulated via the SGS parameterization. In subsection 3.2.2 we highlighted the importance of the SIC in the SGS scheme to simulate ST-type cascades that give rise to $-5/3$ exponential spectral slopes in the KE and APE spectra. Based on these results it should be expected that the relation of $E \approx 2(-gT_r^{-1}\overline{T^*w^*})$ would not hold in the resolved mesoscales when applying a horizontal diffusion scheme that does not comply with the SIC.

In Figure 5.14 we show the 16-day average of the relation that tests the validity of $E \approx 2(-gT_r^{-1}\overline{T^*w^*})$ in wavenumber space (please refer to Figure 5.9 and the exact definition given in the context of this figure for the quantity shown in Figure 5.14). These results are from 4 different KMCM runs, for which the horizontal diffusion scheme is not consistent with the SIC. In Figure 5.14a, we apply the classical Smagorinsky model (Becker and Burkhardt (2007)) with a constant mixing length of $l_h^2 = 11.4\text{km}^2$ that is used for horizontal diffusion of both horizontal momentum and sensible heat. We label this run as SMAG_11.4. In the other panels of Figure 5.14 we utilized the generalized Dynamic Smagorinsky Model (gDSM, Schaefer-Rolffs (2017)) that self-consistently calculates the l_h^2 term via a dynamic Smagorinsky parameter, but uses a fixed horizontal Prandtl number, thereby violating the SIC regarding the forward cascade of APE. These runs are accordingly labeled as gDSM_Mom. These 3 different gDSM_Mom runs deviate by the value chosen for the constant horizontal Prandtl number. The results shown in Figures 5.14b, 5.14c and 5.14c are obtained from gDSM_Mom simulations with values of 2, 1 and 0.7, respectively, for Pr_h. Comparing Figure 5.14 with Figure 5.9, it is clear that none of the experiments that do not take the SIC fully into account captures the relation of $E \approx 2(-gT_r^{-1}\overline{T^*w^*})$ that we derived from the GW energetics in combination with the assumption of SMT (similar dissipation rates for KE and APE). All four sensitivity runs in Figure 5.14 overestimate the energy deposition term over the negative buoyancy production term for $n > 100$ and $80 < p < 220\text{hPa}$. These results confirm our argument about the necessity of complying with the SIC in the turbulent diffusion of both horizontal momentum and sensible heat.
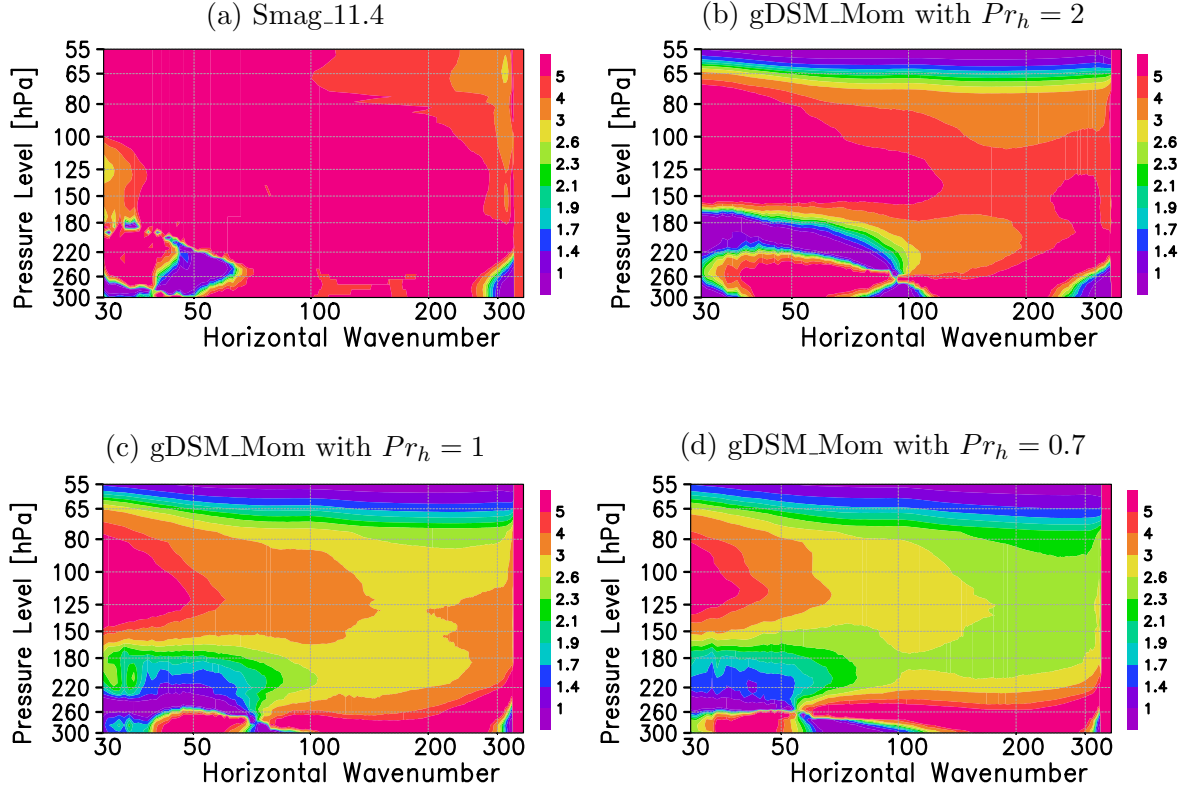
Figure 5.14: 16-day average of the ratio of spectral fluxes due to energy depositon, i.e. $E = FKE^{AC} + FKE^{VA} + FAPE^{NBP}$, and the negative buoyancy production term, i.e. $-gT_r^{-1}\overline{T^*w^*}(FAPE^{NPB})$, calculated for 4 different KMCM runs. See text for definitions of these runs. Note that color bars use a larger range of values in comparison to Figure 5.9.

Comparison of Figures 5.14b, 5.14c, 5.14d with Figure 5.9 emphasizes the importance of complying with the SIC not only of the horizontal diffusion of momentum, but also for the horizontal diffusion of sensible heat. This comparison also shows that a constant horizontal Prandtl numbers of 1 or 0.7 are clearly a better choice than assuming a value of 2, as was done in the previous studies based on the KMCM (e.g.,Schaefer-Rolffs and Becker (2018)). It is also interesting to note that, although $Pr_h = 1$ complies both with the presumed value from the idealized theory of superposed saturated GWs as well as the dynamically calculated Pr_h resulting from the resolved nonlinear westward GWs from our KMCM runs, the gDSM_Mom simulation that has $Pr_h = 0.7$ seems to be the one that comes closest to simulate the relation of $E \approx 2(-gT_r^{-1}\overline{T^*w^*})$ at UTLS altitudes. This result is not very surprising since we found values around 0.68 at UTLS altitudes for the horizontally averaged dynamic Pr_h (see Figure 3.4b in subsection 3.2.2).

Chapter 6

Summary and Outlook

In this study, we used a mechanistic GCM with a fully scale-invariant horizontal diffusion scheme for 16 model days with permanent January conditions. The first part of our study is about extending the constraint of SIC to the horizontal sensible heat diffusion. This extension is based on the gDSM concept (Schaefer-Rolffs (2017)). We formulated this scheme such that the horizontal Prandtl number becomes a space and time dependent parameter. A clear improvement of a smoother $n^{-5/3}$ power law for $n > 120$ for the simulated KE and APE spectra from our newly developed model version in comparison to the spectra from runs that uses a constant horizontal Prandtl number is found. In accordance with this result, the spatial distribution of the horizontal thermal dissipation rate was also simulated differently and it was found to be pronounced in regions of wave breaking or more generally in regions with strongly nonlinear processes. These results further support the underlying hypothesis of this thesis that the mesoscale dynamics are on average governed by the scaling laws of SMT.

This hypothesis forms the basis of the second part of this study, in which we investigated the validity of the theory of SMT with regard to the simulated mesoscales using the KMCM version that includes the new fully scale-invairant horizontal diffusion scheme. Estimation of the characteristic statistical metrics of idealized ST indicated that the necessary conditions for the existence of strongly nonlinear ST-type cascades are fulfilled in our 16 days of January simulations. These indications were found to be pronounced in a specific region in our model, i.e. at sub-tropical (~ 30 degree latitudes) UTLS altitudes (for $220 < p < 60$hPa) in both hemispheres, with stronger values in the northern winter hemisphere. Spectral budget analyses of KE and APE showed that the simulated dynamics at UTLS altitudes is in full agreement with the spectral characteristic of idealized ST. On the other hand, the same model results suggest that the mesoscales in the lowermost stratosphere consist of GW modes that propagate into this region from below. In order to further shed a light on this apparent contradiction, we extended our theoretical interpretation of simulated mesoscales to also include the

theory of saturated nonconservative GWs for the mesoscales.

Accordingly, we recapitulated the energetics of mid-frequency GWs when assuming the steady-state and single-column approximations. This showed that for dissipating GWs, 1) part of the generation of KE that is due to energy deposition (caused by GWs propagating from below) is converted into APE and 2) the energy deposition is about two times this negative buoyancy production rate if the dissipation rates of KE and APE are similar. When applying this picture in horizontal wavenumber space and assuming that the GWs are part of a macro-turbulent inertial range, then the spectral fluxes due to the dissipation rates, the energy deposition, and the buoyancy production must be completed by the forward spectral fluxes from the horizontal advection terms. We showed that in our high-resolution GCM, the energy deposition in the UTLS is only then about twice the conversion rate from KE into APE when complying with the SIC for the horizontal diffusion of both horizontal momentum and sensible heat. This is consistent with the fact that according to equation (5.24), the thermal dissipation from the diffusion scheme should strongly affect the behavior of the negative buoyancy production term. When the thermal dissipation term is captured correctly, the non-conservative propagation of GWs gives rise to ST type energy cascades, where the GW modes involved in these cascades are at the saturation level. Accordingly, we specified which type of GWs in the resolved modes can be subject to saturation and showed explicitly their existence in physical space above the subtropical jet stream. Finally, we note that the significance of utilizing the Dynamic Smagorinsky Model to simulate nonconservative GW dynamics has been demonstrated in several studies, for example for cloud-topped boundary layer flows (Kirkpatrick et al. (2006)), for mountain waves reaching MLT altitudes (Lund et al. (2020)), or for idealized LES of GW breaking (Remmler et al. (2015)). Therefore, when the SIC is fulfilled by the SGS diffusion scheme, we can summarize the mechanism giving rise to in the mesoscales at UTLS altitudes as follows:

1. The mesoscale branches of the KE and APE spectra above the maximum of the upper tropospheric jet are primarily governed by resolved westward mid-frequency GWs at subtropical and middle latitudes, for which each GW spectral element is on average at the saturation level.

2. This saturation of these GWs indicates that energy is being deposited due to propagation from below.

3. The strongly nonlinear dynamics of the saturated GWs are characterized by forward cascades of both APE and KE that are governed by the scaling laws of ST. Accordingly, half of the energy that is deposited as KE is converted into APE.

Aside from the main results and discussions, we also examined the validity of our spectral APE budget analyses as well as the energetics of the new model version with fully scale-invariant horizontal diffusion with respect to the global-scale dynamics and the Lorenz Energy Cycle. Particularly, we compared our results with the analyses of Lambert (1984), who also performed total spectral KE and APE budget analyses based on globally assimilated model results. Discrepancies between our spectral APE budget analysis and that of Lambert (1984) are limited to the lower troposphere and results from the fact that our spectral analysis is performed in the model's terrain-following vertical hybrid coordinate system, whereas Lambert (1984) used pressure coordinates over the whole vertical domain. Furthermore, the simulated global dynamics was found the be in full agreement with the theoretical picture of the Lorenz Energy Cycle.

These conclusions motivate us to explore more details regarding the mesoscale dynamics. For example, the $-5/3$ scaling law for horizontal variance spectra is not the only scaling law prediction of the idealized ST theory. Vertical wavenumber power spectra for the horizontal winds and temperature with -3 exponential spectral slopes are also predicted by ST theory. The existence of such a power law for atmospheric GWs is well known (e.g, VanZandt (1982), Smith et al. (1987), Weinstock (1996), Cot (2001), Sato et al. (2017), Guo et al. (2017)). In future studies, it is highly desirable to analyze the vertical wavenumber spectra and to estimate the GW frequency spectra using ST theory to further validate the idea that the mesoscales are in fact characterized by a macro-turbulent inertial range.

Our results also have important implications regarding higher altitudes of the atmosphere. Specifically, the winter mesosphere and lower thermosphere (MLT) is a very preferable region for studying GW energetics. The strongest GW energy per unit mass in the atmosphere resides in winter MLT (e.g., Becker and Vadas (2020), Becker et al. (2020), Avsarkisov et al. (2022)). The reason is that the spatially and intermittent breakdown of primary GWs in the winter stratopause region gives rise to the generation of secondary GWs that can propagate into the MLT and create spatial and temporal variability there (Becker and Vadas (2018)). These secondary GWs significantly im-

pacts the dynamics of the thermal tides and planetary waves as well as the transport of constituents across the mesopause. Since secondary GWs can have large horizontal wavelengths, the mesoscale scaling of the $-5/3$ law starts at lower wavenumbers in the MLT than in the lower atmosphere (at about $n \sim 50$, Becker et al. (2022)). Therefore, the forward cascades of KE and APE are expected to become more dominant at these larger scales in the MLT in comparison to UTLS regions, according to the findings of this thesis. In future, analysing the resolved spectral KE and APE budgets in the mesoscales of the MLT would answer the question whether the $n^{-5/3}$ power law found in this region can be explained by SMT or not. Note that Avsarkisov et al. (2022) showed that the characteristic SMT statistics in physical space of the MLT region are pronounced in regions of wave breaking. This suggests that our findings regarding the energetics of saturated GWs should apply also in the MLT.

As a final remark, it should be mentioned that there is also room for further theoretical and numerical development. Extension of the SIC to vertical diffusion of horizontal momentum and sensible heat should be pursued to achieve a fully scale-invariant SGS diffusion scheme. Schaefer-Rolffs and Becker (2018) implemented the scale-invariant gDSM scheme for horizontal momentum diffusion by extending the SIC from horizontal diffusion of horizontal momentum to vertical diffusion of horizontal momentum. They reported that such an extension did not introduce a significant difference for the simulated horizontal KE spectrum. In the current study, we did not consider fulfilling the SIC for the vertical diffusion of horizontal momentum and sensible heat. Another important point pertains to the dependence of the vertical diffusion scheme in the KMCM on the Richardson number, i.e. R_i. As we discussed in chapter 5.1.1, R_i dependent vertical diffusion schemes have been shown to overly damp the vertical motions at the smallest scales(Waite (2016)). This results in non-constant (wavenumber-dependent) forward spectral fluxes of KE and APE (in comparison, idealized ST predicts constant spectral fluxes over the inertial range). Therefore, utilization of a R_i dependent vertical diffusion scheme could be the reason why KMCM does not simulate constant spectral energy fluxes at least over a certain wavenumber regime of the resolved mesoscales (see Figure 5.2). It should be noted that Schaefer-Rolffs and Becker (2018) found decreasing vertical mechanical dissipation rates for fully scale invariant diffusion of horizontal momentum, in comparison to runs with a prescribed vertical mixing length. This result points to the idea that extension of the SIC to vertical diffusion may provide a remedy for overly damped vertical motions. This means that the extension of SIC to

the vertical diffusion and thereby relaxing the explicit dependence on Ri could improve the simulated energy cascades and strengthen the validity of SMT for the mesoscales simulated in high-resolution general circulation models.

References

Asselin, R., 1972: Frequency filter for time integrations, *Mon. Wea. Rev.*, **100**, 487-490.

Augier, P. and Lindborg, E., 2013: A new formulation of the spectral energy budget of the atmosphere, with application to two high-resolution general circulation models, *J. Atmos. Sci.*, **70**, 2293–2308.

Augier, P., Billant, P. and Chomaz, J., -M., 2015: Stratified turbulence forced with columnar dipoles: numerical study, *J. Fluid Mech.*, **769**, 403–443.

Avsarkisov, V., 2020: On the buoyancy subrange in stratified turbulence, *Atmosphere*, **11**, 659.

Avsarkisov, V., Becker, E. and Renkwitz, T., 2022: Turbulent parameters in the middle atmosphere: Theoretical estimates deduced from a gravity wave–resolving general circulation model, *J. Atmos. Sci.*, **79** (4), 933– 952.

Becker, E., 2001: Symmetric stress tensor formulation of horizontal momentum diffusion in global models of atmospheric circulation, *J. Atmos. Sci.* **58**, 269–282.

Becker, E., 2003: *Energetics of turbulent momentum diffusion and gravity wave breakdown in general circulation models of the atmosphere*, IAP, Kühlungsborn, 108 pp.

Becker, E., 2003: Frictional heating in global climate models, *Mon. Wea. Rev.*, **131**, 508–520.

Becker, E., 2004: Direct heating rates associated with gravity wave saturation, *J. Atmos. Sol.-Terr. Phys.*, **66**, 683–696.

Becker, E., 2009: Sensitivity of the upper mesosphere to the Lorenz Energy Cycle of the Troposphere, *J. Atmos. Sci.*, **66**, 647-666.

Becker, E., 2012: Dynamical control of the middle atmosphere, *Space Sci. Rev.*, **168**, 283–314.

Becker, E., 2017: Mean-flow effects of thermal tides in the mesosphere and lower thermosphere, *J. Atmos. Sci.*, **74**, 2043–2063.

Becker E., 2019: *Physics of Climate*, University of Rostock, 83 pp.

Becker, E. and Burkhardt, U., 2007: Nonlinear horizontal diffusion for GCMs, *Mon. Wea. Rev.*, **135**, 1439–1454.

Becker, E. and McLandress, C., 2009: Consistent scale interaction of gravity waves in the Doppler spread parameterization, *J. Atmos. Sci.*, **66**, 1434–1449.

Becker, E. and Vadas, S., L., 2018: Secondary gravity waves in the winter mesosphere: Results from a high-resolution global circulation model, *J. Geophys. Res.*, **123**, 2605–2627.

Becker, E. and Vadas, S., L., 2020: Explicit global simulation of gravity waves in the thermosphere, *Journal of Geophysical Research - A: Space Physics*, **125**.

Becker, E., Grygalashvyly and Sonnemann, G., 2020: Gravity wave mixing effects on the OH*-layer, *Advances in Space Research*, **65**, 175-188.

Becker, E., Vadas, S., L., Bossert, K., Harvey, V., L., Zülicke, C. and Hoffmann, L., 2022: A high-resolution whole-atmosphere model with resolved gravity waves and specified large-scale dynamics in the troposphere and lower stratosphere, *Journal of Geophysical Research: Atmospheres*, **submitted**.

Billant, P. and Chomaz, J.-M., 2001: Self-similarity of strongly stratified inviscid flows, *Phys. Fluids*, **13**, 1645-1651.

Blažica, V., Žagar, N., Strajnar, B. and Cedilnik, J., 2013: Rotational and divergent kinetic energy in the mesoscale model ALADIN, *Tellus*, **65A**, 18918.

Boer, G., J. and Lambert, S., J., 2008: The energy cycle in atmospheric models, *Climate Dyn.*, **30**, 371-390.

Boer, G., J. and Shepherd, T., G., 1983: Large-Scale Two-Dimensional Turbulence in the Atmosphere, *J. Atmos. Sci.*, **40**, 164-184.

Boyd, J., P., 2001: *Chebyshev and Fourier Spectral Methodss*, 2nd. Ed., Mineola, New York: Dover, 688 pp.

Brethouwer, G., P., Billant, P., Lindborg, E. and Chomaz, J.-M., 2007: Scaling analysis and simulation of strongly stratified turbulent flows, *J. Fluid Mech.*, **585**, 343–368.

Brune, S. and Becker E., 2013: Indications of stratified turbulence in a mechanistic GCM, *J. Atmos. Sci.*, **70**, 231-247.

Burgess, B., H., Erler A., R. and Shepherd, J., G., 2012: The troposphere-to-stratosphere transition in kinetic energy spectra and nonlinear spectral fluxes as seen in ECMWF analyses, *J. Atmos. Sci.*, **70**(2), 669-687.

Callies, J., Ferrari, R. and Bühler, O., 2014: Transition from geostrophic turbulence to inertia–gravity waves in the atmospheric energy spectrum, *Proc. Natl. Acad. Sci. USA*, **111**, 17 033–17 038.

Callies, J., Bühler, O. and Ferrari, R., 2016: The dynamics of mesoscale winds in the upper troposphere and lower stratosphere, *J. Atmos. Sci.*, **73**, 4853–4872.

Carnevale, G., F., Briscolini, M. and Orlandi, P., 2001: Buoyancy- to inertial-range transition in forced stratified turbulence, *J. Fluid Mech.*, **427**, 205–239.0.

Cho, J., Y., N. and Lindborg, E., 2001: Horizontal velocity structure functions in the upper troposphere and lower stratosphere: 1. Observations., *J. Geophys. Res.*, **106** (D10), 10223–10232.

Cot, C., 2001: Equatorial mesoscale wind and temperature fluctuations in the lower atmosphere, *J. Geophys. Res.*, **106** (D2), 1523–1532.

Deusebio, E., Augier, P. and Lindborg, E., 2014: Third-order structure functions in rotating and stratified turbulence: A comparison between numerical, analytical and observational results, *J. Fluid Mech.*, **755**, 294–313.

Fourier, J., -B., -J., 1878: *The Analytical Theory of Heat*, University Press, 466 pp.

Fritts, D., C. and Alexander P., M., 2003: Gravity wave dynamics and effects in the middle atmosphere, *Rev. Geophys.*, **41**, 1003.

Fritts, D., C. and Dunkerton, T., J., 1985: Fluxes of heat and constituents due to convectively unstable gravity waves, *J. Atmos. Sci.*, **42**, 549–556.

Fritts, D., C. and Werne J., A., 2000: Turbulence dynamics and mixing due to gravity waves in the lower and middle atmosphere, *Atmospheric Science across the Stratopause, Geophys. Monogr.*, Vol. 123, Amer. Geophys. Union, 143–159.

Galperin, B. and Sukoriansky, B., 2010: Geophysical flows with anisotropic turbulence and dispersive waves: flows with stable stratification, *Ocean Dynamics*, **60**, 1319-1337.

Germano, M., Piomelli, U., Moin, P. and Cabot, W., H., 1991: A dynamic subgrid-scale eddy viscosity model, *Phys. Fluids*, **3**, 1760–1765.

Gill A., 1982: *Atmosphere-Ocean Dynamics*, International Geophysics Series, Vol. 30 Academic Press, 679 pp.

Guo, Y., Liu, A., Z. and Gardner, C., S., 2017: First Na lidar measurements of turbulence heat flux, thermal diffusivity, and energy dissipation rate in the mesopause region, *Geophys. Res. Lett.*, **44**(11), 5782– 5790.

Hamilton, K., Takahashi, Y.O. and Ohfuchi, W., 2008: Mesoscale spectrum of atmospheric motions investigated in a very fine resolution global general circulation model, *J. Geophys. Res.*, **113**, D18110.

Hartmann, D., L., 1994: *Global Physical Climatology*, International Geophysics Series, Vol. 56, Academic Press, 411 pp.

Haurwitz B., 1941: *Dynamic Meteorology*, McGraw-Hill Book Co., 365 pp.

Held, I., M. and Suarez, M., J., 1994: A proposal for the intercomparison of the dynamical cores of atmospheric general circulation models, *Bull. Amer. Meteor. Soc.*, **75**, 1825–1830.

Hines, C., O. and Reddy C., A., 1967: On the propagation of atmospheric gravity waves through regions of wind shear, *J. Geophys. Res.*, **72**, 1015–1034.

Holloway, G., 1988: The buoyancy flux from internal gravity wave breaking, *Dyn. Atmos. Oceans*, **12**, 107–125.

Howland, C., Taylor, J. and Caulfield, C., 2020: Mixing in forced stratified turbulence and its dependence on large-scale forcing, *J. Fluid Mech.*, **898**, A7.

Khani, S. and Waite, M., L., 2014: Buoyancy scale effects in large-eddy simulations of stratified turbulence, *J. Fluid Mech.*, **754**, 75–97.

Khani, S. and Waite, M., L., 2014: Large eddy simulations of stratified turbulence: The dynamic Smagorinsky model, *J. Fluid Mech.*, **773**, 327–344.

Kirkpatrick, M., P., Ackerman, A., S., Stevens, D., E. and Mansour, N., N., 2006: On the application of the dynamic Smagorinsky model to large-eddy simulations of the cloud-topped atmospheric boundary layer, *J. Atmos. Sci.*, **63**, 526–546.

Koshyk, J., N. and Hamilton K., 2001: The horizontal kinetic energy spectrum and spectral budget simulated by a high-resolution troposphere–stratosphere–mesosphere GCM, *J. Atmos. Sci.*, **58**, 329–348.

Koshyk, J., N., Hamilton K. and Mahlman, J., 1999: Simulation of k-5/3 mesoscale spectral regime in the GFDL SKYHI general circulation model, *Geophys. Res. Lett.*, **26**, 843–846.

Kraichnan, R., 1967: Inertial ranges in two-dimensional turbulence, *Phys. Fluids*, **10**, 14177-1423.

Lambert, S., J., 1984: A global available potential energy-kinetic energy budget in terms of the two-dimensional wavenumber for the FGGE year, *Atmos.-Ocean*, **22**, 262-282.

Launder, B., E. and Spalding, D., B., 1973: The numerical computation of turbulent flows, *Computer Methods in Applied Mechanics and Engineering*, **3**, 269-289.

Li, Q. and Lindborg, E., 2018: Weakly or strongly nonlinear mesoscale dynamics close to the tropopause, *J. Atmos. Sci.*, **75**, 1215–1229.

Lilly, D., K., 1983: Stratified turbulence and the mesoscale variability of the atmosphere, *J. Atmos. Sci.*, **40**, 749-761.

Lindborg, E., 1999: Can the atmospheric energy spectrum be explained by two-dimensional turbulence?, *J. Fluid Mech.*, **388**, 259–288.

Lindborg, E., 2005: The effect of rotation on the mesoscale energy cascade in the free atmosphere, *Geophys. Res. Lett.*, **32**, L010809.

Lindborg, E., 2006: The energy cascade in a strongly stratified fluid, *J. Fluid Mech.*, **550**, 207-242.

Lindborg, E., 2009: Two comments on the surface quasigeostrophic model for the atmospheric energy spectrum, *J. Atmos. Sci.*, **66** (4), 1069–1072.

Lindborg, E., 2015: A Helmholtz decomposition of structure functions and spectra calculated from aircraft data, *J. Fluid Mech.*, **762**, R4.

Lindzen, R., S., 1981: Turbulence and stress owing to gravity wave and tidal breakdown, *J. Geophys. Res.*, **86**, 9707–9714.

Lindzen, R., E., 1990: *Dynamics in Atmospheric Physics*, Cambridge University Press, 310 pp.

Liu, H., L., 2000: Temperature changes due to gravity wave saturation, *J. Geophys. Res.*, **105**(D10), 12329–12436.

Lorenz, N., E., 1955: Available potential energy and the general circulation, *Tellus*, **7**, 157-167.

Lorenz, N., E., 1967: *The nature and theory of the general circulation of the atmosphere*, World Meteorological Organization Geneva, Vol. 218, 161 pp.

Luce, H., Kantha, L., Hashiguchi, H. and Lawrence, D., 2019: Estimation of turbulence parameters in the lower troposphere from ShUREX (2016–2017) UAV data, *Atmosphere*, **10**(7), 384.

Lund, T., Fritts, D., Kam, W., Laughman, B. and Liu, H.,-L., 2020: Numerical simulation of mountain waves over the southern Andes, Part 1: Mountain wave and secondary wave character, evolutions, and breaking, *J. Atmos. Sci.*, **77**(12), 4337–4356.

Maffioli, A., 2017: Vertical spectra of stratified turbulence at large horizontal scales, *Phys. Rev. Fluids*, **2** (10), 104802.

Maffioli, A. and Davidson P., A., 2016: Dynamics of stratified turbulence decaying from a high buoyancy Reynolds number, *J. Fluid Mech.*, **786**, 210–233.

Margules, M., 1903: Ueber die energie der stürme , *Jahrbuch der k. k. Zentralanstalt für Meteorologie*, 1-26.

Margules, M., 1906: Zur sturmtheorie, *Meteorologische Zeitschrift*, **23**, 481-497.

Nastrom, G., K. and Gage K., 1985: A climatology of atmospheric wavenumber spectra of wind and temperature observed by commercial aircraft, *J. Atmos. Sci.*, **42**, 950-960.

Nastrom, G., K., Gage, K. and Jasperson W. 1984: Kinetic energy spectrum of large- and mesoscale atmospheric processes, *Nature*, **310**, 36-38.

O'Sullivan, D. and Dunkerton T., J., 1995: Generation of inertia-gravity waves in a simulated life-cycle of baroclinic instability, *J. Atmos. Sci.*, **52**, 3695–3716.

Oort, H., A., 1964: On estimates of the atmospheric energy cycle, *Mon. Wea. Rev.*, **92**, 483-493.

Orlanski, I., 1975: A rational subdivision of scales for atmospheric processes, *A. Met. Soc.*, **5**, 527-530.

Peixoto, J., P. and Oort, A., H., 1992: *Physics of Climate*, American Institute of Physics , 520 pp.

Phillips, N., 1966: The equations of motion for a shallow rotating atmosphere and the "traditional approximation", *J. Atmos. Sci*, **23 (5)**, 626-628.

Platzman, G., W., 1987: *Conversations With Jule Charney*(No. NCAR/TN-298+PROC), University Corporation for Atmospheric Research, 169 pp.

Plougonven, R. and Zhang, F., 2014: Internal gravity waves from atmospheric jets and fronts, *Rev. Geophys.*, **52**, 33-76.

Portwood, G., D., deBruynKops, S., M. and Caulfield C., A., 2019: Asymptotic dynamics of high dynamic range stratified turbulence, *Physical review letters*, **122** (19), 194504.

Prandtl, L., 1942:, *Führer durch die Strömungslehre (Essentials of Fluid Mechanics)*, Fried. Vieweg & Sohn, 382 pp.

Remmler, S. and Hickel, S., 2014: Spectral eddy viscosity of stratified turbulence, *J. Fluid Mech.*, **775**, R6.

Remmler, S., Hickel, S., Fruman, M. and Achatz, U., 2015: Validation of large-eddy simulation methods for gravity-wave breaking, *J. Atmos. Sci.*, **72**, 3537–3562.

Riley, J., J. and deBruynKops, S., M., 2003: Dynamics of turbulence strongly influenced by buoyancy, *Phys. Fluids*, **15**(7), 2047–2059.

Riley, J., J. and deBruynKops, S., M., 2019: The effects of stable stratification on the decay of initially isotropic homogeneous turbulence, *Phys. Fluids*, **860**, 787–821.

Riley, J., J., Metcalfe, R., W. and Weismann, M., A., 1981: Direct Numerical Simulation of Homogeneous Turbulence in Density-Stratified Fluids, *Proc. AIP Conf.*, **76**, 79-112.

Sagaut, P., 2006: *Large Eddy Simulation for Incompressible Flows: An Introduction*, 3rd. Ed., Springer Science & Business Media, Berlin, Heidelberg, 556 pp.

Sato, K., Kohma, M., Tsutsumi, M. and Sato, T., 2017: Frequency spectra and vertical profiles of wind fluctuations in the summer Antarctic mesosphere revealed by MST radar observations, *J. Geophys. Res. Atmos.*, **122**, 3-19.

Schaefer-Rolffs, U., 2017: A generalized formulation of the dynamic Smagorinsky model, *Meteor. Z.*, **26**, 181–187.

Schaefer-Rolffs, U., 2019: The Scale Invariance Criterion For Geophysical Fluids, *European Journal of Mechanics / B Fluids*, **74**, 92-98.

Schaefer-Rolffs, U. and Becker, E., 2013: A two-dimensional version of the dynamic Smagorinsky model for atmospheric circulation models, *Mon.Wea.Rev.*, **141**, 887–899.

Schaefer-Rolffs, U. and Becker, E., 2018: Scale-Invariant Formulation of Momentum Diffusion for High-Resolution Atmospheric Circulation Models, *J. Atmos. Sci.*, **146**, 1045-1062.

Schaefer-Rolffs, U. and Becker, E., 2019: Scale-Invariant Formulation of Momentum Diffusion for High-Resolution Atmospheric Circulation Models, *Mon.Wea.Rev.*, **146**, 1045-1062.

Schaefer-Rolffs, U., Knöpfel R., Becker, E., 2015: A scale invariance criterion for LES parametrizations, *Meteor. Z.*, **24**, 3-13.

Schumann, U., 2019: The Horizontal Spectrum of Vertical Velocities near the Tropopause from Global to Gravity Wave Scales, *J. Atmos. Sci.*, **76**, 3847–3862.

Salmon, R., 1998: *Lectures on Geophysical Fluid Dynamics*,Oxford University Press, 378 pp.

Serrin, J., 1959: *Encyclopedia of Physics*, S. Flügge and C. Truesdell, Eds., Springer-Verlag, 125–263.

Simmons, A., J. and Burridge D., M., 1981: An energy and angular momentum conserving vertical finitie-difference scheme and hybrid vertical coordinates, *Mon.Wea.Rev.*, **109**, 758-766.

Skamarock, W., C., Snyder, C., Klemp, J., B. and Park, S., -H., 2019: Vertical resolution requirements in atmospheric simulation, *Mon. Wea. Rev.*, **147**, 2641–2656.

Smagorinsky, J., 1963: General circulation experiments with the primitive equations. i. the basic experiment., *Mon. Wea. Rev.*, **91**, 99–164.

Smith, S., A., Fritts, D., C. and Van Zandt, T., E., 1987: Evidence for a saturated spectrum of atmospheric gravity waves, *J. Atmos. Sci.*, **44**, 1404–1410.

Smyth, W., D. and Moum, J., N., 2000: Anisotropy of turbulence in stably stratified mixing layers, *Phys. Fluids*, **12**, 1343–1362.

Starr, V., P. and White R., M., 1954: *Balance requirements of the general circulation*, Air Force Cambridge Research Center, Vol. 35 Geophys. Res. Papers, 57pp.

Starr, V., P, 1953: Note concerning the nature of the large-scale eddies in the atmosphere, *Tellus*, **5**, 494-498.

Taylor, G., I., 1935: Statistical theory of turbulence: Parts I-II, *Proc. R. Soc. Lond.*, A **151**, 421-64.

Tulloch, R. and Smith, W., W., 2009: Quasigeostrophic turbulence with explicit surface dynamics: Application to the atmospheric energy spectrum, *J. Atmos. Sci.*, **66** (2), 450-467.

Tung, K., K. and Orlando, W., W., 2003: The k^-3 and $k^-5/3$ energy spectrum of atmospheric turbulence: Quasigeostrophic two-level model simulation, *J. Atmos. Sci.*, **60**, 824–835.

Vadas, S., L. and Fritts, D., C. 2002: The importance of spatial variability in the generation of secondary gravity waves from local body forces, *Geophys. Res. Lett.*, **29**(20), 1984.

Vadas, S., L., Becker, E., Bossert, K., Baumgarten, G., Hoffmann, L. and Harvey, V., L., 2022: Secondary gravity waves from the stratospheric polar vortex over ALO-MAR Observatory on 12-14 January 2016: observations and modeling, *Journal of Geophysical Research: Atmospheres*, **127**(2).

van Mieghem, J., 1973: *Atmospheric Energetics*, Clarendon Press, 306 pp.

VanZandt, J., 1982: A universal spectrum of buoyancy waves in the atmosphere,, *Geophys. Res. Lett.*, **9**, 575–578.

Waite, M., L., 2011: Stratified turbulence at the buoyancy scale, *Phys. Fluids*, A **13**, 066602.

Waite, M., L., 2016: Dependence of model energy spectra on vertical resolution, *Mon. Wea. Rev.*, **144**, 1407–1421.

Waite, M., L., 2020: Untangling waves and vortices in the atmospheric kinetic energy spectra, *J. Fluid Mech.*, **888**, F1.

Waite, M., L. and Bartello P., 2004: Stratified turbulence dominated by vortical motion, *J. Fluid Mech.*, **517**, 281–303.

Waite, M. and Bartello P., 2006: The transition from geostrophic to stratified turbulence, *J. Fluid Mech.*, **568**, 89-108.

Waite, M., L. and Snyder C., 2014: The mesoscale kinetic energy spectrum of a baroclinic life cycle, *J. Atmos. Sci.*, **66**, 883–901.

Weinstock, J., 1996: Spectra and a global source of gravity waves for the middle atmosphere, *Adv. Space Res.*, **17**, 67–76.

Žagar, N., Kasahara, A., Terasaki, K., Tribbia, J. and Tanaka, H., 2015: Normal-mode function representation of global 3D datasets: Open-access software for the atmospheric research community, *Geosci. Model Dev.*, **8**, 1169–1195.

Žagar, N., Jelić, D., Blaauw, M. and Bechtold, P., 2017: Energy spectra and inertia–gravity waves in global analyses, *J. Atmos. Sci.*, **74**, 2447–2466.

Zhang, F., 2004: Generation of mesoscale gravity waves in upper-tropospheric jet–front systems, *J. Atmos. Sci.*, **61**, 440–457.

Appendix A

Derivation of the Approximate Form of APE

We start with the expansion in power series for the $\overline{p^{\kappa+1}}$ term to the second order only, since atmosphere assumes small deviations from $\bar{p}$.

$$\overline{p^{\kappa+1}} \approx \bar{p}^{\kappa+1} + (\kappa+1)\bar{p}^{\kappa}(\overline{p-\bar{p}}) + \frac{1}{2}(\kappa+1)\kappa\bar{p}^{\kappa-1}\overline{(p-\bar{p})^2} \tag{A.1}$$

By definition $\tilde{p} = p - \bar{p}$. Accordingly, the second term in equation (A.1) equals to zero, since $\bar{\tilde{p}} = 0$. We insert the above power series expansion to the equation (2.16):

$$A\hat{P}E \approx \frac{c_p\kappa}{2g} \int_0^\infty \left(\frac{\bar{p}}{p_{00}}\right)^\kappa \left(\frac{\overline{\tilde{p}^2}}{\bar{p}}\right) d\theta. \tag{A.2}$$

Lorenz (1955) argues that following approximation holds (his equation 7) in atmosphere;

$$\tilde{p} \approx -\tilde{\theta}\frac{\partial \bar{p}}{\partial \theta}. \tag{A.3}$$

Since in θ coordinates $d\theta = d\bar{\theta}$ and by definition $R = c_p\kappa$, we transform equation (A.2) into the pressure coordinates using relation (A.3) as follows;

$$A\hat{P}E \approx \frac{R}{2g} \int_{p_{00}}^0 \left(\frac{\bar{p}}{p_{00}}\right)^\kappa \left(\frac{\overline{\tilde{\theta}^2}}{\bar{p}}\right)\left(\frac{\partial \bar{\theta}}{\partial \bar{p}}\right)^{-1} d\bar{p}. \tag{A.4}$$

For the next step, we use following relations to rewrite $A\hat{P}E$ in terms of the variance of temperature;

$$\left(\frac{\partial\bar{\theta}}{\partial\bar{p}}\right)^{-1} = -\frac{g^2\bar{\rho}}{\bar{\theta}\overline{N^2}}, \tag{A.5}$$

$$\left(\frac{\bar{p}}{p_{00}}\right)^{\kappa} = \frac{\overline{T}}{\bar{\theta}}, \tag{A.6}$$

$$\tilde{\theta} = \tilde{T}\frac{\bar{\theta}^2}{\overline{T}^2}, \tag{A.7}$$

$$d\bar{p} = dp. \tag{A.8}$$

In relation (A.5) we used the definition of the squared buoyancy frequency, i.e. $N^2 = -g^2\rho\frac{\partial_p\theta}{\theta}$. Accordingly, an approximate form of $A\hat{P}E$ that can be calculated using the prognostic temperature deviations from its horizontal mean is given by;

$$A\hat{P}E \approx \frac{g}{2}\int_0^{p_{00}} \frac{\overline{\tilde{T}^2}}{\overline{T}^2\overline{N^2}}\, dp. \tag{A.9}$$

Appendix B

Derivation of the APE Budget

Starting with the enthalpy equation (2.4), we decompose it into horizontal mean (i.e. $c_p\overline{T}$) and its deviations (i.e. $c_p\widetilde{T}$):

$$\partial_t\widetilde{T} = -\vec{v}_h \cdot \vec{\nabla}_h\widetilde{T} - \omega\partial_p\widetilde{T} - \omega\partial_p\overline{T} + \frac{R\widetilde{T}}{c_pp}d_tp + \frac{R\overline{T}}{c_pp}d_tp + \frac{1}{c_p}Q. \qquad (B.1)$$

In equation (B.1) we have made use of the fact that $\vec{\nabla}_h\overline{T} = 0$ and assumed $\partial_t\overline{T} \approx 0$, since the rate of change of horizontal mean of temperature is negligibly small compared to other terms in the tendency of $\widetilde{T}$. Also the frictional heating term ϵ is included in Q. We add and subtract two terms ($\widetilde{T}\omega\frac{\partial_p\overline{T}}{\overline{T}}$ and $\widetilde{T}\omega\frac{\partial_p\overline{N}^2}{2\overline{N}^2}$);

$$\partial_t\widetilde{T} = -\vec{v}_h \cdot \vec{\nabla}_h\widetilde{T} - \omega\partial_p\widetilde{T} \underbrace{-\omega\partial_p\overline{T} + \frac{R\widetilde{T}}{c_pp}d_tp + \frac{R\overline{T}}{g^2p}d_tp}_{\overline{T}\left[\frac{R}{c_pp}\left(1+\frac{\widetilde{T}}{\overline{T}}\right)\omega\right]} + \frac{1}{c_p}Q + \widetilde{T}\omega\frac{\partial_p\overline{T}}{\overline{T}} - \widetilde{T}\omega\frac{\partial_p\overline{T}}{\overline{T}}$$

$$+ \widetilde{T}\omega\frac{\partial_p\overline{N}^2}{2\overline{N}^2} - \widetilde{T}\omega\frac{\partial_p\overline{N}^2}{2\overline{N}^2}. \qquad (B.2)$$

Purple terms in above equation are further manipulated in 4 steps;

$$\begin{aligned}
&1) -\omega\partial_p\overline{T} + \overline{T}\left[\frac{R}{c_pp}\left(1+\frac{\widetilde{T}}{\overline{T}}\right)\omega\right] - \widetilde{T}\omega\frac{\partial_p\overline{T}}{\overline{T}} \\
&2) -\omega\partial_p\overline{T}\left[1+\frac{\widetilde{T}}{\overline{T}}\right] + \overline{T}\omega\left[1+\frac{\widetilde{T}}{\overline{T}}\right]\frac{R}{c_pp} \\
&3) \left[1+\frac{\widetilde{T}}{\overline{T}}\right]\omega\overline{T}\left[\frac{R}{c_pp} - \frac{\partial_p\overline{T}}{\overline{T}}\right] \\
&4) \left(1+\frac{\widetilde{T}}{\overline{T}}\right)\omega\overline{N}^2\frac{R\overline{T}^2}{c_pp}
\end{aligned} \qquad . \qquad (B.3)$$

Definition of $\overline{N}^2$ is given in equation (2.27). After these steps we have;

$$\partial_t \widetilde{T} = -\vec{v}_h \cdot \vec{\nabla}_h \widetilde{T} - \omega \partial_p \widetilde{T} + \left(1 + \frac{\widetilde{T}}{\overline{T}}\right)\omega \overline{N}^2 \frac{R\overline{T}^2}{c_p p} + \frac{1}{c_p}Q + \widetilde{T}\omega \frac{\partial_p \overline{T}}{\overline{T}}$$
$$+ \widetilde{T}\omega \frac{\partial_p \overline{N}^2}{2\overline{N}^2} - \widetilde{T}\omega \frac{\partial_p \overline{N}^2}{2\overline{N}^2}. \tag{B.4}$$

We finally multiply the left and right-hand side with $\frac{g^2 \widetilde{T}}{\overline{N}^2 \overline{T}^2}$ to get a term for grid space APE;

$$\underbrace{C\widetilde{T}\partial_t\widetilde{T}}_{\text{Tendency of APE, } \partial_t APE} = \underbrace{-C\widetilde{T}\vec{v}_h \cdot \vec{\nabla}_h \widetilde{T}}_{\text{Hor. Adv. of APE, } -\vec{v}_h \cdot \vec{\nabla}_h APE} \underbrace{+ \widetilde{T}\left(1 + \frac{\widetilde{T}}{\overline{T}}\right)\omega \frac{R}{p}}_{\text{Neg. Buoy. Prod.}}$$

$$\underbrace{-C\widetilde{T}\omega\partial_p\widetilde{T} + C\widetilde{T}\frac{\widetilde{T}}{\overline{T}}\omega\partial_p\overline{T} + C\widetilde{T}\frac{\widetilde{T}}{2\overline{N}^2}\omega\partial_p\overline{N}^2}_{\text{Ver. Adv. of APE, } -\omega\partial_p APE} \quad \underbrace{+ C\widetilde{T}\frac{1}{c_p}Q}_{\text{Diab. Heat.}} \quad \underbrace{-C\widetilde{T}\frac{\widetilde{T}}{2\overline{N}^2}\omega\partial_p\overline{N}^2}_{\text{Ver. Exch. of APE, } -\omega APE \frac{\partial_p \overline{N}^2}{\overline{N}^2}}$$
$$\tag{B.5}$$

98

Appendix C

Explicit Form of μ_{h5}

To complete the total SGS horizontal diffusion of sensible heat we need an expression for the divergence of $\frac{1}{Pr_t}$. Explicit derivations are shown below for the term μ_{h5}.

$$c_p \frac{K_h}{Pr_h} \vec{\nabla}_h \left(\frac{1}{Pr_h} \right) \cdot \vec{\nabla}_h T = -c_p \frac{K_h}{Pr_h^2} (\vec{\nabla}_h Pr_h \cdot \vec{\nabla}_h \overline{T}). \tag{C.1}$$

We use equation (3.22) for $\vec{\nabla}_h Pr_h$;

$$\vec{\nabla}_h Pr_h = \vec{\nabla}_h(c_s^2) \frac{\|\vec{\mathcal{M}}_T\|}{\|\vec{\mathcal{L}}_T\|} + c_s^2 \vec{\nabla}_h \left(\frac{\|\vec{\mathcal{M}}_T\|}{\|\vec{\mathcal{L}}_T\|} \right), \tag{C.2}$$

where the expression for $\vec{\nabla}(c_s^2)_h$ is adopted from the existing gDSM scheme utilized for the horizontal momentum diffusion and can be found in Schaefer-Rolffs and Becker (2018). Accordingly, equation C.2 is rewritten as;

$$\vec{\nabla}_h Pr_h = \left[\left[\frac{\vec{\nabla}_h(|\mathbf{L}|)}{|\mathbf{L}|} - \frac{\vec{\nabla}_h(|\mathbf{M}|)}{|\mathbf{M}|} \right] c_s^2 \right] \underbrace{\frac{|\vec{\mathcal{M}}|}{|\vec{\mathcal{L}}|}}_{Pr_h} + c_s^2 \underbrace{\frac{|\vec{\mathcal{M}}|}{|\vec{\mathcal{L}}|}}_{Pr_h} \left[\frac{\vec{\nabla}_h(|\vec{\mathcal{M}}|)}{|\vec{\mathcal{M}}|} - \frac{\vec{\nabla}_h(|\vec{\mathcal{L}}|)}{|\vec{\mathcal{L}}|} \right]. \tag{C.3}$$

Again, the expressions for $\vec{\nabla}_h(|\mathbf{L}|)$ and $\vec{\nabla}_h(|\mathbf{M}|)$ are taken from the existing gDSM scheme. We further gather terms to form Pr_h;

$$\vec{\nabla}_h Pr_h = Pr_h \underbrace{\left[\left[\frac{\vec{\nabla}_h(|\mathbf{L}|)}{|\mathbf{L}|} - \frac{\vec{\nabla}_h(|\mathbf{M}|)}{|\mathbf{M}|} \right] + \left[\frac{\vec{\nabla}_h(|\vec{\mathcal{M}}|)}{|\vec{\mathcal{M}}|} - \frac{\vec{\nabla}_h(|\vec{\mathcal{L}}|)}{|\vec{\mathcal{L}}|} \right] \right]}_{\vec{X}}. \tag{C.4}$$

The individual expressions for $\vec{\nabla}_h(|\vec{\mathcal{L}}|)$ and $\vec{\nabla}_h(|\vec{\mathcal{M}}|)$ are given as;

$$\vec{\nabla}_h(|\vec{\mathcal{L}}|) = \frac{1}{|\vec{\mathcal{L}}|}(\mathcal{L}_1\vec{\nabla}_h\mathcal{L}_1 + \mathcal{L}_2\vec{\nabla}_h\mathcal{L}_2), \tag{C.5}$$

$$\vec{\nabla}_h(|\vec{\mathcal{M}}|) = \frac{1}{|\vec{\mathcal{M}}|}(\mathcal{M}_1\vec{\nabla}_h\mathcal{M}_1 + \mathcal{M}_2\vec{\nabla}_h\mathcal{M}_2), \tag{C.6}$$

$$\vec{\nabla}_h\mathcal{L}_1 = \begin{bmatrix} \widetilde{\widehat{\tilde{u}}\partial_x\widehat{\tilde{T}}} + \widetilde{\widehat{\tilde{T}}\partial_x\widehat{\tilde{u}}} - \left(\widehat{\tilde{\tilde{u}}\partial_x\widehat{\tilde{\tilde{T}}}} + \widehat{\tilde{\tilde{T}}\partial_x\widehat{\tilde{\tilde{u}}}}\right) \\ \widetilde{\widehat{\tilde{u}}\partial_y\widehat{\tilde{T}}} + \widetilde{\widehat{\tilde{T}}\partial_y\widehat{\tilde{u}}} - \left(\widehat{\tilde{\tilde{u}}\partial_y\widehat{\tilde{\tilde{T}}}} + \widehat{\tilde{\tilde{T}}\partial_y\widehat{\tilde{\tilde{u}}}}\right) \end{bmatrix}, \tag{C.7}$$

$$\vec{\nabla}_h\mathcal{L}_2 = \begin{bmatrix} \widetilde{\widehat{\tilde{v}}\partial_x\widehat{\tilde{T}}} + \widetilde{\widehat{\tilde{T}}\partial_x\widehat{\tilde{v}}} - \left(\widehat{\tilde{\tilde{v}}\partial_x\widehat{\tilde{\tilde{T}}}} + \widehat{\tilde{\tilde{T}}\partial_x\widehat{\tilde{\tilde{v}}}}\right) \\ \widetilde{\widehat{\tilde{v}}\partial_y\widehat{\tilde{T}}} + \widetilde{\widehat{\tilde{T}}\partial_y\widehat{\tilde{v}}} - \left(\widehat{\tilde{\tilde{v}}\partial_y\widehat{\tilde{\tilde{T}}}} + \widehat{\tilde{\tilde{T}}\partial_y\widehat{\tilde{\tilde{v}}}}\right) \end{bmatrix}, \tag{C.8}$$

$$\vec{\nabla}_h\mathcal{M}_1 = -(\widehat{\Delta})^2 \begin{bmatrix} \left(\frac{\tilde{\Delta}}{\widehat{\tilde{\Delta}}}\right)^2\left[\widehat{\widetilde{\partial_x\overline{|\mathbf{S}|}\partial_x\tilde{\tilde{T}}}} + \widehat{\widetilde{\overline{|\mathbf{S}|}\partial_x^2\tilde{\tilde{T}}}}\right] - \left[\widetilde{\partial_x\widehat{\overline{|\mathbf{S}|}}\partial_x\widehat{T}} + \widetilde{\widehat{\overline{|\mathbf{S}|}}\partial_x^2\widehat{T}}\right] \\ \left(\frac{\tilde{\Delta}}{\widehat{\tilde{\Delta}}}\right)^2\left[\widehat{\widetilde{\partial_y\overline{|\mathbf{S}|}\partial_x\tilde{\tilde{T}}}} + \widehat{\widetilde{\overline{|\mathbf{S}|}\partial_y\partial_x\tilde{\tilde{T}}}}\right] - \left[\widetilde{\partial_y\widehat{\overline{|\mathbf{S}|}}\partial_x\widehat{T}} + \widetilde{\widehat{\overline{|\mathbf{S}|}}\partial_y\partial_x\widehat{T}}\right] \end{bmatrix}, \tag{C.9}$$

$$\vec{\nabla}_h\mathcal{M}_2 = -(\widehat{\Delta})^2 \begin{bmatrix} \left(\frac{\tilde{\Delta}}{\widehat{\tilde{\Delta}}}\right)^2\left[\widehat{\widetilde{\partial_x\overline{|\mathbf{S}|}\partial_y\tilde{\tilde{T}}}} + \widehat{\widetilde{\overline{|\mathbf{S}|}\partial_x\partial_y\tilde{\tilde{T}}}}\right] - \left[\widetilde{\partial_x\widehat{\overline{|\mathbf{S}|}}\partial_y\widehat{T}} + \widetilde{\widehat{\overline{|\mathbf{S}|}}\partial_x\partial_y\widehat{T}}\right] \\ \left(\frac{\tilde{\Delta}}{\widehat{\tilde{\Delta}}}\right)^2\left[\widehat{\widetilde{\partial_y\overline{|\mathbf{S}|}\partial_y\tilde{\tilde{T}}}} + \widehat{\widetilde{\overline{|\mathbf{S}|}\partial_y^2\tilde{\tilde{T}}}}\right] - \left[\widetilde{\partial_y\widehat{\overline{|\mathbf{S}|}}\partial_y\widehat{T}} + \widetilde{\widehat{\overline{|\mathbf{S}|}}\partial_y^2\widehat{T}}\right] \end{bmatrix}, \tag{C.10}$$

where,

$$\vec{\mathcal{L}} = \begin{bmatrix} \mathcal{L}_1 \\ \mathcal{L}_2 \end{bmatrix}, \tag{C.11}$$

and

$$\vec{\mathcal{M}} = \begin{bmatrix} \mathcal{M}_1 \\ \mathcal{M}_2 \end{bmatrix}. \tag{C.12}$$

Finally equation (C.1) would read;

$$\mu_{h5} = -c_p\frac{K_h}{Pr_h}(\vec{X} \cdot \vec{\nabla}_h\overline{T}). \tag{C.13}$$

Appendix D

Detail from the Derivation of GW KE equation

Here we explicitly show the derivation steps from equation (5.16) to (5.18), regarding the horizontal pressure gradient term in z-coordinates. We start by expanding this term as;

$$-\overline{\vec{v}_h^* \cdot \frac{\vec{\nabla}_h p^*}{\rho_r}} = -\frac{1}{\rho_r}\overline{\vec{\nabla}_h \cdot (\vec{v}_h^* p^*)} + \frac{1}{\rho_r}\overline{p^*\vec{\nabla}_h \cdot \vec{v}_h^*}, \tag{D.1}$$

where the single-column approximation causes first term in equation (D.1) to be dropped. Using the continuity equation of GWs, i.e. $\vec{\nabla}_h \cdot \vec{v}_h^* + \partial_z w^* = 0$, we can rewrite the second term in (D.1) as;

$$\frac{1}{\rho_r}\overline{p^*\vec{\nabla}_h \cdot \vec{v}_h^*} = \frac{1}{\rho_r}\overline{-p^*\partial_z w^*} = -\frac{1}{\rho_r}\partial_z\overline{p^*w^*} + \frac{1}{\rho_r}\overline{w^*\partial_z p^*}. \tag{D.2}$$

Using the hydrostatic approximation, i.e. $\partial_z p^* = -g\rho^*$, we again rewrite the second term in equation (D.2);

$$\frac{1}{\rho_r}\overline{w^*\partial_z p^*} = -\frac{1}{\rho_r}\overline{\rho^*w^*}. \tag{D.3}$$

As it is explained in Becker (2017), the exact thermodynamic relation,

$$\frac{d\Theta}{\Theta} = -\frac{d\rho}{\rho} + \frac{c_v}{c_p}\frac{dp}{p}, \tag{D.4}$$

leads to the anelastic version of the relation of thermodynamic perturbations to the reference values, such that;

$$\frac{\check{\Theta}}{\Theta_r} = -\frac{\check{\rho}}{\rho_r}, \tag{D.5}$$

where (ˇ) denotes the deviations from the reference state. Equation (D.5) also implies,

$$\frac{\check{\Theta}}{\Theta_r} = \frac{\check{T}}{T_r}, \tag{D.6}$$

We further assume that GW scale perturbations and deviations from the reference state are similar in amplitude such that following relation holds;

$$\frac{(\;\breve{}\;)}{(\;)_r} = \frac{(\;)^*}{(\overline{\;})}. \tag{D.7}$$

Relation (D.7) and equations (D.5) & (D.6) are used to rewrite the vertical flux of the GW scale density fluctuations, i.e. equation (D.3) as;

$$-\frac{1}{\rho_r}\overline{\rho^* w^*} = \frac{g}{T_r}\overline{T^* w^*}. \tag{D.8}$$

Equation (D.8) represents the GW scale negative buoyancy production term, which formally corresponds to mesoscale energy conversion term, i.e. APE^{NBP}, in our resolved spectral APE budget. As a result the pressure gradient term in (5.16) is rewritten as;

$$-\overline{\vec{v}_h^* \cdot \frac{\vec{\nabla}_h p^*}{\rho_r}} = -\frac{1}{\rho_r}\partial_z \overline{p^* w^*} + \frac{g}{T_r}\overline{T^* w^*}. \tag{D.9}$$

As it can be seen, the adiabatic conversion term in the KE equation (i.e. the pressure gradient term in z-coordinates in the left hand side of equation (D.9)) corresponds to the vertical geopotential flux convergence (vertical pressure flux convergence in z-coordinates in the right hand side of equation (D.9)) plus the reversible conversion term.

Acknowledgment

Declaration of Authorship

Ich gebe folgende Erklärung ab:

1. Die Gelegenheit zum vorliegenden Promotionsvorhaben ist mir nicht kommerziell vermittelt worden. Insbesondere habe ich keine Organisation eingeschaltet, die gegen Entgelt Betreuerinnen/Betreuer für die Anfertigung von Dissertationen sucht oder die mir obliegenden Pflichten hinsichtlich der Prüfungsleistungen für mich ganz oder teilweise erledigt.

2. Ich versichere hiermit an Eides statt, dass ich die vorliegende Arbeit selbstständig angefertigt und ohne fremde Hilfe verfasst habe. Dazu habe ich keine außer den von mir angegebenen Hilfsmitteln und Quellen verwendet und die den benutzten Werken inhaltlich und wörtlich entnommenen Stellen habe ich als solche kenntlich gemacht.

Unterschrift:

———————————————————

Ort, Datum: Rostock, 29.09.2022

———————————————————